

6-12-2019

Stray Radiation Dose from X-ray and Proton Beam Radiation Therapies

Christopher William Schneider
Louisiana State University and Agricultural and Mechanical College

Follow this and additional works at: https://repository.lsu.edu/gradschool_dissertations



Part of the [Health and Medical Physics Commons](#), and the [Physics Commons](#)

Recommended Citation

Schneider, Christopher William, "Stray Radiation Dose from X-ray and Proton Beam Radiation Therapies" (2019). *LSU Doctoral Dissertations*. 4971.

https://repository.lsu.edu/gradschool_dissertations/4971

This Dissertation is brought to you for free and open access by the Graduate School at LSU Scholarly Repository. It has been accepted for inclusion in LSU Doctoral Dissertations by an authorized graduate school editor of LSU Scholarly Repository. For more information, please contact gradetd@lsu.edu.

STRAY RADIATION DOSE FROM X-RAY AND PROTON BEAM RADIATION THERAPIES

A Dissertation

Submitted to the Graduate Faculty of the
Louisiana State University and
Agricultural and Mechanical College
in partial fulfillment of the
requirements for the degree of
Doctor of Philosophy

in

The Department of Physics and Astronomy

by
Christopher William Schneider
B.S., Southeastern Louisiana University, 2010
August 2019

For my wife and partner, Caroline. This chapter in our life together is closing, but the best is yet to come. I have learned many things on this journey, but the most important thing I have learned is this; The Doctors Schneider make a pretty great team.

Je t'aimerais pour l'éternité.

Acknowledgments

I wish to thank my advisor, Dr. Wayne Newhauser, for teaching by example what it means to be a dedicated, productive, and ethical physicist and researcher. His commitment to shaping me as a professional never wavered, and I will always be proud to call him mentor, colleague, and friend.

I am grateful to my advisory committee including Dr. Robert Carver, Dr. Jonas Fontenot, Dr. Ravi Rau, and Dr. Rui Zhang, for their invaluable advice and feedback on my project. I also could not have completed this work without the support, both professional and moral, of my colleagues in Dr. Newhauser's research group, particularly Will Donahue and Lydia Wilson.

Special thanks are due to the many international collaborators that have been a part of this work. I would like to thank Dr. Ralf-Peter Kapsch for his collaboration in the measurement campaign at the *Physikalisch-Technische Bundesanstalt* (PTB) in Braunschweig, Germany. Also from PTB, I thank Markus Meier, Larissa Miller, and Markus Schrader for their invaluable support during the measurement campaign. For their help and advice during my time as a Chateaubriand Fellow in Paris, I thank Dr. Jad Farah of *l'hôpital Bicêtre* and Alejandro Mazal and Ludovic de Marzi of the *Centre de protonthérapie de l'institut Curie*. Additionally, many thanks to the members of Working Group 9 of the European Radiation Dosimetry Group (EURADOS).

I must also thank the following for providing partial funding for this work: the Bella Bowman Foundation, the Louisiana Board of Regents, the Nuclear Regulatory Commission, the Embassy of France in the United States, and the *Physikalisch-Technische Bundesanstalt*.

Thank you to my wife, Caroline, for her unfailing moral support, and for always being willing to lend her keen eye and analytical mind to proof and critique the many revisions of this document. And finally, thank you to my parents, Mike and Carol Schneider, for a lifetime of love and support.

Table of Contents

ACKNOWLEDGMENTS	iii
LIST OF TABLES	vi
LIST OF FIGURES	viii
ABSTRACT	xii
CHAPTER	
1. INTRODUCTION	1
1.1. External Beam Radiation Therapy	1
1.2. Megavoltage X-Ray Radiation Therapy	1
1.3. Proton Therapy	6
1.4. Motivation and Purpose	9
1.5. References	11
2. AN ANALYTICAL MODEL OF LEAKAGE NEUTRON EQUIV- ALENT DOSE FOR PASSIVELY-SCATTERED PROTON RA- DIOTHERAPY AND VALIDATION WITH MEASUREMENTS	16
2.1. Introduction	16
2.2. Methods	17
2.3. Results	24
2.4. Discussion	31
2.5. Conclusion	33
2.6. References	34
3. A DESCRIPTIVE AND BROADLY APPLICABLE MODEL OF THERAPEUTIC AND STRAY ABSORBED DOSE FROM 6 MV TO 25 MV PHOTON BEAMS	37
3.1. Introduction	37
3.2. Methods and Materials	39
3.3. Results	50
3.4. Discussion	57
3.5. Conclusion	59
3.6. References	59
4. A PHYSICS-BASED ANALYTICAL MODEL OF ABSORBED DOSE FROM PRIMARY, LEAKAGE, AND SCATTERED PHO- TONS FROM MEGAVOLTAGE RADIOOTHERAPY WITH MLCS	63
4.1. Introduction	63
4.2. Methods and Materials	65
4.3. Results	87
4.4. Discussion	98

4.5. References	99
5. PHOTONEUTRON FLUENCE AND ABSORBED DOSE FROM 25-MV EXTERNAL BEAM X-RAY RADIOTHERAPY	104
5.1. Introduction	104
5.2. Methods	106
5.3. Results	111
5.4. Discussion	115
5.5. References	116
6. EXTERNAL AND INTERNAL NEUTRON ABSORBED DOSE FROM PROTON RADIOTHERAPY	118
6.1. Introduction	118
6.2. Methods	118
6.3. Results	120
6.4. Discussion	124
6.5. References	125
7. CONCLUSION	126
7.1. Implications	126
7.2. Coherence with the Literature	127
7.3. Future Work	128
7.4. References	129
APPENDIX. PUBLICATION AGREEMENTS AND PERMISSIONS	131
VITA	133

List of Tables

2.1. Parameters of power law relationship for $(H/D)_{E,iso}$.	28
2.2. Parameters for $C_i(E)$ equations to apportion equivalent dose from neutron energy regimes.	28
2.3. Neutron attenuation parameters and Gaussian width parameters for the four neutron regimes.	29
2.4. Average local relative error ($\bar{\Delta}$) and maximum local relative error ($\Delta _{max}$) for the analytical model of the general purpose beam-line from this work and Perez-Andujar et al. [14].	29
2.5. Model parameters for ocular beam-line.	30
3.1. Comparison of model terms for Jagetic and Newhauser [26] and this work.	40
3.2. Manufacturers, machines, techniques, nominal photon energies, and measurement phantoms considered in this study.	47
3.3. Average and maximum local relative differences for all nominal photon beam energies E for the model calculations compared with the Klinikum Goethe Universität (KGU) data set.	50
3.4. Average and maximum local relative differences for all nominal photon beam energies and depths for the model calculations compared with the EURADOS data set.	53
3.5. Model parameters for model as trained on the KGU and EURADOS data sets and the relative differences between the results for each.	55
3.6. Gamma index criteria for selected pass rates.	57
4.1. Measurement conditions for all absorbed dose profiles scanned in of this work.	67
4.2. Conditions for all Monte Carlo simulations performed as part of this work.	88
4.3. Empirical parameter values for parameterizations average photon energy.	88

4.4. Gamma index passing rates of the analytical model compared with the training data-set (Monte Carlo). The distance-to-agreement criterion is 3 mm.	93
4.5. Gamma index passing rates of the analytical model compared with the validation data-set (measurements). The distance-to-agreement criterion is 3 mm.	93
5.1. Selected measurement conditions for total absorbed dose profiles presented in this work.	106
5.2. Neutron energy regime definitions and number of energy bins in each regime.	107
5.3. Model inputs calculated from Monte Carlo data and model fitting parameters.	114
6.1. Off-axis distances, ρ , at which absorbed dose from external neutrons overtakes that of internal neutrons for three proton beam energies and depths in water.	123

List of Figures

1.1.	Illustration of bremsstrahlung.	2
1.2.	Simplified illustration of a megavoltage x-ray therapy beam setup.	3
1.3.	Illustration of the different sources of stray radiation.	4
1.4.	ENDF/B-VII photoneutron production cross-sections versus photon energy for Tungsten-183 and Beryllium-9 [18].	6
1.5.	Illustration of the Bertini model of the intranuclear cascade process.	8
1.6.	Typical neutron spectrum at isocenter for a 250-MeV proton beam produced via the passive scattering technique.	9
2.1.	Geometry of a general-purpose proton treatment head and water phantom. Adapted from Perez-Andujar et al. [14].	19
2.2.	Geometry of a proton therapy system for ocular treatments and positioning of the neutron equivalent dose meters.	23
2.3.	H/D_{iso} values versus proton beam energy, E	25
2.4.	Predictions from Monte Carlo and analytical model of neutron equivalent dose per treatment dose (H/D) values versus depth in water from proton beams.	25
2.5.	Predictions from Monte Carlo and analytical model of neutron equivalent dose per treatment dose (H/D) versus depth in water at 10-cm off-axis.	26
2.6.	Predictions from Monte Carlo and analytical model of neutron equivalent dose per treatment dose (H/D) versus depth in water at 40-cm off-axis.	26
2.7.	Predictions from Monte Carlo and analytical model of neutron equivalent dose per treatment dose (H/D) versus depth in water at 80-cm off-axis.	27
2.8.	Predictions from Monte Carlo and analytical model of neutron equivalent dose per treatment dose (H/D) versus off-axis position at 22-cm depth in water.	27
2.9.	Plot of C_i values for each neutron energy regime versus proton beam energy.	28

2.10.	Measured and calculated H/D values for the ocular beam-line plotted vs distance from isocenter.	30
3.1.	Functional form of the leakage dose, D_L , versus off-axis distance, x	46
3.2.	Measured and calculated relative absorbed dose $D(x)/D(0)$ versus off-axis position x for all beam energies from the Klinikum Goethe Universität (KGU) data set.	51
3.3.	Measured and calculated relative absorbed dose $D(x)/D(0)$ versus off-axis position x from the 6 MV beam at 1.5 cm depth in water from the KGU data set.	51
3.4.	Measured and calculated relative absorbed dose $D(x)/D_{\text{iso}}$ versus off-axis position x from the European Radiation Dosimetry Group (EURADOS) data set.	52
3.5.	Measured and calculated relative absorbed dose $D(x)/D(0)$ versus off-axis position x for the 6 MV beam at 10 cm depth in water from the EURADOS data set.	53
3.6.	Relative absorbed dose $D(x)/D(0)$ versus off-axis position x in anthropomorphic phantom from irradiations by various treatment techniques and machines.	56
4.1.	Photograph of measurement setup.	67
4.2.	Cross-sectional schematic view of linac head illustrating the relative locations of the beam-modifying and beam-limiting devices.	68
4.3.	Cutaway illustration showing a 3D drawing of half of the primary collimator.	74
4.4.	Schematic cross-sectional view of an MLC leaf.	76
4.5.	2-dimensional drawing of an MLC leaf illustrating the types of rays that must be considered.	79
4.6.	3-dimensional schematic drawing of secondary collimator leaves.	79
4.7.	Monte Carlo simulations of energy fluence from the uncollimated photon source.	89
4.8.	Results of Monte Carlo simulation of a $10 \times 10\text{-cm}^2$ collimated photon beam incident on large water-box phantom.	90

4.9.	Mean photon energy <i>versus</i> distance from photon-beam central axis at 10-cm depth in water from a 6-MV, 10×10-cm ² field.	90
4.10.	Monte Carlo simulated and analytical model calculated head-scattered energy fluence.	91
4.11.	Monte Carlo simulated and analytical model calculated patient-scattered energy fluence.	92
4.12.	Monte Carlo simulation and analytical model calculated photon energy fluence.	92
4.13.	2-dimensional plot of the absorbed dose for a 6-MV 10×10 cm ² field at a depth of 10 cm in water as calculated by the analytical model.	94
4.14.	Absorbed dose to the water-box phantom for case of a 10×10-cm ² field.	95
4.15.	Absorbed dose to the water-box phantom for case of a 5×5-cm ² field at a depth of 10 cm.	95
5.1.	Typical photoneutron energy spectrum, Ψ , at isocenter for a 25-MV beam in air.	105
5.2.	Typical photoneutron energy fluence spectrum, Ψ , at $d = 10$ cm in water for a 25-MV beam with a source-to-surface distance (SSD) of 90 cm.	105
5.3.	Cross-sectional schematic diagram of the linac head.	107
5.4.	Measured and simulated dose (D) versus depth (z) of a 25-MV photon beam with a field size of 10×10 cm ² along the beam's central axis in water.	111
5.5.	Measured and simulated absorbed dose (D) versus lateral position (x) of a 25-MV, 10×10 cm ² photon beam at four depths in water.	112
5.6.	Measured and simulated absorbed dose (D) versus lateral position (y) of a 25-MV, 10×10 cm ² photon beam at four depths in water.	112
5.7.	Half-profile of neutron fluence, Φ_n , predicted by Monte Carlo and analytical model.	113

5.8.	Half-profile of neutron absorbed dose with neutron energy groups.	113
5.9.	Log scale plot showing half-profile of neutron absorbed dose with neutron energy groups.	114
6.1.	Monte Carlo simulation vault geometry. The inset shows a magnified view of the treatment head and phantom.	119
6.2.	Spectral neutron energy fluence, Ψ_n , on central axis at 10-cm depth in water for all proton beam energies considered.	120
6.3.	Spectral neutron energy fluence, Ψ_n , 10 cm off-axis at 10-cm depth in water for all proton beam energies considered.	120
6.4.	Spectral neutron energy fluence, Ψ_n , from all neutrons, external neutrons, and internal neutrons on central axis at 10-cm depth in water for the 219-MeV proton beam.	121
6.5.	Spectral neutron energy fluence, Ψ_n , from all neutrons, external neutrons, and internal neutrons 10-cm off-axis at 10-cm depth in water for the 219-MeV proton beam.	121
6.6.	Neutron absorbed dose, D_n , along the proton beam's central axis for several proton beam energies.	122
6.7.	Neutron absorbed dose, D_n , from all neutrons, external neu- trons, and internal neutrons along the proton beam's central axis for the 219-MeV beam.	122
6.8.	Total absorbed dose, D , for the 219-MeV beam versus off-axis distance, ρ , at a depth of 10 cm in water.	123

Abstract

The growing population of cancer survivors at risk of radiation induced side-effects is a public health concern. These side-effects include serious conditions such as second cancers, the majority of which occur outside of the primary treatment volume. Radiotherapy treatment planning systems systematically underestimate the dose to tissues out-of-field. Attempts to predict and reduce the risks of radiogenic side effects require accurate and personalized knowledge of the out-of-field radiation dose to patients. The long-term goal of this research is to provide clinical and research tools necessary to reduce the risk of radiotherapy side effects and improve the health outcomes of radiotherapy patients. The goal of this dissertation was to characterize the stray radiation from external beam radiation therapy, including megavoltage x-ray therapy and proton therapy.

Chapter 1 gives a brief primer on radiation therapy and a summary of the state of knowledge regarding stray radiation exposures. In Chapter 2, we developed an analytical model of leakage neutron exposures from passively scattered proton therapy based on Monte Carlo simulations and measurements from two proton therapy facilities. Predicted neutron equivalent doses agreed with simulations and measurement to within 15%. In Chapter 3, we developed a broadly applicable model of stray photon radiation from conventional x-ray therapy. Predicted doses agreed with corresponding measurements to within 10% for two treatment machines and five photon beam energies. In Chapter 4, we report measurements, simulations, and a physics-based analytical model of stray photon radiation that realistically models transmission through complex collimator shapes. A gamma index analysis comparing predicted and measured doses found an 89.3% passing rate for criteria of 3-mm distance-to-agreement, 3% dose difference in-field, and 3-mGy/Gy dose difference out-of-field. Chapter 5 presents a model of photoneutron exposures from x-ray radiotherapy. Predicted absorbed doses agreed with simulations within 10%. In Chapter 6, we describe the simulation of external and internal neutron radiation from a compact proton therapy facility. External neutrons were the greatest source of dose out-of-field, but internal neutron dose was greater

than external neutron dose near the field-edge. Chapter 7 summarizes the results presented in this dissertation. Our major finding is that fast, accurate analytical models of stray radiation dose are feasible.

Chapter 1.

Introduction

1.1. External Beam Radiation Therapy

Radiation therapy, also known as radiotherapy, is a medical therapy that utilizes ionizing radiation for the purpose of treating disease, including arteriovenous malformation (AVM), trigeminal neuralgia, and, most commonly, cancer. Research into the therapeutic use of ionizing radiation began shortly after the discovery of x-rays by Wilhelm Röntgen in 1895 [1]. Along with surgery and chemotherapy, radiation therapy forms the triad of therapies at the center of modern cancer treatment. External beam radiation therapy is the most common form of radiation therapy and makes use of an external radiation source directed at the area of the patient to be treated [2]. Importantly, external beam radiation therapy can further be classified into subtypes based on the type and energy of radiation employed.

1.2. Megavoltage X-Ray Radiation Therapy

The most common form of external beam radiation therapy is megavoltage x-ray therapy and is delivered via electron linear accelerators, commonly referred to as linacs. X-ray photons are generated by impinging a narrow beam of high-energy electrons onto a target made of a high-Z material such as tungsten. The term *megavoltage* refers to the potential difference experienced by the electrons as they pass through the linac. Typical accelerating potentials range from 4- to 25-MV.

The process by which high-energy electrons incident on a target produce x-rays is known as bremsstrahlung, which comes from the German for “braking radiation.” When a negatively charged electron passes near the positively charged nucleus of an atom in the target material, the attraction causes the electron to be deflected from its initial path and to lose energy. A bremsstrahlung photon is emitted with an energy equal to the energy lost by the electron such that energy and momentum are conserved. An illustration of the bremsstrahlung process is shown in Figure 1.1. When a beam of megavoltage electrons

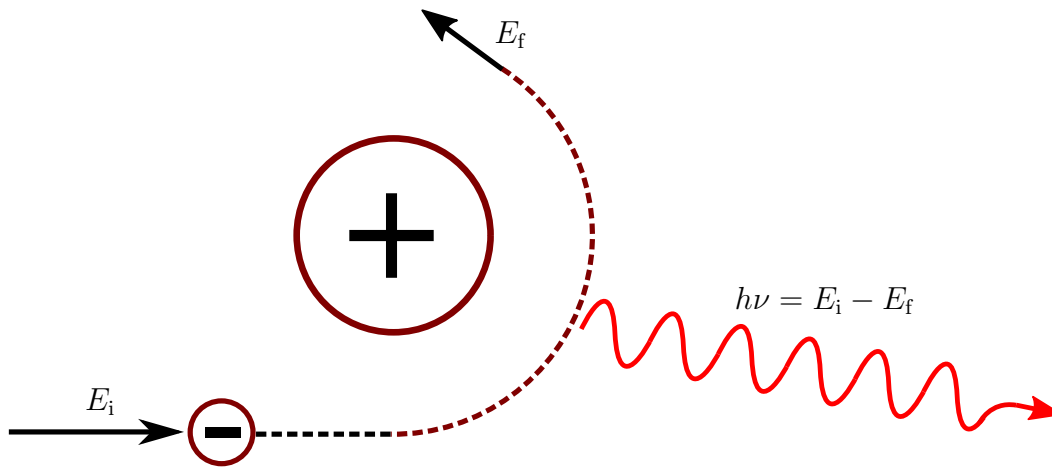


Figure 1.1. Illustration of bremsstrahlung. An incident electron of energy E_i passes near a target nucleus. The electron loses kinetic energy, and its path curves toward the nucleus. The electron emits a photon of energy $h\nu = E_i - E_f$, where E_f is the final energy of the electron, ν is the frequency of the emitted photon, and h is Planck's constant.

is incident upon a target of thickness similar to the stopping length of the electrons, the resulting beam of photons is forward peaked, but broad, with a continuous energy spectrum of photons between zero and the maximum energy of the incident electrons. As a rule of thumb, the mean energy of the resulting x-ray beam will be approximately one-third the energy of the electron beam [3].

The goal of radiation therapy is to deliver conformal dose of radiation to the target volume while sparing normal tissue as much as possible, and so it is necessary to shape the broad beam of x-rays produced in the target. Figure 1.2 shows a simplified, 2-dimensional drawing of the linac head components that shape and monitor the x-ray beam. After the bremsstrahlung field is produced in the target, the conical aperture of the primary collimator limits the maximum possible dimensions of the primary treatment field. A filter is designed to preferentially attenuate those photons on and near the central-axis, where the beam's fluence peaks, in order to create a laterally flat dose distribution at a depth of 10 cm in water. Transmission monitor chambers are used to monitor to the dose rate and total dose delivered to ensure the machine output is as expected and is designed to minimize its perturbation of the radiation field. Secondary collimators provide the final collimation of the field to the desired size and shape. Modern radiotherapy linacs have separate secondary

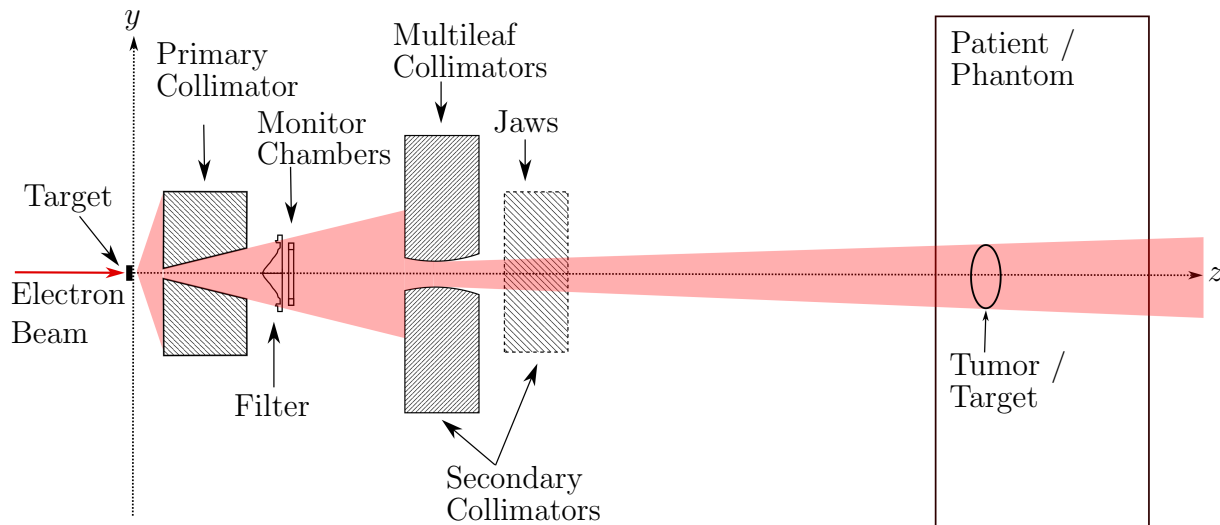


Figure 1.2. Simplified illustration of a megavoltage x-ray therapy beam setup. Important components of the linac head for producing and shaping the treatment field are labeled. The shaded region represents the x-ray field.

collimators that travel along orthogonal axes. These are commonly referred to as x - and y -axis collimators. However, it should be noted that the secondary collimator structure can rotate about the beam’s central axis, and so the x - and y -axes in the collimator frame may not coincide with those of the patient frame.

While Figure 1.2 depicts an ideal case in which no radiation reaches the patient outside of the treatment field, in practice, it is never possible to stop all stray radiation. The result is that the patient’s healthy tissues receive a “radiation bath” of doses that are on the order of grays for tissues very near the target volume and centigray to milligray for the most distant tissues [4, 5]. Nearly all of this stray radiation dose is deposited by four main sources: leakage, head-scatter, patient-scatter, and photoneutron contamination [6]. These sources are described below and illustrated in Figure 1.3.

Leakage radiation exposure occurs because a fraction of the primary x-rays incident on the collimators and other beam limiting devices in the head will escape without being attenuated [6]. The International Electrotechnical Commission mandates that the absorbed dose rate due to radiation, excluding neutrons, emanating from the head shielding of a

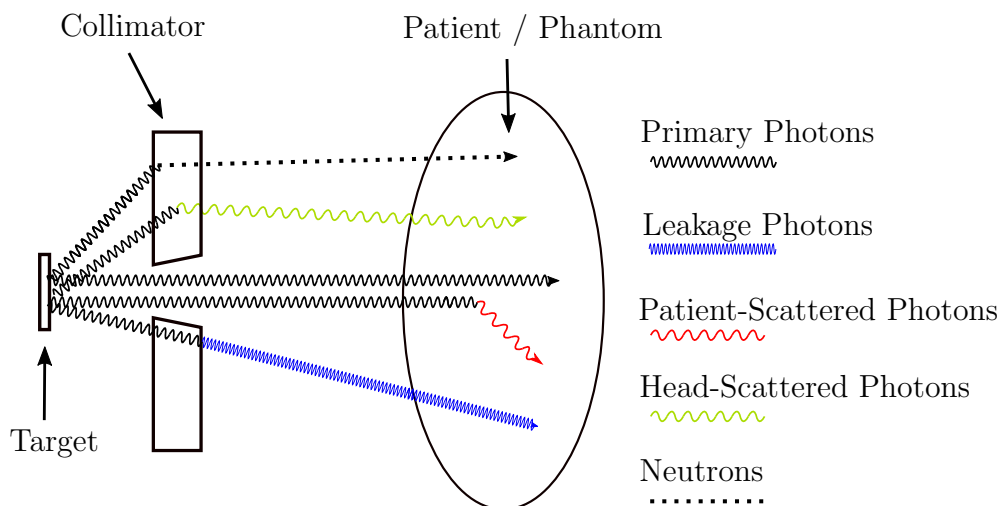


Figure 1.3. Illustration of the different sources of stray radiation.

medical linac be limited to a maximum of not more than 0.2% and an average of not more than 0.1% of the absorbed dose rate on the central-axis of a 10×10 cm² field [7]. Another consequence is that the leakage spectrum will be significantly hardened and have an average energy greater than that of the primary field.

Scattered x-rays are another important source of stray radiation [8, 9]. This is because, for photon beams in the clinical range of beam energies, Compton scattering is the most likely mechanism of interaction in matter [3]. Photons generated by scattering events in the components of the linac head are classified as head scatter, and those photons that scatter inside the patient or phantom are known as patient scatter. Since a scattered photon will be lower in energy than the incident photon, head- and patient-scatter radiation will be of lower average energy than the primary beam.

Another important source of stray radiation from megavoltage x-ray therapy is photoneutron contamination [10, 11]. Neutron contamination of clinical photon beams results primarily from photons undergoing nuclear reactions (γ, n) with the nuclei of high-Z atoms in the treatment head. Electroneutron ($e, e'n$) interactions can also be a source of neutron contamination, but these interactions are less likely than photoneutron interactions by around two orders of magnitude [12]. The primary mechanism of interaction for photoneutron production is the giant dipole resonance [13]. The giant dipole resonance

can be described as a collective excitation of the nucleus in which the protons oscillate against the neutrons [14]. The nucleus can then relax via the emission of one or more particle types including protons (γ, p), deuterons (γ, d), alphas (γ, α), and neutrons (γ, n); however, the ranges of any charged particles emitted will typically be below 1 mm, and so only the neutrons are dosimetrically important [15]. While the absorbed dose from photoneutron contamination is less than that from stray-photons in all cases, there is a large uncertainty in neutron relative biological effectiveness. NCRP Report No. 116 recommends a quality factor of 20 for neutrons in the range of energies produced by medical linacs, and so their contribution to equivalent dose is not negligible [16].

Unlike the other sources of stray radiation, the production of neutrons by incident photons exhibits a threshold energy. In order to liberate a neutron from the nucleus of an atom, the photon energy must be greater than the neutron separation energy. This can be thought of as the binding energy of the “last” neutron in the nucleus. The neutron separation energy, S_n , of an isotope, A_ZX , can be calculated as

$$M_{A-1}^Z X + M_n - M_A^Z X = S_n \quad (1.1)$$

where M_n is the neutron mass, $M_A^Z X$ is the isotopic mass, and $M_{A-1}^Z X$ is the mass of the isotope with one fewer neutrons. Linac collimators and other head components are primarily comprised of lead and tungsten. The lowest neutron separation energy of the naturally occurring isotopes of these elements is 6.2 MeV for tungsten-183. Because of this, it is often stated that photoneutron contamination only occurs for photon-beam energies ≥ 10 MV. However, some modern linacs come equipped with exit windows at the end of the primary collimator made of beryllium-9 typically located at the primary collimator exit, which has the lowest neutron separation energy of any stable isotope at 1.67 MeV. As

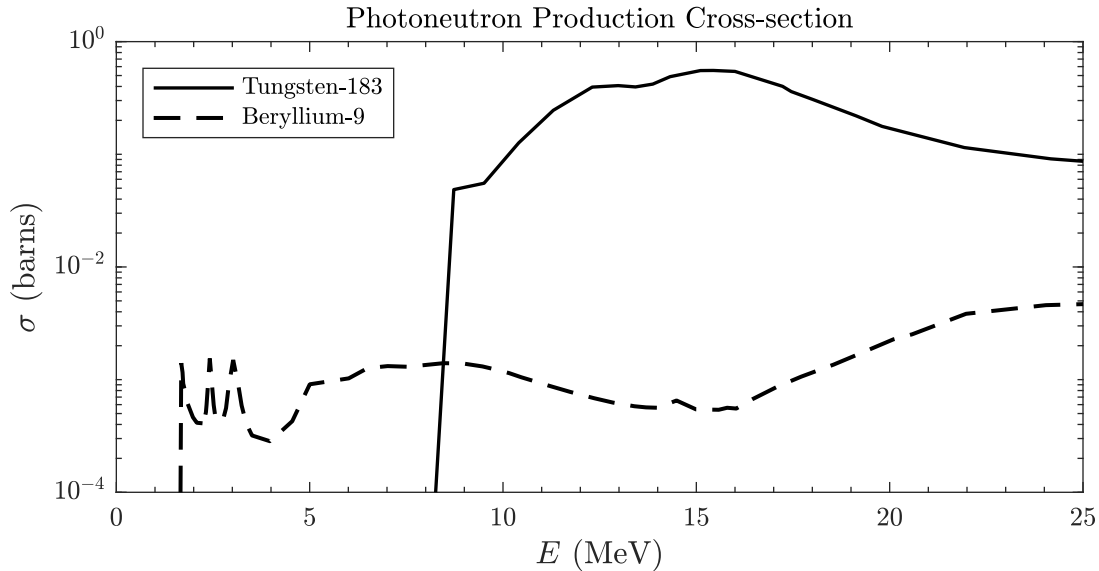


Figure 1.4. ENDF/B-VII photoneutron production cross-sections versus photon energy for Tungsten-183 and Beryllium-9 [18].

this is less than the average energy of photons in a 6-MV beam, there is the potential for neutron contamination [17]. The ENDF/B-VII photoneutron production cross-sections for tungsten-183 and beryllium-9 are shown in Figure 1.4.

1.3. Proton Therapy

Proton therapy is an emerging form of external beam radiation therapy that is becoming commonplace [19]. As of this writing, there are 31 proton centers in operation in the United States, more than half of which have existed for less than five years. At least 13 more are in various stages of planning and construction [20]. The primary motivation behind the expansion of proton therapy is its ability to deliver conformal dose distributions to target volumes while delivering a lower integral dose to the patient’s healthy tissues [21–24]. This is possible because, as massive charged particles, protons have a finite range in matter leading to near zero absorbed dose to tissues distal to the Bragg peak. Another consequence of this feature of charged particles is that, by designing collimators with thickness greater than the range of the primary protons, one can ensure that no primary protons may leak through the beam limiting devices of the treatment head.

Clinical proton beams are generated by cyclotrons or synchrotrons. Synchrotrons have the capability to select the energy of the output beam to suit the range needs of a particular treatment, but the majority of new proton centers are based on cyclotron accelerators due to their smaller footprint and lower cost compared to synchrotrons. The output energy of a cyclotron is typically fixed based on the cyclotron radius and strength of the static magnetic field, and so the proton energy must be degraded to the desired value at some point downstream in the beam-line.

The protons extracted from the accelerator are arranged in a narrow beam. There are two methods of distributing the protons to irradiate the lateral extent of a target. In passively-scattered proton therapy (PSPT), this is accomplished via the inclusion of scattering foils [24–26]. Multiple coulomb scattering in the scattering foils spread the beam laterally. Scanned-beam proton therapy (SBPT) machines make use of scanning magnets to deflect the proton pencil beam as it exits the head [24, 27, 28]. In this way, a broad dose distribution can be obtained by delivering many discrete spot beams, either one at a time or by sweeping the beam across the target [29]. An advantage of SBPT is that collimators are not necessary to shape the field. However, scanned beams delivered without collimators typically result in a broader penumbra (*i.e.*, lateral distance between the 80% and 20% isodose lines) than passive-scatter for depths $\lesssim 15$ cm [30]. Scanned-beam treatments delivered with collimators show improved penumbrae [31–33].

While the ability to deliver treatments with lower dose to the patient’s healthy tissues is an advantage of proton therapy over megavoltage x-ray therapy, there are still multiple sources of stray radiation exposure to the patient that must be considered. As previously mentioned, the leakage of primary charged particles through the treatment head shielding is not a concern for proton therapy, but primary protons may still scatter off of the edges of collimators and other beam-limited devices. These so called “edge scattered photons” can degrade the lateral penumbrae of the field and deposit stray dose in the healthy tissues surrounding the tumor volume [34, 35].

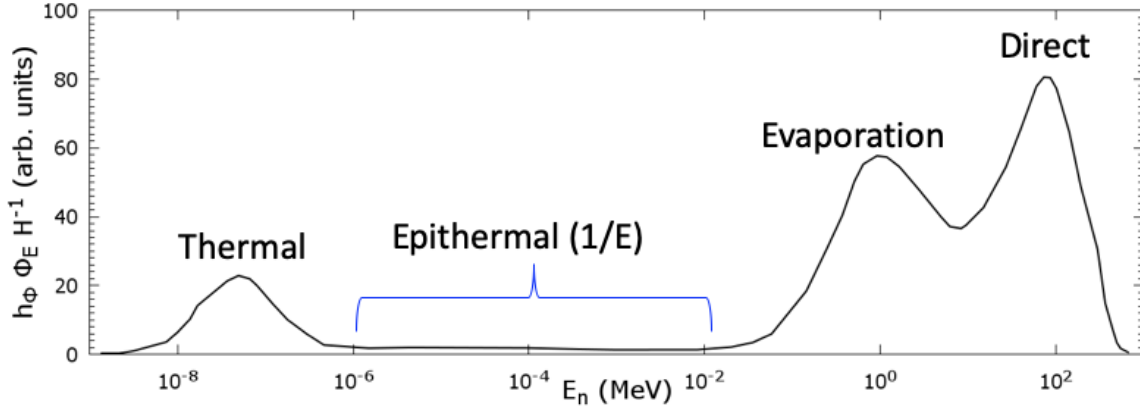


Figure 1.6. Typical neutron spectrum at isocenter for a 250-MeV proton beam produced via the passive scattering technique.

The energy spectrum of neutrons produced by a clinical proton beam can be divided into four regions, as shown by the plot of a typical spectrum in Figure 1.6. The two peaks at the upper end of the energy spectrum are comprised of the cascade and evaporation neutrons described above. There is a continuum of neutrons at the middle energies that have been partially thermalized. These are known as epithermal or $1/E$ neutrons in the literature. Finally, there is a low energy peak of thermal neutrons that will be centered around 2.5×10^{-8} MeV assuming room temperature conditions.

1.4. Motivation and Purpose

Approximately 50% of individuals will be diagnosed with cancer at some point in life [39], and in developed nations, around two-thirds of cancer patients receive radiation therapy as part of their care [40]. Improvements in cancer detection and care have led to steadily improving five-year survival rates in recent decades, surpassing 70% in adults and 80% in children [39, 41]. With the population of cancer survivors living in the United States expected to surpass 20 million by the year 2026, the need to understand and mitigate the side effects of cancer treatment is a pressing public health concern.

Cancer survivors face an increased risk of conditions including cardiac toxicity, fertility complications, and radiogenic second cancers to name just a few [5]. Cancer survivors who received radiation therapy as part of their care are twice as likely to develop

a second cancer compared with those who did not [42]. Diallo et al. [43] reports that, for a cohort of radiation therapy patients who presented with second cancers years after initial treatment, the vast majority occurred in tissues outside of the treatment volume, with 30% occurring in tissues receiving less than 2.5 Gy. In spite of this, treatment planning systems systematically underestimate the dose out of field for both x-ray and proton treatments [44–48]. To remedy this, fast and accurate methods of calculating stray radiation dose are required.

As discussed in Sections 1.1–1.3, all forms of radiation therapy result in low doses to the patient’s healthy tissues. Attempts to characterize these doses in the literature have typically followed some combination of three approaches; measurements [6, 49–51], Monte Carlo simulations [9, 52–54], and empirical parameterizations [55–59]. Measurements are a necessary first step to ensure attempts to characterize stray radiation are grounded in reality, but high quality measurements of low doses such as those found out of field are difficult to perform, require expensive equipment, and are too time consuming to be practical for routine, patient specific purposes. Monte Carlo simulations are also time consuming and computationally expensive, especially since acquiring good statistics far from the treatment field requires many more particle histories than are needed for locations in field.

Previous work from our research group has demonstrated the feasibility of using physics-based analytical models to calculate the stray radiation dose [47, 60]. The specific purpose of this dissertation has been to develop such models for the most common forms of external beam radiation therapy. Chapter 2 describes an analytical model of the external neutron dose from passively-scattered proton therapy. Chapter 3 describes a simplified model of stray radiation dose from external beam photon radiotherapy developed to test the feasibility of a simple model to calculate stray dose from multiple treatment machines. Chapter 4 describes a detailed, physics-based analytical model of stray radiation dose

from 6-MV beams delivered with an Elekta linac. Chapter 5 reports on a model of the photoneutron absorbed dose from 6–25 MV x-ray beams. Finally, Chapter 6 reports a Monte Carlo model of the internal neutron dose from to PSPT and SBPT.

1.5. References

- ¹E. C. Halperin, D. E. Wazer, C. A. Perez, and L. W. Brady, *Perez and Brady's Principles and Practice of Radiation Oncology*, 7th ed. (Wolters Kluwer, Philadelphia, 2019).
- ²ACS, *Cancer treatment & survivorship facts & figures 2016-2017* (American Cancer Society, Atlanta, 2016).
- ³F. H. Attix, *Introduction to radiological physics and radiation dosimetry* (Wiley-VCH, Weinheim, Germany, 1986).
- ⁴R. Harrison, "Introduction to dosimetry and risk estimation of second cancer following radiotherapy", *Radiat Meas* **57**, 1–8 (2013).
- ⁵W. D. Newhauser and M. Durante, "Assessing the risk of second malignancies after modern radiotherapy", *Nat Rev Cancer* **11**, 438–48 (2011).
- ⁶M. Stovall, C. R. Blackwell, J. Cundiff, D. H. Novack, J. R. Palta, L. K. Wagner, E. W. Webster, and R. J. Shalek, "Fetal dose from radiotherapy with photon beams: report of AAPM radiation therapy committee Task Group No. 36", *Med Phys* **22**, 63–82 (1995).
- ⁷IEC, *Medical electrical equipment — Part 2-1: Particular requirements for the basic safety and essential performance of electron accelerators in the range 1 MeV to 50 MeV*, IEC 60601 (International Electrotechnical Commission, Geneva, 2009).
- ⁸N. Chofor, D. Harder, A. Ruhmann, K. C. Willborn, T. Wiezorek, and B. Poppe, "Experimental study on photon-beam peripheral doses, their components and some possibilities for their reduction.", *Phys Med Biol* **55**, 4011–4027 (2010).
- ⁹N. Chofor, D. Harder, K. C. Willborn, and B. Poppe, "Internal scatter, the unavoidable major component of the peripheral dose in photon-beam radiotherapy", *Phys Med Biol* **57**, 1733–43 (2012).
- ¹⁰P. H. McGinley, M. Wood, M. Mills, and R. Rodriguez, "Dose levels due to neutrons in the vicinity of high-energy medical accelerators", *Med Phys* **3**, 397–402 (1976).
- ¹¹P. H. McGinley and E. K. Butker, "Evaluation of neutron dose equivalent levels at the maze entrance of medical accelerator treatment rooms", *Med Phys* **18**, 279–81 (1991).

- ¹²F. Biltekin, M. Yeginer, and G. Ozyigit, “Investigating in-field and out-of-field neutron contamination in high-energy medical linear accelerators based on the treatment factors of field size, depth, beam modifiers, and beam type”, *Phys Med* **31**, 517–23 (2015).
- ¹³A. Naseri and A. Mesbahi, “A review on photoneutrons characteristics in radiation therapy with high-energy photon beams”, *Rep Pract Oncol Radiother* **15**, 138–44 (2010).
- ¹⁴B. M. Spicer, “The giant dipole resonance”, in *Advances in nuclear physics*, Vol. 2, edited by M. Baranger and E. Vogt (Plenum Press, New York, 1969) Chap. 1, pp. 1–78.
- ¹⁵I. Akkurt et al., “Photoneutron yields from tungsten in the energy range of the giant dipole resonance”, *Phys Med Biol* **48**, 3345–52 (2003).
- ¹⁶NCRP, *NCRP Report No. 116 - Limitation of exposure to ionizing radiation* (National Council on Radiation Protection and Measurements, Bethesda, MD, 1993).
- ¹⁷B. Juste, S. Morato, A. Salvat, R. Miro, and G. Verdu, “Study of the photoneutron generation caused by a linac beryllium window with a 6 mev treatment beam”, *Conf Proc IEEE Eng Med Biol Soc* **2018**, 4150–4153 (2018).
- ¹⁸M. Chadwick et al., “ENDF/B-VII.0: next generation evaluated nuclear data library for nuclear science and technology”, *Nuclear Data Sheets* **107**, Evaluated Nuclear Data File ENDF/B-VII.0, 2931–3060 (2006).
- ¹⁹J. S. Loeffler and M. Durante, “Charged particle therapy—optimization, challenges and future directions”, *Nat Rev Clin Oncol* **10**, 411–24 (2013).
- ²⁰PTCOG, *Facilities in operation*, [Online] Available: <https://www.ptcog.ch/index.php/facilities-in-operation>. Particle Therapy Co-Operative Group. 2019.
- ²¹R. Miralbell, A. Lomax, L. Cella, and U. Schneider, “Potential reduction of the incidence of radiation-induced second cancers by using proton beams in the treatment of pediatric tumors”, *Int J Radiat Oncol Biol Phys* **54**, 824–9 (2002).
- ²²W. D. Newhauser, J. D. Fontenot, A. Mahajan, D. Kornguth, M. Stovall, Y. Zheng, P. J. Taddei, D. Mirkovic, R. Mohan, J. D. Cox, and S. Woo, “The risk of developing a second cancer after receiving craniospinal proton irradiation”, *Phys Med Biol* **54**, 2277–91 (2009).
- ²³R. Zhang, R. M. Howell, A. Giebeler, P. J. Taddei, A. Mahajan, and W. D. Newhauser, “Comparison of risk of radiogenic second cancer following photon and proton craniospinal irradiation for a pediatric medulloblastoma patient”, *Phys Med Biol* **58**, 807–23 (2013).
- ²⁴W. D. Newhauser and R. Zhang, “The physics of proton therapy”, *Phys Med Biol* **60**, R155–209 (2015).
- ²⁵A. M. Koehler, R. J. Schneider, and J. M. Sisterson, “Flattening of proton dose distributions for large-field radiotherapy”, *Med Phys* **4**, 297–301 (1977).

- ²⁶R. Slopsema, “Beam delivery using passive scattering”, in *Proton therapy physics* (CRC Press, Boca Raton, 2012) Chap. 5, pp. 125–156.
- ²⁷E. Pedroni, R. Bacher, H. Blattmann, T. Bohringer, A. Coray, A. Lomax, S. Lin, G. Munkel, S. Scheib, U. Schneider, and et al., “The 200-mev proton therapy project at the paul scherrer institute: conceptual design and practical realization”, *Med Phys* **22**, 37–53 (1995).
- ²⁸J. Flanz, “Particle beam scanning”, in *Proton therapy physics* (CRC Press, Boca Raton, 2012) Chap. 6, pp. 157–190.
- ²⁹G. Klimpki, Y. Zhang, G. Fattori, S. Psoroulas, D. C. Weber, A. Lomax, and D. Meer, “The impact of pencil beam scanning techniques on the effectiveness and efficiency of rescanning moving targets”, *Phys Med Biol* **63**, 145006 (2018).
- ³⁰S. Safai, T. Bortfeld, and M. Engelsman, “Comparison between the lateral penumbra of a collimated double-scattered beam and uncollimated scanning beam in proton radiotherapy”, *Phys Med Biol* **53**, 1729–50 (2008).
- ³¹C. Guardiola, C. Peucelle, and Y. Prezado, “Optimization of the mechanical collimation for minibeam generation in proton minibeam radiation therapy”, *Med Phys* **44**, 1470–1478 (2017).
- ³²Y. Prezado, G. Jouvion, D. Hardy, A. Patriarca, C. Nauraye, J. Bergs, W. Gonzalez, C. Guardiola, M. Juchaux, D. Labiod, R. Dendale, L. Jourdain, C. Sebrie, and F. Pouzoulet, “Proton minibeam radiation therapy spares normal rat brain: long-term clinical, radiological and histopathological analysis”, *Sci Rep* **7**, 14403 (2017).
- ³³L. De Marzi, A. Patriarca, C. Nauraye, E. Hierso, R. Dendale, C. Guardiola, and Y. Prezado, “Implementation of planar proton minibeam radiation therapy using a pencil beam scanning system: a proof of concept study”, *Med Phys* **45**, 5305–5316 (2018).
- ³⁴P. van Luijk, A. A. van t’Veld, H. D. Zelle, and J. M. Schippers, “Collimator scatter and 2D dosimetry in small proton beams”, *Phys Med Biol* **46**, 653–70 (2001).
- ³⁵U. Titt, Y. Zheng, O. N. Vassiliev, and W. D. Newhauser, “Monte Carlo investigation of collimator scatter of proton-therapy beams produced using the passive scattering method”, *Phys Med Biol* **53**, 487–504 (2008).
- ³⁶S. Agosteo, C. Birattari, M. Caravaggio, M. Silari, and G. Tosi, “Secondary neutron and photon dose in proton therapy”, *Radiother Oncol* **48**, 293–305 (1998).
- ³⁷X. Yan, U. Titt, A. M. Koehler, and W. D. Newhauser, “Measurement of neutron dose equivalent to proton therapy patients outside of the proton radiation field”, *Nuclear Instruments and Methods in Physics Research A* **476**, 429–34 (2002).

- ³⁸H. W. BERTINI, “Intranuclear-cascade calculation of the secondary nucleon spectra from nucleon-nucleus interactions in the energy range 340 to 2900 MeV and comparisons with experiment”, *Phys. Rev.* **188**, 1711–1730 (1969).
- ³⁹A. M. Noone, N. Howlander, M. Krapcho, D. Miller, A. Brest, M. Yu, J. Ruhl, Z. Tatalovich, A. Mariotto, D. R. Lewis, H. S. Chen, E. J. Feuer, and K. A. Cronin, eds., *SEER cancer statistics review, 1975-2015* (National Cancer Institute, Bethesda, MD, 2018).
- ⁴⁰D. Smart, *Physician characteristics and distribution in the U.S.* (American Medical Association, Chicago, IL, 2009).
- ⁴¹G. Gatta et al., “Childhood cancer survival in europe 1999-2007: results of eurocare-5—a population-based study”, *Lancet Oncol* **15**, 35–47 (2014).
- ⁴²G. T. Armstrong, M. Stovall, and L. L. Robison, “Long-term effects of radiation exposure among adult survivors of childhood cancer: results from the childhood cancer survivor study”, *Radiat Res* **174**, 840–50 (2010).
- ⁴³I. Diallo, N. Haddy, E. Adjadj, A. Samand, E. Quiniou, J. Chavaudra, I. Alziar, N. Perret, S. Guerin, D. Lefkopoulos, and F. de Vathaire, “Frequency distribution of second solid cancer locations in relation to the irradiated volume among 115 patients treated for childhood cancer”, *Int J Radiat Oncol Biol Phys* **74**, 876–83 (2009).
- ⁴⁴R. M. Howell, S. B. Scarboro, S. F. Kry, and D. Z. Yaldo, “Accuracy of out-of-field dose calculations by a commercial treatment planning system”, *Phys Med Biol* **55**, 6999–7008 (2010).
- ⁴⁵A. Joosten, O. Matzinger, W. Jeanneret-Sozzi, F. Bochud, and R. Moeckli, “Evaluation of organ-specific peripheral doses after 2-dimensional, 3-dimensional and hybrid intensity modulated radiation therapy for breast cancer based on monte carlo and convolution/superposition algorithms: implications for secondary cancer risk assessment”, *Radiother Oncol* **106**, 33–41 (2013).
- ⁴⁶U. Schneider, R. A. Halg, M. Hartmann, A. Mack, F. Storelli, A. Joosten, R. Mockli, and J. Besserer, “Accuracy of out-of-field dose calculation of tomotherapy and cyberknife treatment planning systems: a dosimetric study”, *Z Med Phys* **24**, 211–5 (2014).
- ⁴⁷L. J. Jagetic and W. D. Newhauser, “A simple and fast physics-based analytical method to calculate therapeutic and stray doses from external beam, megavoltage x-ray therapy”, *Phys Med Biol* **60**, 4753–75 (2015).
- ⁴⁸J. Eley, W. Newhauser, K. Homann, R. Howell, C. Schneider, M. Durante, and C. Bert, “Implementation of an analytical model for leakage neutron equivalent dose in a proton radiotherapy planning system”, *Cancers (Basel)* **7**, 427–38 (2015).

- ⁴⁹R. Kaderka, D. Schardt, M. Durante, T. Berger, U. Ramm, J. Licher, and C. La Tessa, “Out-of-field dose measurements in a water phantom using different radiotherapy modalities”, *Phys Med Biol* **57**, 5059–74 (2012).
- ⁵⁰K. R. Kase, G. K. Svensson, A. B. Wolbarst, and M. A. Marks, “Measurements of dose from secondary radiation outside a treatment field”, *Int J Radiat Oncol Biol Phys* **9**, 1177–83 (1983).
- ⁵¹S. F. Kry, M. Price, D. Followill, F. Mourtada, and M. Salehpour, “The use of LiF (TLD-100) as an out-of-field dosimeter”, *Journal of Applied Clinical Medical Physics* **8**, 169–175 (2007).
- ⁵²S. S. Almberg, J. Frengen, and T. Lindmo, “Monte Carlo study of in-field and out-of-field dose distributions from a linear accelerator operating with and without a flattening-filter”, *Med Phys* **39**, 5194–203 (2012).
- ⁵³B. S. Athar and H. Paganetti, “Comparison of second cancer risk due to out-of-field doses from 6-MV IMRT and proton therapy based on 6 pediatric patient treatment plans”, *Radiother Oncol* **98**, 87–92 (2011).
- ⁵⁴S. F. Kry, U. Titt, F. Ponisch, D. Followill, O. N. Vassiliev, R. A. White, R. Mohan, and M. Salehpour, “A Monte Carlo model for calculating out-of-field dose from a Varian 6 MV beam”, *Med Phys* **33**, 4405–13 (2006).
- ⁵⁵P. H. van der Giessen, “Peridose, a software program to calculate the dose outside the primary beam in radiation therapy”, *Radiother Oncol* **58**, 209–13 (2001).
- ⁵⁶M. Stovall, R. Weathers, C. Kasper, S. A. Smith, L. Travis, E. Ron, and R. Kleinerman, “Dose reconstruction for therapeutic and diagnostic radiation exposures: use in epidemiological studies”, *Radiat Res* **166**, 141–57 (2006).
- ⁵⁷P. J. Taddei, W. Jalbout, R. M. Howell, N. Khater, F. Geara, K. Homann, and W. D. Newhauser, “Analytical model for out-of-field dose in photon craniospinal irradiation”, *Phys Med Biol* **58**, 7463–79 (2013).
- ⁵⁸B. Sánchez-Nieto, R. El-far, L. Irazola, M. Romero-Expósito, J. I. Lagares, J. C. Mateo, J. A. Terrón, and F. Sánchez Doblado, “Analytical model for photon peripheral dose estimation in radiotherapy treatments”, *Biomed Phys Eng Express* **1**, 045205 (2015).
- ⁵⁹P. Hauri, R. A. Halg, J. Besserer, and U. Schneider, “A general model for stray dose calculation of static and intensity-modulated photon radiation”, *Med Phys* **43**, 1955 (2016).
- ⁶⁰A. Perez-Andujar, R. Zhang, and W. Newhauser, “Monte Carlo and analytical model predictions of leakage neutron exposures from passively scattered proton therapy”, *Med Phys* **40**, 121714 (2013).

Chapter 2.

An Analytical Model of Leakage Neutron Equivalent Dose for Passively-Scattered Proton Radiotherapy and Validation with Measurements

2.1. Introduction

In many cases, proton therapy is dosimetrically advantageous compared to other forms of external beam radiation therapy because it allows for uniform target coverage with lower doses to healthy tissues [1–3]. However, proton therapy patients are still exposed to stray radiation, which is not fully understood and not routinely estimated for most patients. Most proton beam treatments are delivered by the passive scattering technique. Stray radiation dose to the patient from passively scattered proton therapy (PSPT) primarily comes from neutrons that leak out of the treatment head [4, 5]. This is a concern because neutrons have an enhanced relative biological effectiveness compared with protons [6, 7], and even relatively small doses far from the primary treatment field increase the risk of secondary cancers [8]. Commercial treatment planning systems do not take neutron dose into account. Researchers have relied mainly on measurements and Monte Carlo-based simulation in order to learn more about neutron exposures. However, the time required for these methods is a barrier to research and routine clinical use. Thus, there is a need for fast, accurate analytical models of leakage neutron equivalent dose from proton therapy.

Polf and Newhauser [9] reported that analytical models of neutron equivalent dose from proton therapy are feasible. One proposed analytical model employed a power law to predict neutron equivalent dose per therapeutic dose (H/D) for passively scattered proton therapy for different field sizes and locations within a treatment vault [10, 11]. This model was refined for 250 MeV pristine proton beams, both in-air and in a water phantom, by Zhang et al. [12]. Anferov [13] reported a model based on shielding calculation methods to predict the equivalent dose from neutrons for 100, 150, and 200 MeV proton beams.

Adapted with permission from: Schneider, C.; Newhauser, W.; Farah, J., An Analytical Model of Leakage Neutron Equivalent Dose for Passively-Scattered Proton Radiotherapy and Validation with Measurements. *Cancers*. **2015**, *7*, 795–810. Copyright (2015) MDPI AG (Basel, Switzerland).

The most complete and realistic leakage model to date was reported by Perez-Andujar et al. [14], which takes into account four separate neutron energy regimes to predict H/D in-air and in-water for proton beams with energies between 100 and 250 MeV. The model was found to have good agreement when compared with benchmarked Monte Carlo simulations. However, this model was not continuous with proton beam-energy and required interpolation of parameters between the discrete energies considered. The model's large number of parameters made its configuration and use difficult. Furthermore, the model was not compared with measured data nor was it tested at proton beam energies below 100 MeV.

The purpose of this study was to improve an analytical model of neutron H/D by making it continuous in energy and reducing the number of free parameters, thus simplifying its configuration and use. We compared the results of this model with Monte Carlo simulated neutron H/D values between 100 and 250 MeV for a conventional proton therapy beam-line. Additionally, we configured and tested a version of the model with new H/D measurements at 75 MeV proton beam energy.

2.2. Methods

2.2.1. Analytical Model

Building upon the methods of Perez-Andujar et al. [14], we improved an analytical model for (H/D) from leakage neutrons from passively scattered proton therapy. For the reader's convenience, we briefly review the previous model here. (H/D) contributions are calculated from four neutron energy regimes: intranuclear cascade neutrons (also called direct neutrons), evaporation neutrons, epithermal neutrons (also called $(1/E)$ neutrons), and thermal neutrons. Cascade neutrons are produced when a bombarding proton interacts with a target nucleus and can have energies up to the maximum energy of the proton beam. The second highest energy regime, that of evaporation neutrons, corresponds to neutrons ejected by the excited nucleus after the initial proton collision in processes known as compound emission and pre-equilibrium emission. The third energy regime, epithermal

neutrons, corresponds to neutrons that have lost some portion of their energy via inelastic scattering and moderation. Some of these neutrons will be lost via capture processes. Finally, the lowest energy regime corresponds to thermal neutrons that have lost most of their kinetic energy and are in thermal equilibrium with the environment. These undergo elastic scattering until they are eventually captured.

The analytical model for H/D at a point, p , in a water phantom is

$$\left(\frac{H}{D}\right)_p = \left(\frac{H}{D}\right)_{E,\text{iso}} \left(\frac{d}{d_{\text{iso}}}\right)^{-q} \sum_{i=1}^4 C_i(E) \exp[-\alpha_i(d' - d'_{\text{iso}})] \exp\left[\frac{-(x^2 + y^2)d_{\text{iso}}^2}{2\sigma_i^2 z^2}\right], \quad (2.1)$$

where $(H/D)_{E,\text{iso}}$ is the total neutron equivalent dose per treatment dose at isocenter as function of the proton beam energy; d is the distance from the neutron source to the calculation point; d' is the distance along the ray, d , from the phantom surface to the calculation point; d_{iso} is the distance from the neutron source to isocenter; and d'_{iso} is the distance along the ray, d_{iso} , from the phantom surface to isocenter. The irradiation geometry, dimensions, and distances are shown in Figure 2.1. The exponent, q , governs the power law falloff of neutron dose with distance from isocenter. The $C_i(E)$ terms apportion the fraction of the total equivalent dose resulting from the each of the four neutron energy regimes. The first exponential term models neutron attenuation in the phantom. The mean free paths of the neutrons of the i^{th} regime in water are denoted by α_i , with the first exponential term modeling neutron attenuation in the phantom. The second exponential term, then, models the lateral distribution of the i^{th} neutron regime with α_i as the Gaussian width parameter.

In this work, several improvements have been made to the model. Previously, the model required interpolation of $(H/D)_{\text{iso}}$ values at proton beam energies between energies contained in the lookup tables. In this work, $(H/D)_{E,\text{iso}}$ has been parameterized with proton beam energy according to a power law relationship, or

$$\left(\frac{H}{D}\right)_{E,\text{iso}} = \alpha_E \times E^{p_E} \times \left(\frac{H}{D}\right)_{\text{ref,iso}}, \quad (2.2)$$

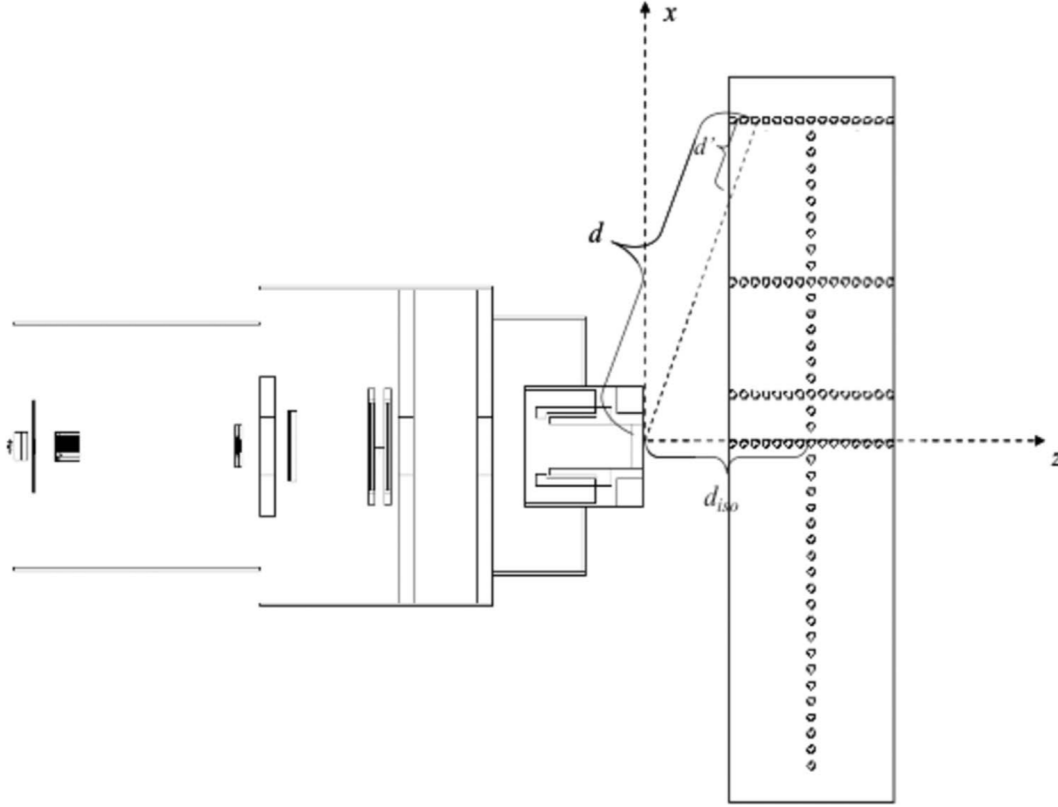


Figure 2.1. Geometry of a general-purpose proton treatment head and water phantom. Adapted from Perez-Andujar et al. [14].

where $(H/D)_{\text{ref,iso}}$ is the neutron equivalent dose value at isocenter for a proton beam of a given reference energy (100 MeV in this study), p_E is the exponent governing the power law, α_E is a scaling factor, and E is the proton beam energy. This value may be obtained from measurement or from a Monte Carlo simulation and is found by taking the quotient

$$\left(\frac{H}{D}\right)_{\text{ref,iso}} = \frac{(H/p)_{\text{ref,iso}}^{\text{closed}}}{(D/p)_{\text{ref,iso}}^{\text{open}}}, \quad (2.3)$$

where $(D/p)_{\text{ref,iso}}^{\text{open}}$ is the absorbed dose in gray per proton at isocenter found with the collimator open and $(H/p)_{\text{ref,iso}}^{\text{closed}}$ is the neutron equivalent dose in sievert per proton with the collimator closed [11].

The previous model relied on lookup tables of 32 C_i values that were found from an iterative fitting process; four values at each of the eight proton beam energies considered from 100 to 250 MeV [14]. In the improved model, the $C_i(E)$ values that apportion the contributions from each neutron regime were parameterized as functions of proton beam energy. Specifically, for intranuclear cascade neutrons, we use the linear form

$$C_1(E) = a_1E + b_1 \quad , \quad (2.4)$$

where E is the proton beam energy, a_1 is the slope, and b_1 is the intercept. For evaporation neutrons, the cumulative normal was used with a lower bound as in,

$$C_2(E) = a_2 \text{cnorm}(E, b_2, c_2) + d_2 \quad , \quad (2.5)$$

where a_2 is a scaling coefficient, d_2 is the lower bound, and the cumulative normal function with mean value b_2 and width parameter c_2 is defined in the usual way as

$$\text{cnorm}(E, b_2, c_2) = \frac{1}{c_2\sqrt{2\pi}} \int_{-\infty}^E \exp \left[\frac{-(E' - b_2)^2}{2c_2^2} \right] dE' \quad . \quad (2.6)$$

The epithermal regime was modeled as

$$C_3(E) = a_3 \quad , \quad (2.7)$$

where a_3 is a constant. For the thermal neutrons, we used

$$C_4(E) = a_4E^2 + b_4E + c_4 \quad , \quad (2.8)$$

where a_4 and b_4 and c_4 are the polynomial's second, first, and zeroth order coefficients. Since these curves are used to apportion the equivalent dose from each neutron energy regime, they were constrained so that their sum is unity. The forms of Equations 2.4, 2.5, 2.7, 2.8

and 4.37 were chosen empirically to faithfully reproduce the shapes of the C curves with energy while simultaneously reducing the number of model parameters. Specifically, the approach of Perez-Andujar et al. [14] required a lookup table containing 40 values plus 9 energy independent parameters for a total of 49 parameters. Our model requires only 13 values plus 9 energy independent parameters for a total of 22 parameters to cover the same interval of proton beam energies from 100 to 250 MeV. Parameterizing these terms with energy offers several advantages compared with the table lookup. It allows the model to be continuous in energy and reduces the number of free parameters. The values for the parameters α_E , p_E , a_1 , b_1 , a_2 , b_2 , c_2 , d_2 , a_3 , a_4 , b_4 , and c_4 were obtained via the iterative fitting process described in section 2.2.4 below.

2.2.2. Monte Carlo simulated H/D values for general purpose beam-line at 100 to 250 MeV

Previous studies [12, 14] utilized dosimetric data exclusively from Monte Carlo simulations to develop the model. In this study, we purposefully utilized the same Monte Carlo data in order to facilitate the comparison of results with and without the improvements developed in this work. The Monte Carlo data were taken from a simulation of the passive scattering system in place at The University of Texas MD Anderson Cancer Center described in detail by Perez-Andujar et al. [14]. This was accomplished with the Monte Carlo Proton Radiotherapy Treatment Planning (MCP RTP) system [15] which utilizes the Monte Carlo N-Particle eXtended (MCNPX) Radiation Transport Code [16]. MCNPX is commonly used for simulating neutron exposures and has been extensively benchmarked against measurements [17–22]. Simulations were carried out first with an open collimator to determine the primary absorbed dose per proton, D/p . Next, simulations were done with a closed final collimator to determine the neutron equivalent dose per proton, H/p , and the ratio of these yields H/D . The simulated neutron data includes nominal proton beam energies of 100, 120, 140, 160, 180, 200, 225, and 250 MeV with a closed collimator, pristine Bragg peak, and with the proton beam incident on a water phantom. The phantom contained 100 spherical

detecting volumes, each of 1-cm diameter. The detecting volumes were located along lines parallel to the beam axis at 0 cm, 10 cm, 40 cm, and 80 cm off-axis, as well as one line perpendicular to the beam axis at the depth of isocenter in the phantom (22 cm). The simulation geometry is illustrated in Figure 2.1.

2.2.3. Measure H/D for ocular beam-line at 75 MeV

Measurements of H/D for the 75 MeV proton beam were carried out at Centre de Proton thérapie d'Orsay (CPO) in France in a single-scattering proton beam-line dedicated to ocular tumor treatments. During the neutron measurements, a closed patient collimator was used together with a pristine Bragg peak. We selected 75 MeV proton beam energy because it is representative of ocular treatments at CPO. Measurements were taken in air.

Two instrument types were used to acquire neutron ambient dose equivalent, $H^*(10)$, in air. The Berthold LB 6411 [23] is a conventional neutron probe with a spherical polyethylene moderator (25 cm external diameter) and a central ^3He proportional counter (4 cm external diameter and 10 cm length). It is known to be suitable for ambient dose equivalent measurements in the energy range from thermal to 20 MeV [24]. Additionally, this rem-counter is characterized by a high rejection coefficient for gamma radiation. The WENDI-II is a survey meter with a cylindrical polyethylene moderator (22.9 cm in diameter and 21 cm long), and a central cylindrical ^3He proportional counter [25]. The moderator encloses a tungsten powder shell of 1.5 cm thickness, which enhances the accuracy of the instrument's response at energies above about 20 MeV by neutron multiplication.

The measurements of $H^*(10)$ were made at isocenter and several distances from isocenter along the proton beam axis and 45° and 90° with respect to the beam axis. Figure 2.2 shows the ocular beam line and the 10 measurement positions.

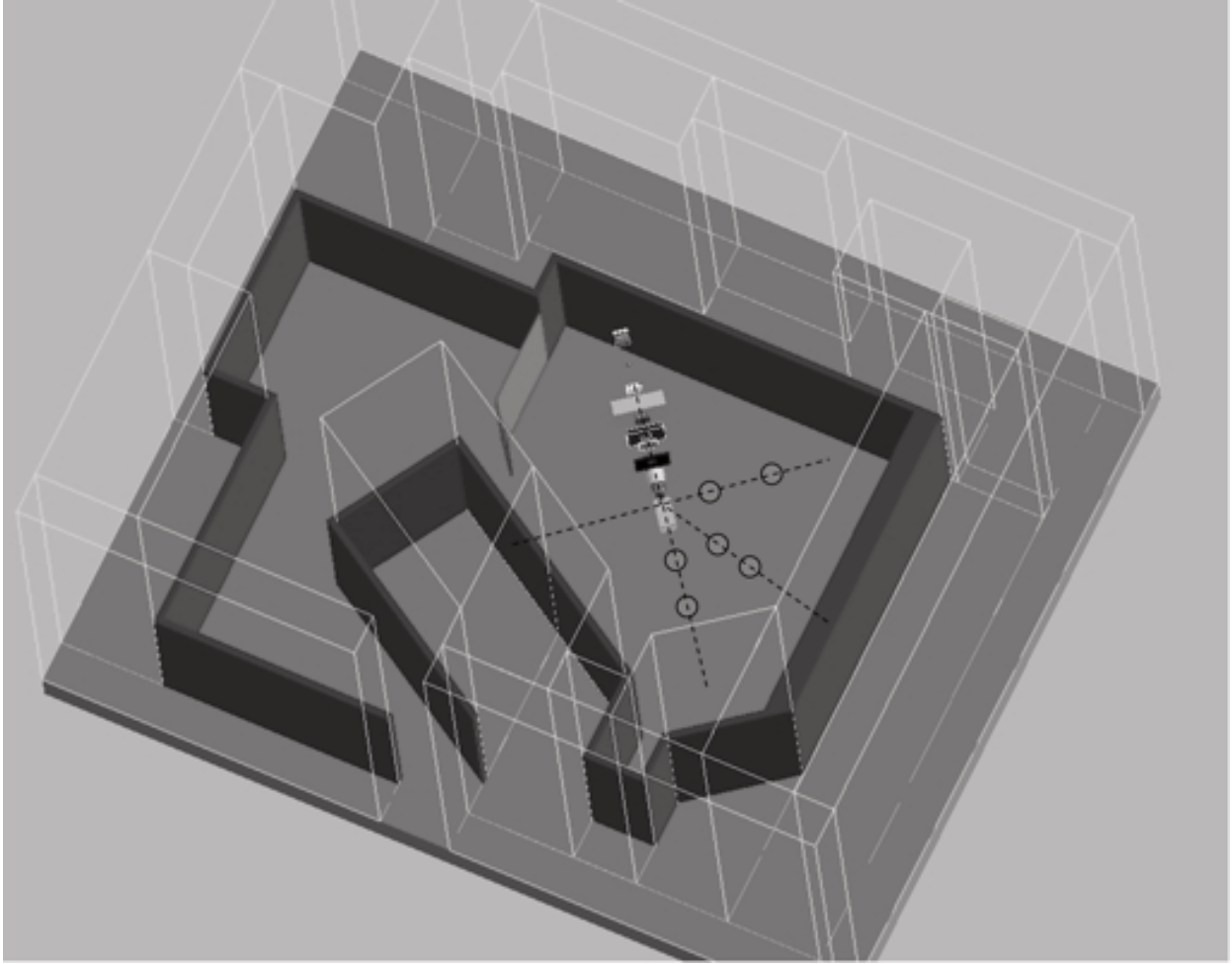


Figure 2.2. Geometry of a proton therapy system for ocular treatments and positioning of the neutron equivalent dose meters along the three axes at 0° , 45° and 90° with respect to the proton beam direction.

2.2.4. Model training

Previously, the model was trained separately at each proton beam energy considered [14]. In this work, we trained the improved model for the general purpose beam-line by fitting to all data from 100 to 250 MeV simultaneously. All free parameters were selected using the generalized reduced gradient method to minimize the local relative differences in H/D [26].

The model was trained separately for the 75 MeV measurements. This was necessary because of the considerable differences between the beam-lines. Because the measured data from the ocular beam-line consist of a single proton beam energy and measurements were

taken in air, some modifications were necessary. The α_i terms from Equation 2.1, which model neutron attenuation in water, were defined to be zero, since there is no water present. The power law model for $(H/D)_{E,\text{iso}}$ in Equation 2.2 was simply replaced with the measured H/D value at isocenter at 75 MeV. Finally, the $C_i(E)$ curves defined in Equations 2.4, 2.5, 2.7, 2.8 and 4.37 were replaced with scalar coefficients C_1 , C_2 , C_3 , and C_4 .

2.3. Results

2.3.1. Model Agreement with Monte Carlo data at 100 to 250 MeV

Figure 2.3 shows the Monte Carlo simulated and analytical model calculated values of H/D at isocenter for the general purpose and ocular beam-lines. H/D along the central axis is plotted as a function of depth in water for all energies in Figure 2.4. Figures 2.5–2.7 plot the corresponding results at off-axis distances of 10 cm, 40 cm, and 80 cm, respectively. Figure 2.8 shows lateral H/D profiles for all energies at isocenter depth (22 cm). These figures demonstrate the good agreement between the H/D values from Monte Carlo simulations and the analytical model calculations. The average relative difference between the analytical model and the Monte Carlo calculations at all proton beam energies and locations considered was 10% with a maximum difference of 60%. The maximum difference occurred for the 120 MeV proton beam energy at a location 80 cm off-axis and 19 cm deep in the phantom.

The parameters governing $(H/D)_{E,\text{iso}}$ from Equation 2.2 are shown in Table 2.1. Table 2.2 lists the parameters that govern the $C_i(E)$ curves in Equations 2.4, 2.5, 2.7, 2.8 and 4.37. Our results confirm the findings of Perez-Andujar et al. [14] that the largest contribution to H/D is from the high-energy direct neutrons followed by the epithermal neutrons. H/D from the evaporation neutron regime is more prevalent at higher energies, and the thermal neutron regime contributes a relatively small component of the equivalent dose. Figure 2.9 shows the $C_i(E)$ curves from this work plotted with proton beam energy and compared with analogous values from Perez-Andujar et al. [14]. Use of the parameterized

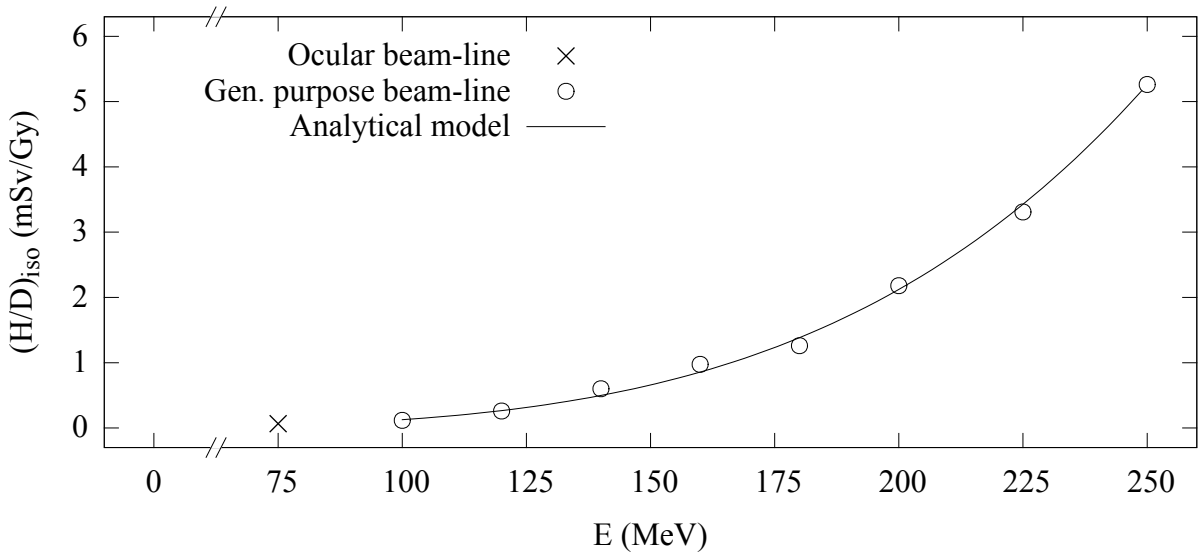


Figure 2.3. H/D_{iso} values versus proton beam energy, E . Ocular beam-line value (\times) was measured in air. General purpose beam-line values (\circ) were obtained from Monte Carlo simulations. Analytical model (line) values were calculated using Equation 2.2.

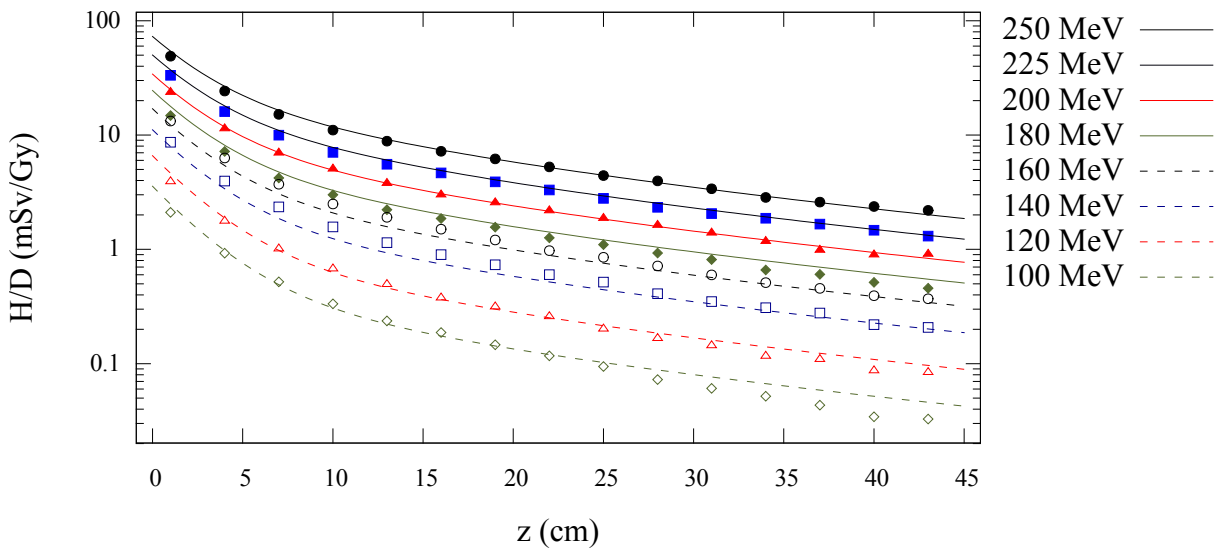


Figure 2.4. Predictions from Monte Carlo (points) and analytical model (lines) of neutron equivalent dose per treatment dose (H/D) values versus depth in water from proton beams of 100, 120, 140, 160, 180, 200, 225, and 250 MeV.

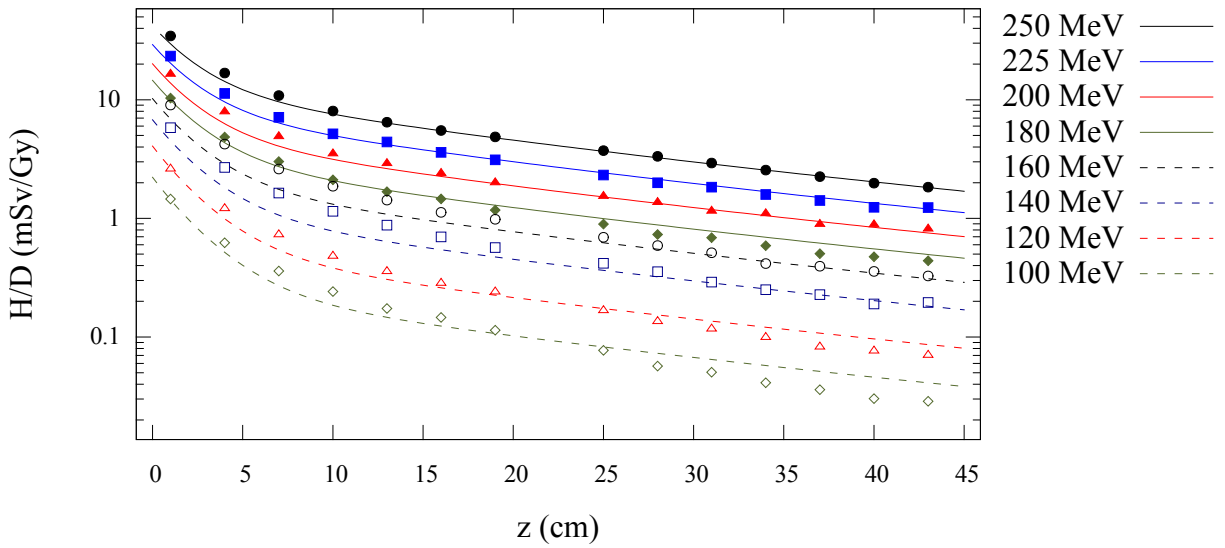


Figure 2.5. Predictions from Monte Carlo (points) and analytical model (lines) of neutron equivalent dose per treatment dose (H/D) versus depth in water at 10-cm off-axis for 100 to 250-MeV proton beam energies.

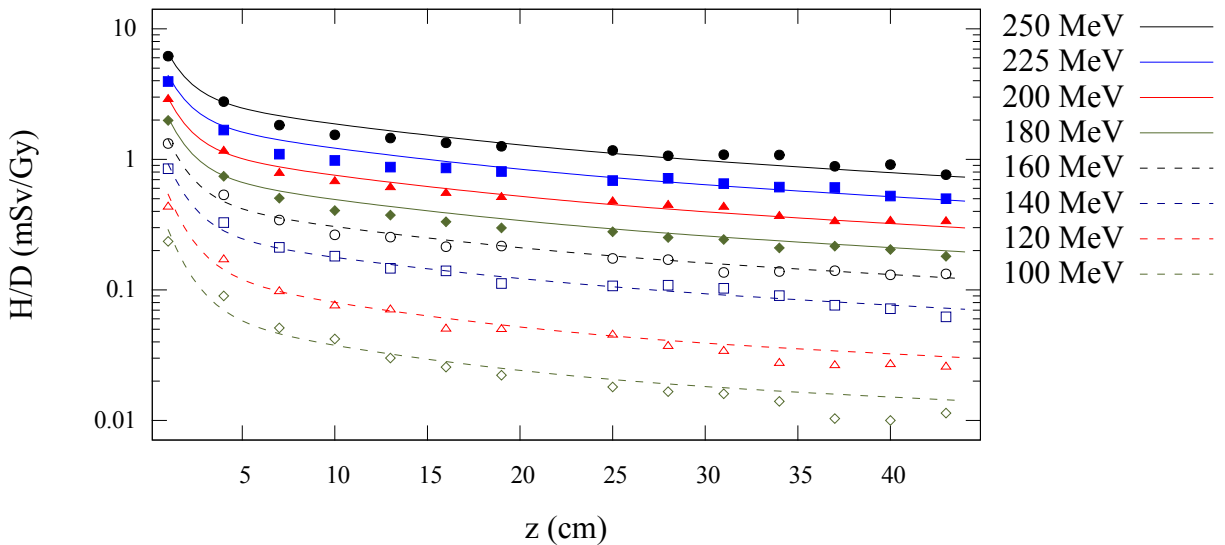


Figure 2.6. Predictions from Monte Carlo (points) and analytical model (lines) of neutron equivalent dose per treatment dose (H/D) versus depth in water at 40-cm off-axis for 100 to 250-MeV proton beam energies.

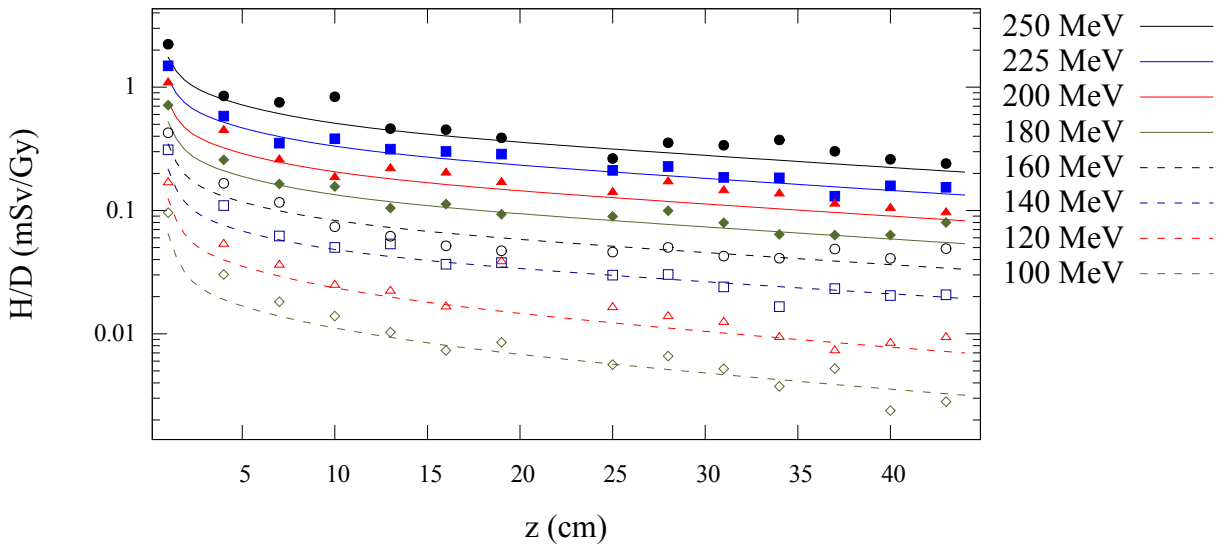


Figure 2.7. Predictions from Monte Carlo (points) and analytical model (lines) of neutron equivalent dose per treatment dose (H/D) versus depth in water at 80-cm off-axis for 100 to 250-MeV proton beam energies.

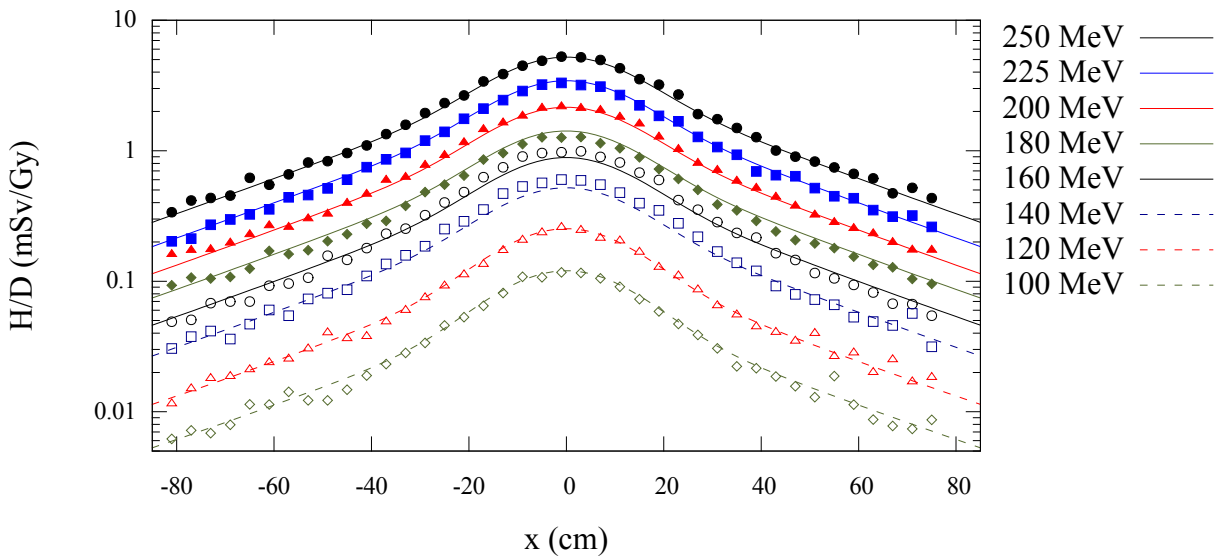


Figure 2.8. Predictions from Monte Carlo (points) and analytical model (lines) of neutron equivalent dose per treatment dose (H/D) versus off-axis position at 22-cm depth in water for 100 to 250 MeV proton beam energies.

$C_i(E)$ curves greatly reduced the difficulty of configuring the model by preventing non physical fluctuations of several parameters with energy, eliminating the need for subjective manual adjustments.

Table 2.1. Parameters of power law relationship for $(H/D)_{E,iso}$.

α_E	p_E	$(H/D)_{E,iso}$
8.0×10^{-9}	4.1×10^0	1.2×10^{-4}

Table 2.2. Parameters for $C_i(E)$ equations to apportion equivalent dose from neutron energy regimes.

Neutron Energy Regime	a_i	b_i	c_i	d_i
Intranuclear Cascade	-4.8×10^{-4}	6.0×10^{-1}	N/A	N/A
Evaporation	1.2×10^{-1}	1.3×10^2	5.0×10^0	-1.3×10^{-11}
Epithermal (1/E)	4.0×10^{-1}	N/A	N/A	N/A
Thermal	1.2×10^{-7}	-6.6×10^{-5}	1.1×10^{-2}	N/A

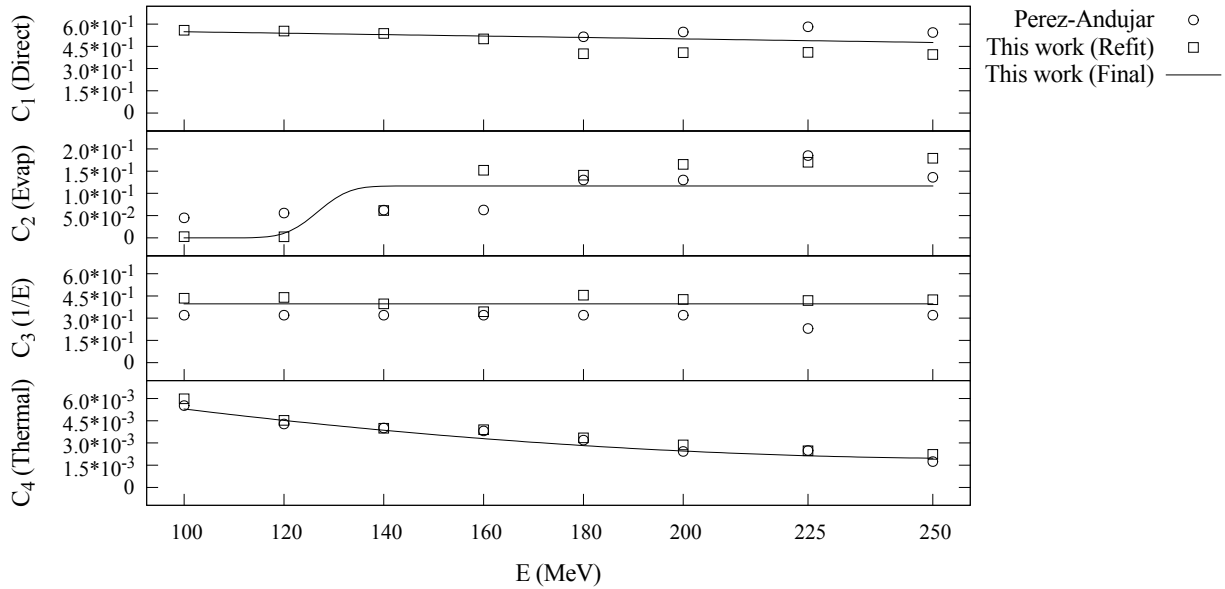


Figure 2.9. Plot of C_i values for each neutron energy regime versus proton beam energy. Points represent C_i values from Perez-Andujar et al. [14] (circles) and from a refitting of that model using the improved fitting methods (squares). The solid curves represent the parameterized $C_i(E)$ models used in the final version.

Table 2.3 lists the energy independent parameters, including the neutron attenuation factors and Gaussian width parameters. As expected, the width parameters for the low energy neutron regimes, epithermal and thermal, are very large corresponding to an isotropic distribution. The higher energy neutron regimes are forward peaked. The exponent governing falloff, q , was found to be 1.13. Table 2.4 lists a comparison of the accuracies for all locations and all energies, as well as at each specific energy, between this work and Perez-Andujar et al. [14]. We found similar agreement with the Monte Carlo simulations. The average local relative differences were within 4% of each other for all energies. The maximum local relative error was decreased from 76% to 60%.

Table 2.3. Neutron attenuation parameters and Gaussian width parameters for the four neutron regimes.

Direct		Evaporation		Epithermal		Thermal	
α_1 (cm ⁻¹)	σ_1 (cm ¹)	α_2 (cm ⁻¹)	σ_2 (cm ¹)	α_3 (cm ⁻¹)	σ_3 (cm ¹)	α_4 (cm ⁻¹)	σ_4 (cm ¹)
1.3×10^{-2}	1.4×10^2	1.3×10^{-2}	7.7×10^1	3.2×10^{-2}	3.9×10^3	3.3×10^{-1}	3.9×10^3

Table 2.4. Average local relative error ($\bar{\Delta}$) and maximum local relative error ($\Delta|_{\max}$) for the analytical model of the general purpose beam-line from this work and Perez-Andujar et al. [14].

Proton Energy (MeV)	This Work		Perez-Andujar et al. [14]	
	$\bar{\Delta}$ (%)	$\Delta _{\max}$ (%)	$\bar{\Delta}$ (%)	$\Delta _{\max}$ (%)
All	10	60	10	76
250	7	39	7	30
225	7	29	6	29
200	7	31	56	34
180	11	31	7	34
160	11	33	10	45
140	11	45	10	46
120	11	60	15	61
100	16	54	18	76

2.3.2. Model agreement with measured data at 75 MeV

Measured and calculated H/D values for the ocular beam-line data are shown in Figure 2.10 with separate plots for each of the rays measured along: 0°, 45°, and 90° with respect to the beam axis. The plot shows good agreement between measured values and

the analytical model. We conservatively estimated the uncertainty in the measured data at $\pm 25\%$, and the calculated H/D values agreed within this limit for all points considered. The average error was 16% and the maximum error was 24%. The exponent that governs falloff, q , was found to be 1.5. The larger q value is expected in this instance since the ocular beam-line is narrower and should more closely resemble a point source. The parameters C_1 – C_4 , σ_1 – σ_4 , and H/D_{iso} for the ocular beam-line data are listed in Table 2.5.

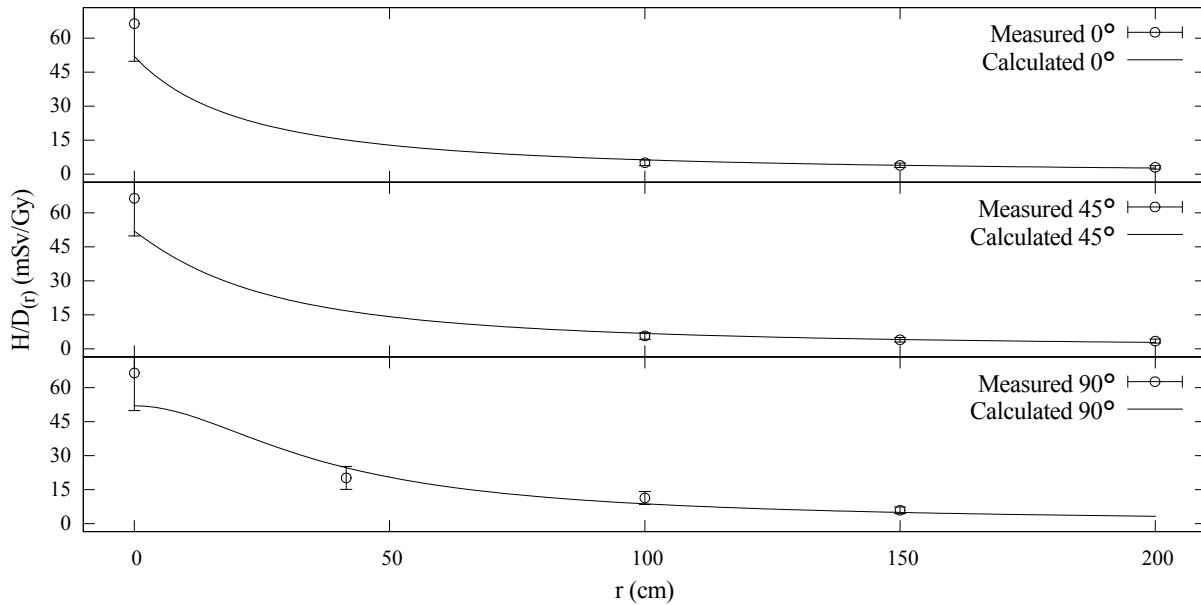


Figure 2.10. Measured (circles) and calculated (lines) H/D values for the ocular beam-line plotted vs distance from isocenter. The top plot shows data taken along the beam axis with points distal to isocenter. The middle plot shows the values along a ray 45° with respect to the beam axis. The lower plot shows values directly lateral to isocenter, *i.e.*, along a ray 90° with respect to the beam axis.

Table 2.5. Model parameters for ocular beam-line.

C_1	C_2	C_3	C_4	σ_1 (cm)	σ_2 (cm)	σ_3 (cm)	σ_4 (cm)	$(H/D)_{\text{iso}}$ (mSv/Gy)
1.1×10^{-2}	7.8×10^{-1}	1.0×10^{-1}	9.6×10^{-2}	9.4×10^{-2}	1.0×10^3	4.2×10^3	4.2×10^3	5.2×10^{-5}

2.4. Discussion

We have improved an analytical model for predicting H/D from leakage neutrons for proton therapy by parameterization of energy dependent aspects of the model, thereby reducing the number of free parameters and simplifying the model configuration process. We have demonstrated the training of this model using Monte Carlo simulated neutron exposures for proton beam energies from 100 to 250 MeV and using measured data from a separate 75 MeV proton therapy beam-line.

The major finding of this work is that an analytical model of neutron H/D for passively scattered proton therapy may be applied continuously over a wide range of proton beam-energies with relatively few model parameters. In addition to reducing the number of free parameters, explicitly modeling the contribution of different neutron energy regimes based on the proton beam energy yields other advantages to our model. The model is now continuous in energy, and this approach obviates the need to interpolate from a table of values at intermediate energies. The model can be easily applied to energies between those used in the work without the need for additional measurements or crude linear interpolation. In contrast, the lookup table approach employed by Perez-Andujar et al. [14] requires the interpolation of several parameters for use at energies other than those contained in the lookup table and also requires a large number of energy specific parameters that complicate the training of the model. Our method reduces the number of free parameters, and our improved fitting methods have made the model training process much simpler for the user. This approach gives confidence that the fitted parameters follow physically realistic dependencies on proton beam energy and are not the result of over-fitting or memorizing the data.

Another encouraging confirmatory finding is that the analytical model is applicable to low energy proton beams such as those used in ocular treatments. It is important that the model be easily adaptable to other passive scattering treatment systems, so that it can

have the greatest possible impact and find use at many different institutions. Importantly, Farah et al. [27] previously reported on the difficulty in configuring the original model, an obstacle that this work has successfully overcome.

The results of this work are consistent with the findings of other studies. Perez-Andujar et al. [14] found that to accurately model the equivalent dose from leakage neutrons requires the consideration of no fewer than four neutron energy regimes. That is supported by this work. The contributions from each of the four neutron energy regimes are similar for this work and the previous model. Furthermore, the dosimetric accuracies were found to be similar.

A major strength of this study is that the improved model relies on far fewer free parameters than previous works. The inclusion of measured data from a second passively-scattered proton therapy beam-line is another strength of this study. Specifically, the analytical model was configured for use at the lower energy (75 MeV) and compared against experimental data to validate its utility to predict stray radiation from an ocular beam-line.

One limitation of this study is that we only benchmarked the model with measured data at a single proton beam energy for the ocular beam-line. Additionally, the measured data was taken in-air and not in a water phantom. These limitations are minor because we demonstrated good agreement for the model compared with Monte Carlo simulated H/D values in a water phantom and at many different energies for the general purpose beam-line.

Future work on leakage radiation from proton therapy should include research and development to translate the analytical models to clinical practice. Specifically, the model should be integrated into treatment planning systems to facilitate routine clinical dose assessments for patients with heterogeneous anatomy and irregular external surfaces. A study from our group has yielded promising preliminary results indicating that the integration of a similar analytical model into a radiotherapy treatment planning system is technically feasible and the leakage-dose algorithm is sufficiently fast for routine clinical treatment planning applications [28]. Specifically, this study found that the time required

was a factor of 1.6 of the time necessary for the proton dose calculation allowing for the total calculation to be completed in less than one hour on a single CPU. Additional research and development work will be needed to enhance the analytical model to account for other treatment factors such as range modulation. Range modulation can be modeled from first principles using the proton modulation function including proton fluence weights, Eqs (2–5) from Polf and Newhauser [9] or Eqs (1–4) from Zheng et al. [29], and dosimetric data at multiple proton beam energies from Monte Carlo simulations. If the relationship between H/D and the modulation width is known from measurements or simulations of the usual case with flat-topped Bragg peaks, the dependence of H/D on modulation width may be accounted for with an empirical analytical model. From previous work, we know that H/D increases with modulation width modestly and continuously (see Figure 9 in Zheng et al. [29]), and it appears to follow a simple analytic expression, *e.g.*, a polynomial or asymptotic exponential function. Studies on range modulation and other treatment factors are underway in our laboratory. This model may also find application for scanned-beam proton therapy beam-lines equipped with passive and dynamic collimators, *e.g.*, milled brass collimators, multi-leaf collimators [30, 31], and trimmers [32].

2.5. Conclusion

In this work, we improved an analytical model of neutron H/D for passively scattered proton therapy in the energy range from 100 to 250 MeV. The improved model relies on fewer configuration parameters and is easier to train. We tested the analytical model on measured neutron H/D values from a separate 75 MeV beam-line. Our results revealed good agreement of the model with both measured data and Monte Carlo simulations. The results of this work suggest that, with further development and testing, analytical models may be applicable for routine use in clinical treatment planning systems to predict neutron exposures to patients.

2.6. References

- ¹R. Miralbell, A. Lomax, L. Cella, and U. Schneider, “Potential reduction of the incidence of radiation-induced second cancers by using proton beams in the treatment of pediatric tumors”, *Int J Radiat Oncol Biol Phys* **54**, 824–9 (2002).
- ²W. D. Newhauser, J. D. Fontenot, A. Mahajan, D. Kornguth, M. Stovall, Y. Zheng, P. J. Taddei, D. Mirkovic, R. Mohan, J. D. Cox, and S. Woo, “The risk of developing a second cancer after receiving craniospinal proton irradiation”, *Phys Med Biol* **54**, 2277–91 (2009).
- ³R. Zhang, R. M. Howell, A. Giebeler, P. J. Taddei, A. Mahajan, and W. D. Newhauser, “Comparison of risk of radiogenic second cancer following photon and proton craniospinal irradiation for a pediatric medulloblastoma patient”, *Phys Med Biol* **58**, 807–23 (2013).
- ⁴S. Agosteo, C. Birattari, M. Caravaggio, M. Silari, and G. Tosi, “Secondary neutron and photon dose in proton therapy”, *Radiother Oncol* **48**, 293–305 (1998).
- ⁵W. D. Newhauser and R. Zhang, “The physics of proton therapy”, *Phys Med Biol* **60**, R155–209 (2015).
- ⁶H. Paganetti, “Nuclear interactions in proton therapy: dose and relative biological effect distributions originating from primary and secondary particles”, *Phys Med Biol* **47**, 747–64 (2002).
- ⁷F. Tommasino and M. Durante, “Proton radiobiology”, *Cancers (Basel)* **7**, 353–81 (2015).
- ⁸W. D. Newhauser and M. Durante, “Assessing the risk of second malignancies after modern radiotherapy”, *Nat Rev Cancer* **11**, 438–48 (2011).
- ⁹J. C. Polf and W. D. Newhauser, “Calculations of neutron dose equivalent exposures from range-modulated proton therapy beams”, *Phys Med Biol* **50**, 3859–73 (2005).
- ¹⁰Y. Zheng, W. Newhauser, J. Fontenot, P. Taddei, and R. Mohan, “Monte carlo study of neutron dose equivalent during passive scattering proton therapy”, *Phys Med Biol* **52**, 4481–96 (2007).
- ¹¹Y. Zheng, W. Newhauser, J. Fontenot, N. Koch, and R. Mohan, “Monte carlo simulations of stray neutron radiation exposures in proton therapy”, *Journal of Nuclear Materials* **361**, 289–297 (2007).
- ¹²R. Zhang, A. Perez-Andujar, J. D. Fontenot, P. J. Taddei, and W. D. Newhauser, “An analytic model of neutron ambient dose equivalent and equivalent dose for proton radiotherapy”, *Phys Med Biol* **55**, 6975–85 (2010).
- ¹³V. Anferov, “Analytic estimates of secondary neutron dose in proton therapy”, *Phys Med Biol* **55**, 7509–22 (2010).

- ¹⁴A. Perez-Andujar, R. Zhang, and W. Newhauser, “Monte carlo and analytical model predictions of leakage neutron exposures from passively scattered proton therapy”, *Med Phys* **40**, 121714 (2013).
- ¹⁵W. Newhauser, J. Fontenot, Y. Zheng, J. Polf, U. Titt, N. Koch, X. Zhang, and R. Mohan, “Monte carlo simulations for configuring and testing an analytical proton dose-calculation algorithm”, *Phys Med Biol* **52**, 4569–84 (2007).
- ¹⁶D. B. Pelowitz, *Mcnpx user’s manual version 2.7.0* (Los Alamos, NM, 2011).
- ¹⁷J. Farah, F. Martinetti, R. Sayah, V. Lacoste, L. Donadille, F. Trompier, C. Nauraye, L. De Marzi, I. Vabre, S. Delacroix, J. Herault, and I. Clairand, “Monte carlo modeling of proton therapy installations: a global experimental method to validate secondary neutron dose calculations”, *Phys Med Biol* **59**, 2747–65 (2014).
- ¹⁸J. D. Fontenot, W. D. Newhauser, and U. Titt, “Design tools for proton therapy nozzles based on the double-scattering foil technique”, *Radiat Prot Dosimetry* **116**, 211–5 (2005).
- ¹⁹J. Herault, N. Iborra, B. Serrano, and P. Chauvel, “Monte carlo simulation of a proton-therapy platform devoted to ocular melanoma”, *Med Phys* **32**, 910–9 (2005).
- ²⁰N. Koch, W. D. Newhauser, U. Titt, D. Gombos, K. Coombes, and G. Starkschall, “Monte carlo calculations and measurements of absorbed dose per monitor unit for the treatment of uveal melanoma with proton therapy”, *Phys Med Biol* **53**, 1581–94 (2008).
- ²¹R. Tayama, Y. Fujita, M. Tadokoro, H. Fujimaki, T. Sakae, and T. Terunuma, “Measurement of neutron dose distribution for a passive scattering nozzle at the Proton Medical Research Center (PMRC)”, *Nuclear Instruments and Methods in Physics Research Section A: Accelerators, Spectrometers, Detectors and Associated Equipment* **564**, 532–536 (2006).
- ²²R. Tayama, H. Handa, K. Hayashi, H. Nakano, N. Sasamoto, H. Nakashima, and F. Masukawa, “Benchmark calculations of neutron yields and dose equivalent from thick iron target for 52–256 mev protons”, *Nuclear Engineering and Design* **213**, 119–131 (2002).
- ²³B. Burgkhardt, A. Fieg G and. Klett, A. Plewnia, and B. Siebrt, “The neutron fluence and h*(10) response of the new lb 6411 rem counter”, *Radiat Prot Dosimetry* **70**, 361–64 (1997).
- ²⁴M. Silari, S. Agosteo, P. Beck, R. Bedogni, E. Cale, M. Caresana, C. Domingo, L. Donadille, N. Dubourg, and A. Exposito, “Intercomparison of radiation protection devices in a high-energy stray neutron field. part iii: instrument response”, *Radiat. Meas.* **44**, 673–91 (2009).
- ²⁵R. H. Olsher, H. H. Hsu, A. Beverding, J. H. Kleck, W. H. Casson, D. G. Vasilik, and R. T. Devine, “Wendi: an improved neutron rem meter”, *Health Phys* **79**, 170–81 (2000).

- ²⁶L. S. Lasdon, R. L. Fox, and M. W. Ratner, *Nonlinear optimization using the generalized reduced gradient method*, Report (National Technical Information Service, 1973).
- ²⁷J. Farah, A. Bonfrate, L. De Marzi, A. De Oliveira, S. Delacroix, F. Martinetti, F. Trompier, and I. Clairand, “Configuration and validation of an analytical model predicting secondary neutron radiation in proton therapy using monte carlo simulations and experimental measurements”, *Phys Med* (2015) 10.1016/j.ejmp.2015.01.017.
- ²⁸J. Eley, W. Newhauser, K. Homann, R. Howell, C. Schneider, M. Durante, and C. Bert, “Implementation of an analytical model for leakage neutron equivalent dose in a proton radiotherapy planning system”, *Cancers* **7**, 427–438 (2015).
- ²⁹Y. Zheng, J. Fontenot, P. Taddei, D. Mirkovic, and W. Newhauser, “Monte carlo simulations of neutron spectral fluence, radiation weighting factor and ambient dose equivalent for a passively scattered proton therapy unit”, *Phys Med Biol* **53**, 187–201 (2008).
- ³⁰M. Bues, W. D. Newhauser, U. Titt, and A. R. Smith, “Therapeutic step and shoot proton beam spot-scanning with a multi-leaf collimator: a monte carlo study”, *Radiat Prot Dosimetry* **115**, 164–9 (2005).
- ³¹W. D. Newhauser, R. Zhang, T. G. Jones, A. Giebeler, P. J. Taddei, R. D. Stewart, A. Lee, and O. Vassiliev, “Reducing the cost of proton radiation therapy: the feasibility of a streamlined treatment technique for prostate cancer”, *Cancers (Basel)* **7**, 688–705 (2015).
- ³²D. E. Hyer, P. M. Hill, D. Wang, B. R. Smith, and R. T. Flynn, “A dynamic collimation system for penumbra reduction in spot-scanning proton therapy: proof of concept”, *Med Phys* **41**, 091701 (2014).

Chapter 3.

A Descriptive and Broadly Applicable Model of Therapeutic and Stray Absorbed Dose from 6 MV to 25 MV Photon Beams

3.1. Introduction

The goal of modern external beam radiotherapy is to deliver a highly targeted radiation dose to a diseased anatomic location or region while sparing the the rest of the body. However, in practice, the whole body is unavoidably exposed to unwanted stray radiation. Healthy tissue in the margin of the treatment field will receive absorbed doses on the order of the prescribed dose. Tissues outside the treatment field receive stray dose from scattered and leakage radiation that is one to four orders of magnitude smaller [1]. Historically, clinical practices focused almost exclusively on in-field exposures because of their prime importance to curing primary cancers. In recent years, 5-year survival rates have surpassed 69% for all cancers [2] and 80% for childhood cancers [3], but a myriad of radiation epidemiology studies have revealed the high prevalence of radiation-induced late effects including cardiac toxicity and radiogenic second cancers[4, 5]. Most radiogenic second cancers occur outside the therapeutic radiation field [6–10]. For these reasons, there is increasing interest in knowing the small stray radiation exposures to the whole body.

Many researchers have reported algorithms to model absorbed dose from external beam photon radiation therapy [11–14]. In general, these algorithms accurately predict exposures inside and immediately outside the high-dose treatment field. However, none of these algorithms have fully addressed the stray dose far from the treatment field. Stovall et al. described three main sources of stray radiation from external beam radiation therapy delivered with electron linear accelerators [15]. Radiation scattered from the treatment head, known as head scatter, is primarily important within about 10 cm from the field edge. Patient scatter is an important source up to around 30 cm from the field edge.

Adapted with permission from: Schneider, C.W.; Newhauser, W.D.; Wilson, L.J.; Schneider, U.; Kaderka, R.; Miljanić, S.; Knežević, Ž.; Stolarczyk, L.; Durante, M.; Harrison, R.M., A descriptive and broadly applicable model of therapeutic and stray absorbed dose from 6 MV to 25 MV photon beams. *Med Phys.* **2017**, *44*, 3805–3814. Copyright (2017) American Association of Physicists in Medicine.

Finally, leakage radiation emanates from the treatment enclosure and predominates the stray radiation dose beyond about 30 cm. Monte Carlo simulations have been a useful research tool for modeling stray dose [16–18], but these methods have not found use in clinical settings due to their complexity and long computational times. The feasibility of analytical models to predict stray dose from radiation therapy has been supported by several works [7, 19–25], but few attempts have been made at developing models accurate for both in-field and out-of-field doses. Jagetic and Newhauser reported on one such model that accurately predicts absorbed dose from therapeutic, scatter, and leakage radiation [26]. This model was evaluated only at 6 MV photon-beam energy, only for Conformal Radiation Therapy (CRT), and only for one type of electron linear accelerator (Elekta, SL25, Stockholm). The study left open important questions. Firstly, is this approach extensible to other treatment techniques, e.g., Intensity Modulated Radiation Therapy (IMRT)? Secondly, is it adaptable to treatment units from other manufacturers? Third, can it be done without proprietary data?

The objective of this study was to determine whether a physics-based analytical modeling approach is applicable to a variety of treatment techniques and treatment units. More specifically, we characterized the dosimetric accuracy that can be achieved without the use of proprietary and machine-specific parameters to configure the model. In order to accomplish this, we developed a new analytical model that can be configured with measured dose profiles that are similar to those used for configuring commercial treatment planning systems. The model was tested using measured data from a variety of treatment machines and techniques in the 6 to 25 MV interval of photon beam energy.

3.2. Methods and Materials

3.2.1. Analytical Model

The analytical model consists of four terms: one to model the therapeutic radiation dose and three to model sources of stray dose, or

$$D_T = D_P + D_{HS} + D_{PS} + D_L \quad , \quad (3.1)$$

where D_T is the total dose from all sources, D_P is the primary dose term that models the therapeutic dose, D_{HS} is the first stray dose term that models dose from head scattered radiation, D_{PS} is the second stray dose term that models dose from patient scattered radiation, and D_L is the third stray dose term that models leakage radiation.

Consequently, simplicity and ease of use were of prime importance to the model's design. In particular, we designed it for ease and simplicity of configuration, e.g., by using non-proprietary data that can be quickly measured in most clinics. The model proposed in this work shares the major underlying physics and mathematical form as that of Jagetic and Newhauser, but it was radically simplified here to streamline the configuration process and to eliminate the use of proprietary data. As will become readily apparent later, these two features were of prime importance in configuring the model for multiple treatment techniques and machines. Table 3.1 compares the two models and detailed descriptions of the terms from this work follow below.

The primary absorbed dose, D_P , for square and rectangular fields is given by

$$D_P = A_P \times C(x, z) \times C(y, z) \times TF_{P,w}(x, y, z, E) \quad (3.2)$$

Table 3.1. Comparison of model terms for Jagetic and Newhauser [26] and this work.

Term	Jagetic and Newhauser [26]		This Work	
	Description	Eqn.	Description	Eqn.
Uncollimated Fluence, Φ	Modeled using electron radiation yield, 3 Gaussian source terms, and divergence.	(2.8)	Not modeled.	N/A
In-air Primary Collimated Fluence, Φ_P	Uncollimated fluence multiplied by cumulative normal.	(2.10)	Implicitly modeled.	(3.2)
Primary Dose in Water, $D_{P,w}$	In-air primary fluence multiplied by transmission factor and mass-energy absorption coefficient.	(2.15)	Cumulative normal multiplied by transmission factor and primary scaling factor.	(3.2)
Leakage Fluence, Φ_L	Uncollimated fluence multiplied by complimentary cumulative normal.	(2.17)	Implicitly modeled.	(3.18)
Leakage Dose in Water, $D_{L,w}$	Leakage fluence multiplied by transmission factors for collimators and water and mass-energy absorption coefficient.	(2.20)	Cumulative normal multiplied by Gaussian source term, water transmission factors, and energy dependent leakage scaling factor.	(3.18)
Head-Scatter Dose in Water, $D_{HS,w}$	Gaussian multiplied by empirical, field-size dependent, scaling factor and water transmission factor.	(2.27)	Gaussian multiplied by energy-dependent scaling factor and water transmission factor.	(3.11)
Patient-Scatter Dose in Water, $D_{PS,w}$	Dual Gaussians multiplied by empirical, field-size dependent scaling factors and water transmission factor.	(2.28)	Gaussian multiplied by energy-dependent scaling factor and water transmission factor.	(3.14)

where A_P governs the amplitude of the primary dose on the central axis, $C(x, z)$ and $C(y, z)$ govern the width and lateral penumbræ of the beam in the x and y directions, x and y are the lateral distances from central-axis in the plane of calculation for the in- and cross-plane directions, and $TF_{P,w}(x, y, z, E)$ is the transmission factor of the primary portion of the beam of nominal energy E at a point (x, y, z) in a phantom.

The C functions in (3.2) model the shape of the primary dose via the simple but realistic approach of using cumulative normal distributions, as in

$$C(x, z) = \frac{1}{2\pi\sigma^2(z)} \times \left\{ \int_{-\infty}^x \exp \left[\frac{-(x' + \bar{x}(z))^2}{2(\sigma_P^2(z))} \right] dx' \right\} \times \left\{ 1 - \int_{-\infty}^x \exp \left[\frac{-(x' - \bar{x}(z))^2}{2(\sigma_P^2(z))} \right] dx' \right\} . \quad (3.3)$$

where $\sigma_P(z)$ is the width parameter for the cumulative normal functions used to define the penumbra, and $\bar{x}_P(z)$ and $\bar{y}_P(z)$ are the centroids of the cumulative normals projected to depth z . These parameters are described in detail below.

The parameters $\sigma_P(z)$, $\bar{x}(z)$, and $\bar{y}(z)$ are scaled with depth according to

$$\sigma_P(z) = \sigma_{P,0} \times F_P(z) \quad , \quad (3.4)$$

$$\bar{x}(z) = \bar{x}_{P,0} \times F_P(z) \quad , \quad (3.5)$$

$$\bar{y}(z) = \bar{y}_{P,0} \times F_P(z) \quad , \quad (3.6)$$

where $\sigma_{P,0}$ is the width parameter in the isocentric plane, $\bar{x}_{P,0}$ and $\bar{y}_{P,0}$ are the lateral field edge locations in the isocentric plane. $F_P(z)$ is the scaling factor defined as

$$F_P(z) = \frac{\text{SSD} + d_{\text{iso}} + (z - d_{\text{iso}}) \times \alpha_P}{\text{SSD} + d_{\text{iso}}} \quad , \quad (3.7)$$

where SSD is the source-to-surface distance, d_{iso} is the depth at isocenter, and α_P is an empirical correction factor to the rate at which $\sigma_P(z)$, $\bar{x}_P(z)$, and $\bar{y}_P(z)$ change with depth.

The transmission factor in water at the calculation point is given by

$$TF_{P,w}(x, y, z, E) = \exp[-\mu_{P,\text{eff}} \times d(x, y, z)] \quad , \quad (3.8)$$

where the path length through water to point (x, y, z) is

$$d(x, y, z) = \sqrt{(\text{SSD} + z)^2 + x^2 + y^2} \times \left(\frac{z}{\text{SSD} + z} \right) \quad . \quad (3.9)$$

The effective linear photon attenuation coefficient is

$$\mu_{P,\text{eff}}(E) = (m_{\mu,P} \times E + b_{\mu,P}) \times \mu|_{w,\bar{E}} \quad , \quad (3.10)$$

where $\mu_{P,\text{eff}}(E)$ is the effective linear attenuation coefficient in water for the primary portion of a beam of nominal energy E , and $\mu|_{w,\bar{E}}$ is the linear attenuation coefficient in water for photons of energy \bar{E} , where \bar{E} is the average energy of the photon beam approximated as one third the value of the nominal energy following Jagetic and Newhauser [26]. The parameters $b_{\mu,P}$ and $m_{\mu,P}$ are the 0th and 1st order coefficients, respectively, of an empirical correction factor to the effective linear attenuation coefficient that is parameterized with energy. This factor is needed because $\mu|_{w,\bar{E}}$ will not equal the true energy weighted mean of the linear attenuation coefficient, $\mu(E)$, across the full energy spectrum of the beam. The values of the parameters $b_{\mu,P}$ and $m_{\mu,P}$ are determined along with the other fitting parameters via the model training procedure described in Section 3.2.3. The values of $\mu|_{w,\bar{E}}$ for the energies considered in this study were found from the National Institute of Standards and Technology (NIST) XCOM photon cross sections database [27].

The stray dose is the sum of three terms. The head scatter dose term is the narrowest laterally and is given by

$$D_{\text{HS}}(x, y, z, E) = \frac{A_{\text{HS}}(E)}{\sigma_{\text{HS}}(z)\sqrt{2\pi}} \exp\left[\frac{-(x^2 + y^2)}{2\sigma_{\text{HS}}^2(z)}\right] \times TF_{\text{HS,w}}(x, y, z, E) \quad , \quad (3.11)$$

where $A_{\text{HS}}(E)$ is the energy dependent scaling factor given by

$$A_{\text{HS}}(E) = \beta_{\text{HS}} \times E + \gamma_{\text{HS}} \quad , \quad (3.12)$$

β_{HS} and γ_{HS} are the 1st and 0th order coefficients, respectively, that parameterize the factor with photon beam energy. The depth dependent width parameter, $\sigma_{\text{HS}}(z)$, is given by

$$\sigma_{\text{HS}}(z) = \sigma_{\text{HS},0} \times F_{\text{HS}}(z) \quad , \quad (3.13)$$

where $\sigma_{\text{HS},0}$, is the head scatter width parameter in the isocentric plane, $F_{\text{HS}}(z)$ is defined similarly to (3.7) with empirical adjustment factor α_{HS} , and $TF_{\text{HS,w}}(x, y, z, E)$ is the transmission factor for head scattered radiation defined similarly to (3.8).

The patient scatter dose term is similarly given by

$$D_{\text{PS}}(x, y, z, E) = \frac{A_{\text{PS}}(E)}{\sigma_{\text{PS}}(z)\sqrt{2\pi}} \exp\left[\frac{-(x^2 + y^2)}{2\sigma_{\text{PS}}^2(z)}\right] \times TF_{\text{PS,w}}(x, y, E) \quad , \quad (3.14)$$

where $A_{\text{PS}}(E)$ is the energy dependent scaling factor

$$A_{\text{PS}}(E) = \beta_{\text{PS}} \times E + \gamma_{\text{PS}} \quad , \quad (3.15)$$

β_{PS} and γ_{PS} are the 1st and 0th order coefficients, respectively, that parameterize the scaling factor with photon beam energy, and $\sigma_{\text{PS}}(z)$ is a depth dependent width parameter that scales with depth according to

$$\sigma_{\text{PS}}(z) = \sigma_{\text{PS},0} \times F_{\text{HS}}(z) \quad , \quad (3.16)$$

where $\sigma_{\text{PS},0}$ is the head scatter width parameter in the isocentric plane and $F_{\text{PS}}(z)$ is defined similarly to (3.7) with empirical adjustment factor α_{PS} . The transmission factor for radiation from patient scatter in a water phantom is given by

$$TF_{\text{PS,w}}(x, y, E) = \exp \left(-\mu_{\text{PS,eff}}(E) \times \sqrt{x^2 + y^2} \right) . \quad (3.17)$$

The functional form of the leakage dose term is illustrated in Figure 3.1 and is defined as

$$\begin{aligned} D_{\text{L}}(x, y, z, E) &= \frac{A_{\text{L}}(E)}{\sigma_{\text{L}}(z)\sqrt{2\pi}} \exp \left[\frac{-(x^2 + y^2)}{2\sigma_{\text{L}}^2(z)} \right] \\ &\times TF_{\text{L,w}}(x, y, z, E) \times PC(r, z, E) \\ &\times [1 - C(x, z) \times C(y, z)] \quad , \end{aligned} \quad (3.18)$$

where $A_{\text{L}}(E)$ is an energy dependent scaling factor

$$A_{\text{L}}(E) = (\beta_{\text{L}} \times E + \gamma_{\text{L}}) F_{\phi} \quad , \quad (3.19)$$

and F_{ϕ} accounts for increased leakage present in treatments with large amount of photon fluence modulation. The depth-dependent width parameter from (3.18) is

$$\sigma_{\text{L}}(z) = \sigma_{\text{L},0} \times F_{\text{L}}(z) \quad , \quad (3.20)$$

where $F_L(z)$ is defined similarly to (3.7) with a corresponding empirical adjustment factor α_L . The factor $[1 - C(x, z) \times C(y, z)]$ suppresses the leakage term inside the treatment field, and $PC(r, z, E)$ models attenuation in the primary collimator. This primary collimator function is given by

$$PC(r, z, E) = 1 - A_{PC}(E) \times \int_{-\infty}^r \exp \left[\frac{-(r' + \bar{r}(z))^2}{2\sigma_{PC}^2} \right] dr' , \quad (3.21)$$

where $r = \sqrt{x^2 + y^2}$, $A_{PC}(E)$ is the energy dependent scaling factor

$$A_{PC}(E) = \beta_{PC} \times E + \gamma_{PC} , \quad (3.22)$$

$\sigma_{PC}(z)$ is the width parameter of primary collimator penumbra given by

$$\sigma_{PC}(z) = \sigma_{PC,0} \times F_L(z) , \quad (3.23)$$

and $\bar{r}(z)$ is the lateral location of the primary collimator projected to depth z as in

$$\bar{r}(z) = \bar{r}_0 \times F_L(z) . \quad (3.24)$$

3.2.2. Measurements

There are three distinct sets of measured dosimetric data considered in this manuscript summarized in Table 3.2. The first set was obtained in this study under the auspices of the European Radiation Dosimetry (EURADOS) Working Group 9 (WG9), a multinational collaboration of institutions and researchers dedicated to research and development in the field of radiation dosimetry in medicine [1]. These experiments were specifically designed to yield dosimetric data that was needed to understand and model the physics of stray radiation exposure. The measurement methods and a limited number of preliminary results were

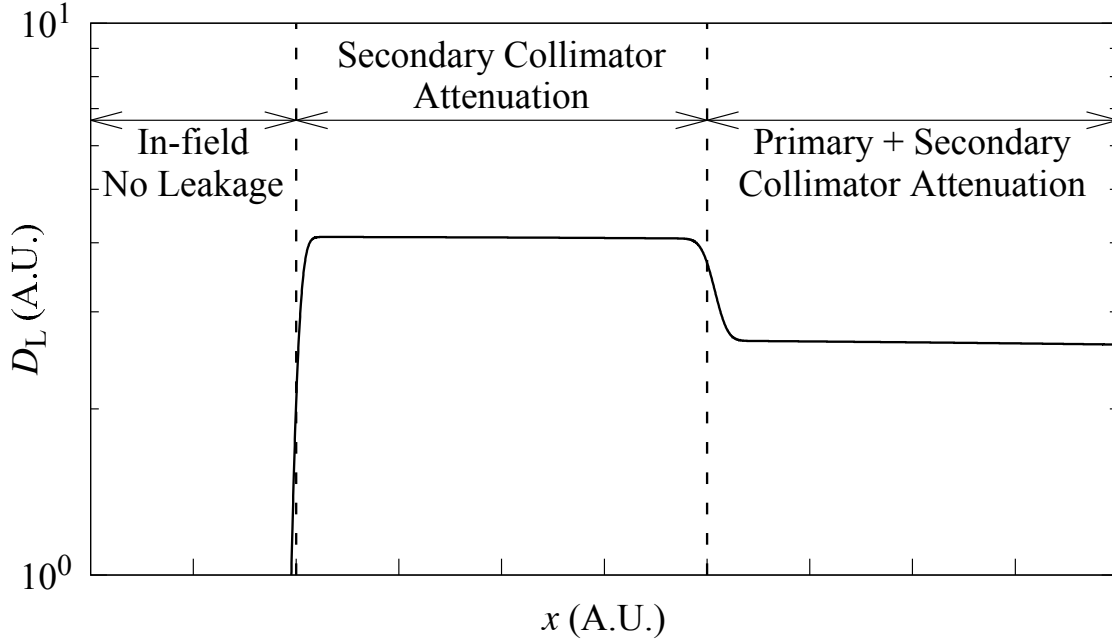


Figure 3.1. Functional form of the leakage dose, D_L , versus off-axis distance, x . In the in-field region, the leakage dose is defined to be zero. In the intermediate region, leakage is attenuated by the secondary collimator. Far out of field, there is additional attenuation from the primary collimator.

previously reported by Bordy et al. [28] The EURADOS data set consists of measurements made with multiple types thermoluminescent dosimeters (TLDs), radiophotoluminescent dosimeters (RPLs), and optically stimulated luminescent dosimeters (OSLDs) of doses delivered by a Saturne 43 linac (GE Medical Systems, USA). The calibration procedure for the various types of dosimeters is described by Knežević et al. [29]. Doses were measured at various locations inside a $30 \times 30 \times 60 \text{ cm}^3$ water phantom. This data set includes dose profiles at 10, 15, 20, and 25 cm depths in water with a source-to-surface distance (SSD) of 90 cm, a field size of $10 \times 10 \text{ cm}^2$, and beam energies of 6, 12, and 20 MV. The irradiations each delivered a reference dose of 2 Gy to the isocenter located at 10 cm depth. The measurements from this data set are being prepared for distribution in the form of electronic files containing complete tables of all numerical data and will be available for download from the EURADOS website (<http://www.eurados.org>).

Table 3.2. Manufacturers, machines, techniques, nominal photon energies, and measurement phantoms considered in this study. All measurements in the EURADOS and KGU data sets were taken in water box phantoms. All measurements in the Halg et al. data set were taken in an anthropomorphic phantom.

Data Set	MFR.	Model	Technique	Beam Energy (MV)
EURADOS	GE	Saturne 43	CRT	6,12, 20
KGU	Elekta	SL25	CRT	6, 18, 25
	Varian	Clinac 21 iX	CRT, IMRT	6
(Halg et al.)	Elekta	Synergy	IMRT	6
	Siemens	Oncor Avant-Garde	IMRT	6
		Mevatron Primus	Wedge	
	Accuray	CyberKnife	Stereotactic	6
TomoTherapyHi-Art 2		IMRT		

The second data set used in this work comprises measurements performed at the Klinikum Goethe Universität (KGU) in Frankfurt, Germany. The KGU data set measurements were made with a diamond detector model (60003 PTW, Freiburg) of doses delivered by an SL25 linac (Elekta, Stockholm) for various field sizes, depths, and beam energies. For this work, we consider 10 x 10 cm² fields at depths of 1.5 and 3.5 cm in water and 100 cm SSD for beam energies of 6, 18, and 25 MV. These measurements were previously published in Kaderka et al. [30].

The third data set used in this work comprises doses measured in an anthropomorphic phantom (Alderson-Rando, RSD Radiology Support Devices, Long Beach, CA) for a variety of widely used treatment machines and treatment techniques. These measurements were previously published in Halg et al. [31]. Prostate treatment plans were created for nine treatment techniques from four manufacturers, including Accuray (Sunnyvale, CA, USA), Elekta (Stockholm, Sweden), Varian Medical Systems (Palo Alto, CA, USA), and Siemens (Berlin, Germany). All beams in this data set had a nominal energy of 6 MV. The dose measurements were performed using TLDs placed inside the anthropomorphic phantom. The dose along the medial patient axis was determined using 34 TLDs spaced at 2.5 cm intervals from the target (in prostate) to the head.

3.2.3. Model Training

In this work, the analytical model was trained separately using the EURADOS and KGU data sets. Training was accomplished by simultaneously fitting the parameters listed in Table 3.5 to measured dose values at all locations and at all beam energies. We used a gradient search algorithm to vary the free parameters and minimize the sum of the local relative differences, ΔD_{Total} , between the predicted and measured values. The sum of total relative differences was defined according to

$$\Delta D_{\text{Total}} = \sum_{i=1}^n \Delta D_i = \sum_{i=1}^n \left[\frac{|D_i^{\text{model}} - D_i^{\text{measured}}|}{(D_i^{\text{model}} + D_i^{\text{measured}}) / 2} \right] , \quad (3.25)$$

where n is the number of data points. In order to characterize the goodness of fit, we calculated

$$\overline{\Delta D} = \Delta D_{\text{Total}} / n , \quad (3.26)$$

where $\overline{\Delta D}$ is the average local relative difference, and

$$\Delta D_{\text{max}} = \max(\{\Delta D_1, \dots, \Delta D_n\}) , \quad (3.27)$$

where ΔD_{max} is the maximum of the local relative differences.

3.2.4. Model Validation

The model, as configured and trained on both the KGU and EURADOS data sets, was validated by comparison with independent data, namely, the measured dose profiles in an anthropomorphic phantom for several treatment machines and techniques. Variations in depth due to the irregular surface contour of the phantom were modeled implicitly since it has been demonstrated that these variations are modest [24]. We compared the model as trained on two independent training data sets in order to test the sensitivity of the agreement to the choice of training data.

The quality assurance technique known as gamma analysis, first described by Low et al. [32], characterizes the agreement between measured and calculated dose distributions on a point by point basis by combining dose difference and distance to agreement criteria. In most radiotherapy clinics, the dose difference criterion is selected at 3% of the maximum dose, and the distance to agreement criterion at 3 mm. These values are commonly known as the Van Dyk criteria [33]. However, this choice is not suitable for application far outside of the treatment field since dose in this region is well under 3% of the maximum dose, rendering the test insensitive to important dose errors in the out-of-field region. To overcome this limitation, we extended the gamma index analysis method that is extended in order to provide sufficient sensitivity and dynamic range to characterize dosimetric agreement in both the in-field and out-of-field regions.

The gamma indices at all positions in therapeutic and out-of-field dose regions were calculated according to

$$\Gamma(x_m, x_c) = \begin{cases} \sqrt{\frac{r^2(x_m, x_c)}{\Delta d_T^2} + \frac{\delta_R^2(x_m, x_c)}{\Delta D_R^2}}, & x_m \text{ in/near field} \\ \sqrt{\frac{r^2(x_m, x_c)}{\Delta d_{\text{OOF}}^2} + \frac{\delta_A^2(x_m, x_c)}{\Delta D_A^2}}, & x_m \text{ out-of-field} \end{cases} \quad (3.28)$$

where x_m and x_c are the locations of measured and calculated dose values, respectively. $r(x_m, x_c)$ is the difference in position between measured and calculated dose values, Δd_T and Δd_{OOF} are the distance to agreement criteria in the therapeutic and out-of-field regions, respectively, $\delta_R(x_m, x_c)$ represents the relative dose difference between measured and calculated dose values, ΔD_R is the relative dose difference criterion, $\delta_A(x_m, x_c)$ represents the absolute dose difference between measured and calculated dose values, and ΔD_A is the absolute dose difference criterion. The therapeutic dose region was delineated from the out-of-field dose region at the 1% relative dose level based on previously published findings [26, 34–36]. This allows for a significantly more severe dosimetric test out-of-field than conventional methods. Gamma index analysis was performed separately comparing the analytical model calculations on each of the two training data sets to the anthropomorphic

phantom data set for the Varian Clinac 21 iX CRT. Gamma index pass rates were selected at 100%, 95%, 90%, and 67%. The corresponding gamma index criteria were iteratively decreased until the analysis yielded the selected pass rate.

3.3. Results

3.3.1. Model Training

Figure 3.2 shows the Elekta SL25 measured and analytical model calculated total absorbed dose values for the three nominal beam energies (6, 18, and 25 MV) from the KGU data set. This figure demonstrates excellent agreement between measurement and analytical model calculations across the range of nominal beam energies considered. Figure 3.3 shows the measured absorbed dose from the 6 MV beam at a depth 1.5 cm in water plotted with the analytical model calculated absorbed dose. The individual analytical model dose terms (*i.e.* D_P , D_{HS} , D_{PS} , D_L) are also plotted thus demonstrating how the combination of these terms yields excellent agreement in both the in- and out-of-field regions. Table 3.3 shows the average and local relative differences for the model compared with the KGU dataset including the 6 MV beam at a depth of 1.5 cm and the 18 and 25 MV beams each at a depth of 3.5 cm. The average local relative difference, defined in (3.26), was 9.9%. The maximum local relative difference, defined in (3.27), was 33%.

Table 3.3. Average and maximum local relative differences for all nominal photon beam energies E for the model calculations compared with the Klinikum Goethe Universität (KGU) data set.

E	$\overline{\Delta D}(\%)$	$\Delta D_{\max}(\%)$
6 MV	7.1	23.9
18 MV	12.3	32.9
25 MV	8.1	33.0
All Energies	9.9	33.0

Figure 3.4 shows plots of Saturne 43 measured and analytical model calculated absorbed dose for the 6, 12, and 20 MV nominal beam energies at depths in water of 10 and 25 cm from the model as trained with the EURADOS data set. Very good agreement is seen between the model and the training data, showcasing the ability of the model to

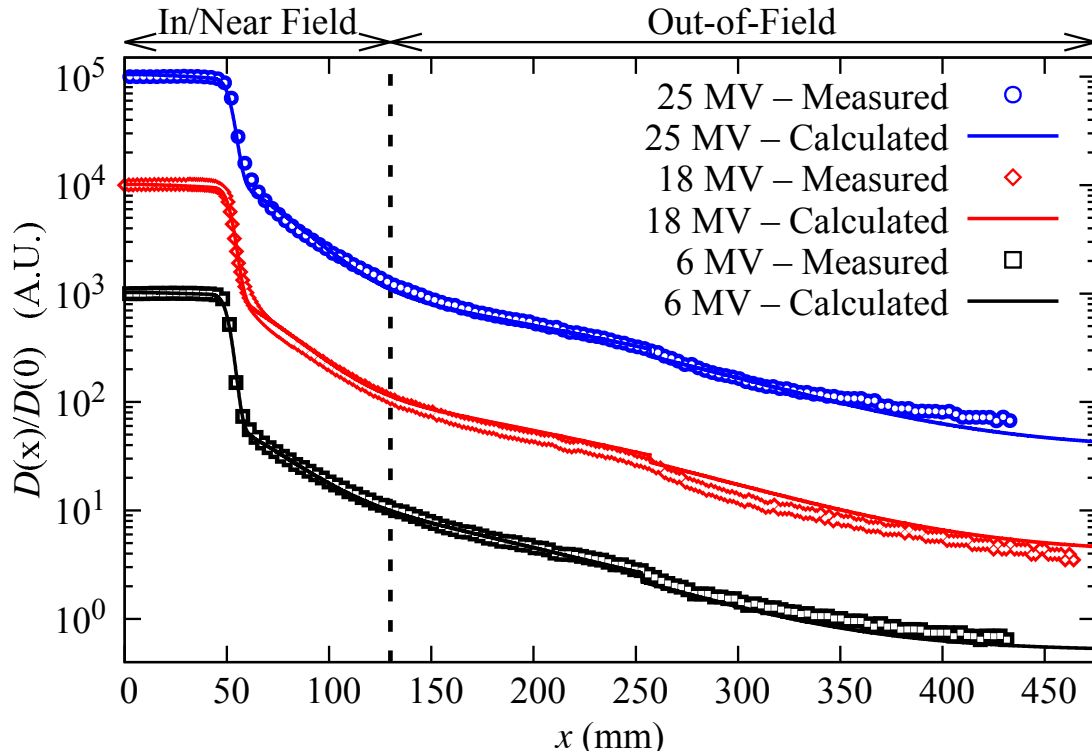


Figure 3.2. Measured and calculated relative absorbed dose $D(x)/D(0)$ versus off-axis position x for all beam energies from the Klinikum Goethe Universität (KGU) data set. The abscissa corresponds to the lateral distance from the central axis of the beam. The ordinate represents the relative absorbed dose as a function of x . All profiles are at d_{\max} (1.5 cm for 6 MV and 3.5 cm for 18 and 25 MV) and were normalized to the value of dose at $x = 0$. For visual clarity, the profiles are offset by factors of 10.

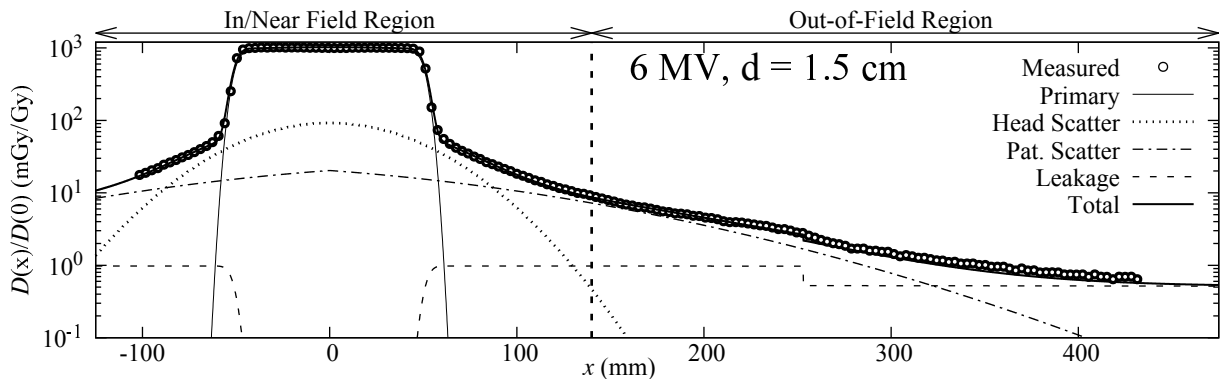


Figure 3.3. Measured and calculated relative absorbed dose $D(x)/D(0)$ versus off-axis position x from the 6 MV beam at 1.5 cm depth in water from the Klinikum Goethe Universität (KGU) data set.

accurately calculate absorbed dose across a range of energies and depths. Figure 3.5 show the measured absorbed dose from the 6 MV beam at a depth 10 cm in water plotted with the analytical model calculated absorbed dose and all individual dose components. Table 3.4 lists the average and maximum local relative differences for all energies and depths included in this data set. The average difference for all locations and energies considered was 9.9% and the maximum difference was 41%.

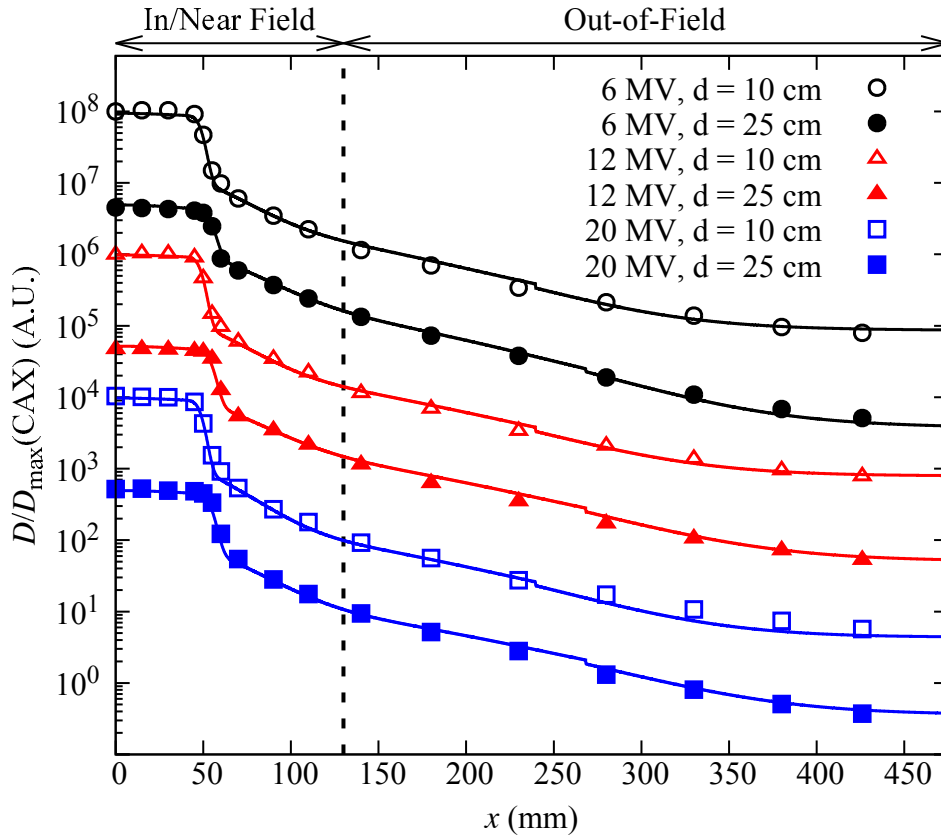


Figure 3.4. Measured and calculated relative absorbed dose $D(x)/D_{\text{iso}}$ versus off-axis position x for 6, 12, and 20 MV beams at 10 cm and 25 cm depths in water from the European Radiation Dosimetry Group (EURADOS) data set. The abscissa corresponds to distance from the central axis of the beam. The ordinate corresponds to the relative absorbed dose as a function of x . The profiles were normalized to the value of dose at isocenter for the given beam energy. For visual clarity, the profiles were offset from one another by factors of 10.

The model parameter values resulting from fitting the model to the KGU and EURADOS data sets of measurements in water are listed in Table 3.5. The relative differences between the parameters as fit on these data sets are also listed. The primary

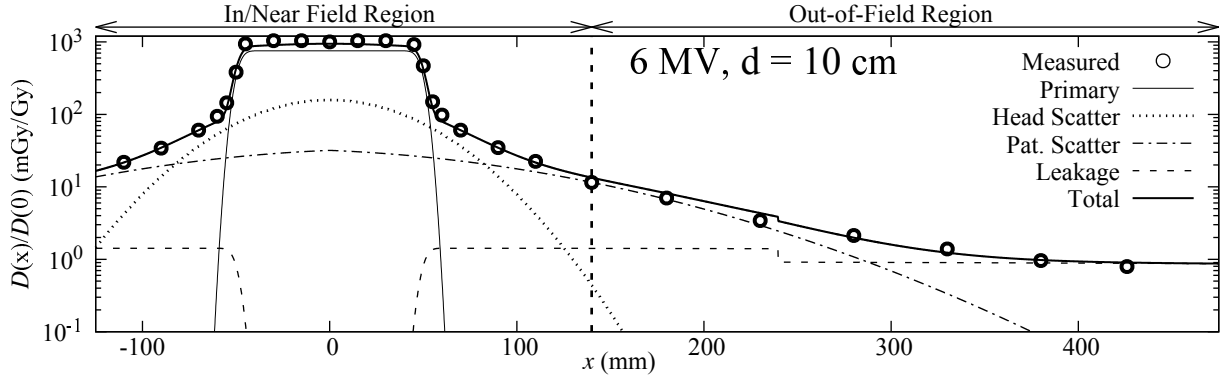


Figure 3.5. Measured and calculated relative absorbed dose $D(x)/D(0)$ versus off-axis position x for the 6 MV beam at 10 cm depth in water from the European Radiation Dosimetry Group (EURADOS) data set.

Table 3.4. Average and maximum local relative differences for all nominal photon beam energies and depths for the model calculations compared with the European Radiation Dosimetry Group (EURADOS) data set.

Depth (cm)	6 MV		12 MV	
	$\Delta D(\%)$	$\Delta D_{\max}(\%)$	$\Delta D(\%)$	$\Delta D_{\max}(\%)$
10	10.2	26.9	10.3	25.2
15	11.8	31.2	9.5	27.9
20	9.8	41	7.4	20.3
25	8.6	30.3	8.8	26.5
All	10.1	41	9	27.9
Depth (cm)	20 MV		All Energies	
	$\Delta D(\%)$	$\Delta D_{\max}(\%)$	$\Delta D(\%)$	$\Delta D_{\max}(\%)$
10	11.8	30.7	10.8	30.7
15	10.6	34.6	10.6	34.6
20	9.1	31.7	8.7	41
25	10.8	27.4	9.4	30.3
All	10.6	34.6	9.9	41

dose parameters resulting from fitting the model to each of the two data sets are similar with no parameter differing by more than 33.5%. However, there are considerable differences between the parameters for the out-of-field dose components, thus highlighting the ability of the model to adapt to out-of-field dose profiles of different machines.

Table 3.5. Model parameters for model as trained on Klinikum Goethe Universität (KGU) and European Radiation Dosimetry Group (EURADOS) data sets and the relative differences between the results for each.

Term	Description	Symbol	KGU	EURADOS	Rel. Diff.
Primary	Dose coefficient	A_P (mGy/Gy)	982	1326	29.9%
	Field edge	$\bar{x}_{P,0}$ (cm)	5.0	4.9	1.4%
	Penumbra	$\sigma_{P,0}$ (cm)	0.33	0.33	1.6%
	Projection correction factor	α_P (—)	1.1	0.78	33.5%
	Attenuation 0 th order coefficient	$b_{\mu,P}$ (—)	1.0	1.1	12.1%
	Attneuation 1 st order coefficient	$m_{\mu,P}$ (MeV ⁻¹)	5.2×10^{-2}	5.7×10^{-2}	8.5%
Head Scatter	Dose 0 th order coefficient	β_{HS} (mGy/Gy)	9927	16195	48.0%
	Dose 1 st order coefficient	γ_{HS} (mGy/Gy/MeV)	722	263	93.3%
	Width parameter	$\alpha_{HS,0}$ (cm)	4.2	4.1	4.0%
	Projection correction factor	α_{HS} (—)	0.88	0.79	10.8%
	Attenuation 0 th order coefficient	$b_{\mu,HS}$ (—)	3.0×10^{-3}	8.3×10^{-3}	94.9%
	Attneuation 1 st order coefficient	$m_{\mu,HS}$ (MeV ⁻¹)	3.5×10^{-2}	5.0×10^{-2}	35.6%
Patient Scatter	Dose 0 th order coefficient	β_{PS} (mGy/Gy)	7717	9616	21.9%
	Dose 1 st order coefficient	γ_{PS} (mGy/Gy/MeV)	-145	-342	80.9%
	Width parameter	$\alpha_{PS,0}$ (cm)	15.0	12.0	21.9%
	Projection correction factor	α_{PS} (—)	0.60	0.58	3.6%
	Attenuation 0 th order coefficient	$b_{\mu,PS}$ (—)	0.88	0.49	56.4%
	Attneuation 1 st order coefficient	$m_{\mu,PS}$ (MeV ⁻¹)	-1.8×10^{-2}	-1.5×10^{-2}	13.7%
Leakage	Dose 0 th order coefficient	β_L (mGy/Gy)	9601	13287	32.2%
	Dose 1 st order coefficient	γ_L (mGy/Gy/MeV)	-100	-613	143.9%
	Width parameter	$\alpha_{L,0}$ (cm)	340	239	34.8%
	Projection correction factor	α_L (—)	0.80	0.80	0.7%
	Attenuation 0 th order coefficient	$b_{\mu,L}$ (—)	1.7	0.90	63.9%
	Attneuation 1 st order coefficient	$m_{\mu,L}$ (MeV ⁻¹)	-4.7×10^{-2}	-5.0×10^{-2}	6.6%
	PC 0 th order coefficient	β_{PC} (—)	0.46	0.35	28.3%
	PC 1 st order coefficient	γ_{PC} (MeV ⁻¹)	4.0×10^{-3}	3.5×10^{-3}	11.4%
	PC location	\bar{x}_{PC} (cm)	25.0	24.0	4.3%
PC penumbra	$\sigma_{PC,0}$ (cm)	5.0×10^{-3}	5.0×10^{-3}	0.0%	

3.3.2. Validation with anthropomorphic phantom measurements

Doses measured in an anthropomorphic phantom for all nine treatment machines considered are shown in Figure 3.6. Also shown on this plot are the calculated doses from the analytical model as trained on both the KGU and EURADOS data sets from the previous section. The gamma index criteria required to achieve the selected passing rates are listed in Table 3.6.

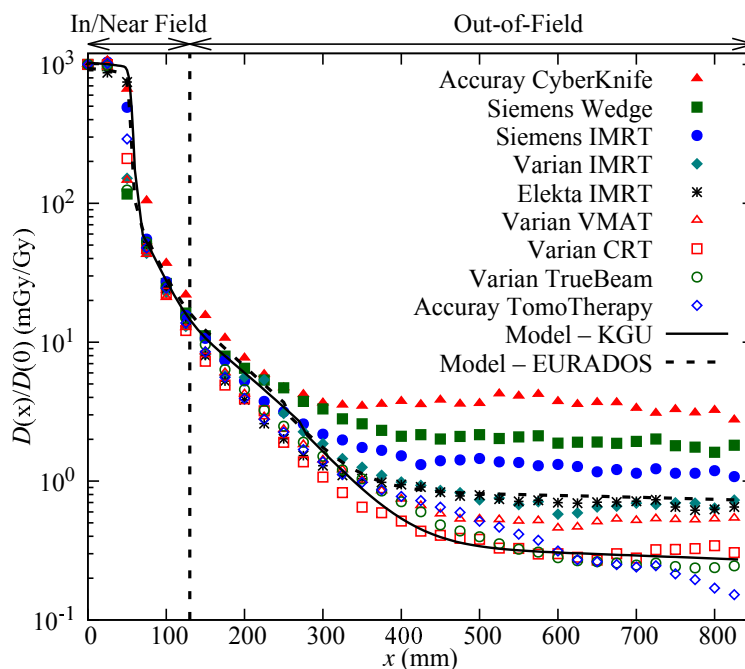


Figure 3.6. Relative absorbed dose $D(x)/D(0)$ versus off-axis position x in anthropomorphic phantom from irradiations by various treatment techniques and machines. Points represent measured doses. Lines represent analytical model calculations from the model as trained on the Klinikum Goethe Universität (KGU) and European Radiation Dosimetry Group (EURADOS) data sets, respectively.

The large differences in leakage radiation seen in the measured profiles in Figure 3.6 are due to differences in the fluence modulation used for the different techniques, as well as variations in collimators and head shielding in various machines. For example, the increased leakage from the CyberKnife unit was likely due to reduced head shielding in order to facilitate the mounting of the linac on a robotic arm. On the other hand, the increased leakage from the wedged field technique was due to the greater beam-on time

Table 3.6. Gamma index criteria for selected pass rates when comparing the model as trained on the Klinikum Goethe Universität (KGU) and European Radiation Dosimetry Group (EURADOS) data sets to the anthropomorphic phantom data set for the Varian Clinac 21 iX. The criteria considered include relative dose difference, ΔD_R ; absolute dose difference, ΔD_A ; and distance to agreement in the therapeutic and out-of-field regions, Δd_t and Δd_{OOF} , respectively.

Training Data Set	Pass Rate	Therapeutic		Out-of-Field	
		ΔD_R (%)	Δd_t (mm)	ΔD_A ($\frac{mGy}{Gy}$)	Δd_{OOF} (mm)
KGU	100	8	18	3.5	0.5
	95	6	14	3.1	0.5
	90	4	10	2.2	0.5
	67	3	7	0.3	0.5
EURADOS	100	15	20	4.5	0.5
	95	11	16	3.9	0.5
	90	8	12	2.5	0.5
	67	6	8	0.6	0.5

required to produce wedged fields. Dose profiles from special techniques such as these should not be expected to closely match the dose profiles of more typical treatment techniques, *e.g.*, IMRT. By fitting the model parameters for each curve individually, it is possible to faithfully reproduce each of the measured dose profiles in a descriptive capacity (not shown), but additional development is necessary to extend the model to include explicit modeling of fluence modulation for predictive purposes.

3.4. Discussion

This work strongly suggests that there is potential for improving the completeness and accuracy of dose distribution calculations in routine clinical applications. The model is not intended to replace current methods of treatment planning, but could be used in conjunction with current methods to provide a level of accuracy for the dose far outside the treatment field that is not available from currently available commercial treatment planning systems. With further study, this model could be implemented for use in hand calculations of fetal dose in the case of a pregnant radiation therapy patient or the dose to implants

such pacemakers that may be damaged by radiation. Additionally, the ability to calculate therapeutic and stray radiation with a single model should be useful for studies in radiation epidemiology or as an educational tool for demonstrating the shape and relative magnitudes of the dose distributions from various treatment machines and techniques. Importantly, this may all be possible with a single analytical model that users may implement with measured data that is likely to already exist for their clinic.

The results of this study are consistent with previous works related to analytical models of total dose from external beam radiation therapy. In particular, the results achieved in this work agree well with those of a more complex model previously reported by Jagetic and Newhauser [26]. The model offers simplicity, easy portability to various treatment machines and techniques, and increased speed compared with the more detailed model of Jagetic and Newhauser.

Major strengths of this study include the large number of treatment machines and techniques considered. Whereas previous works have been limited to single treatment techniques, this work considers nine techniques delivered with seven treatment machines from four manufacturers. This is made possible by the simplicity of the reported model. Additionally, in demonstrating the accuracies that are achievable with such a simple model, this work informs about the tradeoff between accuracy and complexity for analytical dose models.

Limitations of this work include the limited amount of measured data taken for each treatment technique. Additionally, only the descriptive capabilities of the model have been examined in this work, and the model's ability to predict doses for treatments with different setup conditions has not been tested. This is not a serious limitation because a lookup table approach could be used to apply this model to many different setup conditions with only a few measurements required. Another limitation of the model, in its current form, is the lack of photoneutrons at beam energies greater than 10 MV. However, this is not a serious limitation because most external beam photon treatments are delivered with 6

MV beams. This is especially true of IMRT. Additionally, for beam energies up to 18 MV, the component of equivalent dose due to photoneutrons is a small fraction of that due to leakage photons [30]. Also, the model can be extended to include photoneutrons in future studies. Other future work should include testing the model for dosimetric accuracy under different treatment conditions, such as field size. Additionally, implementing the model into a treatment planning system would allow for further testing of the practicality of using analytical models of stray dose in clinical settings. Our research group has recently performed similar work by implementing an analytical model of neutron dose from passively-scattered proton therapy into a research treatment planning system [37].

3.5. Conclusion

In this work we developed a new, broadly-applicable analytical model of the total dose from external beam radiation therapy. The model provides very good accuracy, on average better than 10%, for both therapeutic and stray dose for a wide variety of treatment machines and techniques when compared with measured data. Importantly, the model developed here may be configured using non-proprietary configuration parameters and dosimetric data that is readily measurable in most clinics.

3.6. References

- ¹R. Harrison, “Introduction to dosimetry and risk estimation of second cancer following radiotherapy”, *Radiat Meas* **57**, 1–8 (2013).
- ²R. L. Siegel, K. D. Miller, and A. Jemal, “Cancer statistics, 2016”, *CA Cancer J Clin* **66**, 7–30 (2016).
- ³N. Howlader, A. M. Noone, M. Krapcho, J. Garshell, D. Miller, and S. F. Altekruse, *Seer cancer statistics review, 1975-2011*, Report (National Cancer Institute, 2014).
- ⁴National Research Council, *Health risks from exposure to low levels of ionizing radiation: beir vii – phase 2* (The National Academies Press, Washington, DC, 2006).
- ⁵NCRP, *Second primary cancers and cardiovascular disease after radiation therapy: NCRP Report No. 151*, National Council on Radiation Protection and Measurements, Bethesda, Maryland, 2011.

- ⁶G. T. Armstrong, M. Stovall, and L. L. Robison, “Long-term effects of radiation exposure among adult survivors of childhood cancer: results from the childhood cancer survivor study”, *Radiat Res* **174**, 840–50 (2010).
- ⁷I. Diallo, A. Lamon, A. Shamsaldin, E. Grimaud, F. de Vathaire, and J. Chavaudra, “Estimation of the radiation dose delivered to any point outside the target volume per patient treated with external beam radiotherapy”, *Radiother Oncol* **38**, 269–71 (1996).
- ⁸W. D. Newhauser, A. Berrington de Gonzalez, R. Schulte, and C. Lee, “A review of radiotherapy-induced late effects research after advanced technology treatments”, *Front Oncol* **6**, 13 (2016).
- ⁹W. D. Newhauser and M. Durante, “Assessing the risk of second malignancies after modern radiotherapy”, *Nat Rev Cancer* **11**, 438–48 (2011).
- ¹⁰W. Dorr and T. Herrmann, “Cancer induction by radiotherapy: dose dependence and spatial relationship to irradiated volume”, *J Radiol Prot* **22**, A117–21 (2002).
- ¹¹A. Ahnesjo, “Collapsed cone convolution of radiant energy for photon dose calculation in heterogeneous media”, *Med Phys* **16**, 577–92 (1989).
- ¹²T. Han, J. K. Mikell, M. Salehpour, and F. Mourtada, “Dosimetric comparison of acuros xb deterministic radiation transport method with monte carlo and model-based convolution methods in heterogeneous media”, *Med Phys* **38**, 2651–64 (2011).
- ¹³T. R. Mackie, J. W. Scrimger, and J. J. Battista, “A convolution method of calculating dose for 15-mv x rays”, *Med Phys* **12**, 188–96 (1985).
- ¹⁴R. Mohan, C. Chui, and L. Lidofsky, “Differential pencil beam dose computation model for photons”, *Med Phys* **13**, 64–73 (1986).
- ¹⁵M. Stovall, C. R. Blackwell, J. Cundiff, D. H. Novack, J. R. Palta, L. K. Wagner, E. W. Webster, and R. J. Shalek, “Fetal dose from radiotherapy with photon beams: report of aapm radiation therapy committee task group no. 36”, *Med Phys* **22**, 63–82 (1995).
- ¹⁶A. Joosten, F. Bochud, and R. Moeckli, “A critical evaluation of secondary cancer risk models applied to monte carlo dose distributions of 2-dimensional, 3-dimensional conformal and hybrid intensity-modulated radiation therapy for breast cancer”, *Phys Med Biol* **59**, 4697–722 (2014).
- ¹⁷S. F. Kry, U. Titt, D. Followill, F. Ponisch, O. N. Vassiliev, R. A. White, M. Stovall, and M. Salehpour, “A monte carlo model for out-of-field dose calculation from high-energy photon therapy”, *Med Phys* **34**, 3489–99 (2007).
- ¹⁸S. F. Kry, U. Titt, F. Ponisch, D. Followill, O. N. Vassiliev, R. A. White, R. Mohan, and M. Salehpour, “A monte carlo model for calculating out-of-field dose from a Varian 6 MV beam”, *Med Phys* **33**, 4405–13 (2006).

- ¹⁹M. A. Benadjaoud, J. Bezin, A. Veres, D. Lefkopoulos, J. Chavaudra, A. Bridier, F. de Vathaire, and I. Diallo, “A multi-plane source model for out-of-field head scatter dose calculations in external beam photon therapy”, *Phys Med Biol* **57**, 7725–39 (2012).
- ²⁰N. Chofor, D. Harder, K. C. Willborn, and B. Poppe, “Internal scatter, the unavoidable major component of the peripheral dose in photon-beam radiotherapy”, *Phys Med Biol* **57**, 1733–43 (2012).
- ²¹S. F. Kry, M. Salehpour, D. S. Followill, M. Stovall, D. A. Kuban, R. A. White, and I. Rosen, “Out-of-field photon and neutron dose equivalents from step-and-shoot intensity-modulated radiation therapy”, *Int J Radiat Oncol Biol Phys* **62**, 1204–16 (2005).
- ²²M. Stovall, S. S. Donaldson, R. E. Weathers, L. L. Robison, A. C. Mertens, J. F. Winther, J. H. Olsen, and J. Boice J. D., “Genetic effects of radiotherapy for childhood cancer: gonadal dose reconstruction”, *Int J Radiat Oncol Biol Phys* **60**, 542–52 (2004).
- ²³M. Stovall, R. Weathers, C. Kasper, S. A. Smith, L. Travis, E. Ron, and R. Kleinerman, “Dose reconstruction for therapeutic and diagnostic radiation exposures: use in epidemiological studies”, *Radiat Res* **166**, 141–57 (2006).
- ²⁴P. J. Taddei, W. Jalbout, R. M. Howell, N. Khater, F. Geara, K. Homann, and W. D. Newhauser, “Analytical model for out-of-field dose in photon craniospinal irradiation”, *Phys Med Biol* **58**, 7463–79 (2013).
- ²⁵P. H. van der Giessen, “Peridose, a software program to calculate the dose outside the primary beam in radiation therapy”, *Radiother Oncol* **58**, 209–13 (2001).
- ²⁶L. J. Jagetic and W. D. Newhauser, “A simple and fast physics-based analytical method to calculate therapeutic and stray doses from external beam, megavoltage x-ray therapy”, *Phys Med Biol* **60**, 4753–75 (2015).
- ²⁷M. J. Berger, J. H. Hubbell, S. M. Seltzer, J. Chang, J. S. Coursey, R. Sukumar, Z. D. S, and K. Olsen, *XCOM: Photon Cross Section Database (version 1.5)*, [Online] Available: <http://physics.nist.gov/xcom>. National Institute of Standards and Technology, Gaithersburg, MD. Online, <http://physics.nist.gov/xcom>, 2010.
- ²⁸J. Bordy, I. Bessiere, E. d’Agostino, C. Domingo, F. d’Errico, A. di Fulvio, Ž. Knežević, S. Miljanić, P. Olko, A. Ostrosky, B. Poumarede, S. Sorel, L. Stolarczyk, V. D., and R. Harrison, “Radiotherapy out-of-field dosimetry: experimental and computational results for photons in a water tank”, *Radiat Meas* **57**, 29–34 (2013).
- ²⁹Ž. Knežević, L. Stolarczyk, I. Bessieres, J. M. Bordy, S. Miljanić, and P. Olko, “Photon dosimetry methods outside the target volume in radiation therapy: optically stimulated luminescence (osl), thermoluminescence (tl) and radiophotoluminescence (rpl) dosimetry”, *Radiation Measurements* **57**, 9–18 (2013).

- ³⁰R. Kaderka, D. Schardt, M. Durante, T. Berger, U. Ramm, J. Licher, and C. La Tessa, “Out-of-field dose measurements in a water phantom using different radiotherapy modalities”, *Phys Med Biol* **57**, 5059–74 (2012).
- ³¹R. A. Halg, J. Besserer, and U. Schneider, “Systematic measurements of whole-body dose distributions for various treatment machines and delivery techniques in radiation therapy”, *Med Phys* **39**, 7662–76 (2012).
- ³²D. A. Low, W. B. Harms, S. Mutic, and J. A. Purdy, “A technique for the quantitative evaluation of dose distributions”, *Med Phys* **25**, 656–61 (1998).
- ³³J. Van Dyk, R. B. Barnett, J. E. Cygler, and P. C. Shragge, “Commissioning and quality assurance of treatment planning computers”, *Int J Radiat Oncol Biol Phys* **26**, 261–73 (1993).
- ³⁴R. M. Howell, S. B. Scarborough, S. F. Kry, and D. Z. Yaldo, “Accuracy of out-of-field dose calculations by a commercial treatment planning system”, *Phys Med Biol* **55**, 6999–7008 (2010).
- ³⁵A. Joosten, O. Matzinger, W. Jeanneret-Sozzi, F. Bochud, and R. Moeckli, “Evaluation of organ-specific peripheral doses after 2-dimensional, 3-dimensional and hybrid intensity modulated radiation therapy for breast cancer based on monte carlo and convolution/superposition algorithms: implications for secondary cancer risk assessment”, *Radiother Oncol* **106**, 33–41 (2013).
- ³⁶U. Schneider, R. A. Halg, M. Hartmann, A. Mack, F. Storelli, A. Joosten, R. Mockli, and J. Besserer, “Accuracy of out-of-field dose calculation of tomotherapy and cyberknife treatment planning systems: a dosimetric study”, *Z Med Phys* **24**, 211–5 (2014).
- ³⁷J. Eley, W. Newhauser, K. Homann, R. Howell, C. Schneider, M. Durante, and C. Bert, “Implementation of an analytical model for leakage neutron equivalent dose in a proton radiotherapy planning system”, *Cancers (Basel)* **7**, 427–38 (2015).

Chapter 4.

A Physics-Based Analytical Model of Absorbed Dose from Primary, Leakage, and Scattered Photons from Megavoltage Radiotherapy with MLCs

4.1. Introduction

The goal of modern radiation therapy is to eradicate or control diseased tissues and to spare healthy tissues to the greatest extent possible. The side effects of radiation exposure to healthy tissue range from mild to severe and can be categorized as either acute or late-occurring. Late-occurring side effects of radiation include ailments such as cardiac toxicity and radiation induced second cancers [1–4]. These effects can occur up to decades after treatment, including in tissues far from the location of the primary tumor [5]. In particular, most radiation induced second cancers occur outside of the treatment field boundaries [6]. It logically follows that radiation exposures from both therapeutic and stray radiation should be known in order to project treatment efficacy and radiation side effects.

Radiation therapy, along with surgery and chemotherapy, is one of the central treatment options available to cancer patients. Approximately one-half to two-thirds of cancer patients in developed nations receive radiation therapy at some point during their care [7]. Recent studies have confirmed that improvements in survival rates have led to an increasingly large population of cancer survivors and, therefore, an increasing prevalence of patients suffering from late-effects of radiation therapy [8–10]. This has caused mounting interest in research into accurately characterizing the dose to a patient’s whole body [4, 11, 12].

In external beam radiation therapy, the sparing of healthy tissue is achieved through the use of collimators to tightly conform the boundaries of the radiation field to shape of the planning target volume (PTV). However, lower levels of stray radiation, including scattered and leakage radiation, still reach a patient’s healthy tissues. Remarkably, contemporary clinical treatment planning systems accurately calculate the in-field dose but systematically

underestimate the absorbed dose outside of the PTV by 40–100% in some cases [13–18]. In the literature, far more attention has been paid to exposures in and immediately near the treatment field because their importance in controlling malignant disease [4, 19].

Attempts to characterize the stray radiation exposures from photon radiotherapy delivered with electron linacs have made use of measurements [20–22], Monte Carlo simulations [23–27], and empirical parameterizations [28–30]. Sánchez-Nieto et al. [31] reported an analytical model for calculating stray-dose from photon beams applicable along the midline of a patient in the isocentric plane at distances ≥ 10 cm from the field edge. A recent work from Hauri et al. [32] modeled patient-scattered radiation as a disk source and relied on machine specific parameterizations of head-scattered and leakage radiation. Previously, we demonstrated the feasibility of physics-based analytical models for calculating total body dose for 6-MV CRT [17]. Subsequently, we showed that such methods are broadly applicable to a wide variety of treatment machines and techniques [33]. However, these models were developed and validated only for the in- and cross-plane axes and approximated collimators as semi-infinite planes. Furthermore, the individual components of the stray dose model (leakage, head-scatter, and patient-scatter) were not verified by comparison with measurements or Monte Carlo simulations.

The objective of this work is to develop a new physics-based, analytical model of therapeutic and stray radiation that can calculate attenuation through clinically realistic collimator geometries including multileaf collimators (MLCs). Additionally, we aim to verify the dosimetric accuracy of all radiation components at all locations. We measured absorbed dose distributions from 6-MV beams incident on a water-box phantom to obtain data for configuring the model. We performed Monte Carlo simulations to independently determine the photon energy-fluence and dose from primary, leakage, and scattered photons. This allowed us to separately model the contributions to dose from each component and to realistically model the influence of the rounded and flat edges of the collimators.

4.2. Methods and Materials

4.2.1. Definitions

In the literature, the terminology and nomenclature used for the sources of stray radiation incident on a patient are myriad, ambiguous, and often inconsistent [12]. In this work, uncollided radiation refers to those photons generated in the tungsten target that have not interacted in any other object. Those uncollided photons that pass through the treatment aperture comprise the primary radiation field. The uncollided photons that travel through one or more beam-limiting devices without interacting are considered leakage radiation. Photons that undergo scattering events in the linac head are labeled head-scatter. Finally, patient-scattered radiation comprises photons that undergo scattering events within the patient or phantom.

4.2.2. Measurements

We took measurements of absorbed dose to serve as validation data for the analytical model described in Section 4.2.4. Measurements were taken with two active dosimeter types. The primary detector used was a Farmer-type ionization chamber (TM 30013, SN 009214, PTW, Freiburg, Germany). This is a waterproof chamber regularly used for both absolute and relative photon dosimetry. It has a sensitive volume of 0.6 cm^3 and a flat energy response from 30 kV to 50 MV photon-beam energy [34]. To ensure adequate spatial resolution in high-dose-gradient regions, we also measured with a waterproof solid-state diode dosimeter (TM 60012, SN 00579, PTW, Freiburg, Germany). The diode detector has a water-equivalent window thickness of 1.33 mm and a 1 mm^2 by $30 \text{ }\mu\text{m}$ thick circular sensitive volume. Measurements from both detectors were corrected for variations in photon spectral fluence following the methods of Chofer et al. [35, 36].

All measurements were performed at the Metrological ELeCtron Accelerator Facility (MELAF) at the *Physikalisch-Technische Bundesanstalt* (PTB) in Braunschweig, Germany [37]. The facility has two linacs (Precise Treatment SystemTM, SN 151605 and 151617, Elekta, Stockholm, Sweden) dedicated to metrology and research. The first of the linacs was

commissioned to deliver 6-, 10-, and 15-MV photon beams, and the other was commissioned for 4-, 8-, and 25-MV photon beams. The gantry angle was set to 270° for all measurements. Dose rates were controlled through the use of a high-precision transmission monitor system [38].

Measurements were conducted in air and in a water-box phantom. In both cases, detector positioning was accomplished using the PTB in-house scanning system. For the in-water measurements, a $60 \times 60 \times 60$ cm³ phantom with 1-cm thick plastic (polymethyl methacrylate or PMMA) walls with a water-equivalent thickness of 1.1 cm. The phantom was filled with distilled water and carefully positioned to achieve a source-to-surface distance (SSD) of 90 cm, placing isocenter at an axial distance of 10 cm distal to the upstream face of the phantom wall upon which the beam impinged. The phantom was positioned laterally such that isocenter was 11 cm from both the bottom and nearest lateral side faces of the phantom. This asymmetric positioning allowed for half-profile scans extending to an off-axis distance of 40 cm in both the x- and y-direction and depths of up to 40 cm while always maintaining at least 9 cm between the detector and phantom edge. Due to the finite detector size and 1.1 cm water-equivalent thickness of the phantom wall, the shallowest depth at which measurements were achievable was 2 cm. In order to ensure adequate side-scatter, a smaller $30 \times 30 \times 30$ cm³ water phantom, also with 1-cm thick plastic walls was abutted directly against the large phantom. A photograph of the measurement setup is displayed in Figure 4.1.

4.2.3. Monte Carlo Simulations

Monte Carlo simulations of absorbed dose were performed to serve as training data for the analytical model described in Section 4.2.4. We simulated the linac, water-box phantom, and vault of the PTB facility. Monte Carlo simulations of photon fluence and total absorbed dose were performed using the Monte Carlo N-Particle eXtended (MCNPX) transport code version 2.7 [39]. The model of the linac in use at PTB was designed based on schematics provided by the manufacturer [40]. We modeled all major beam modifying

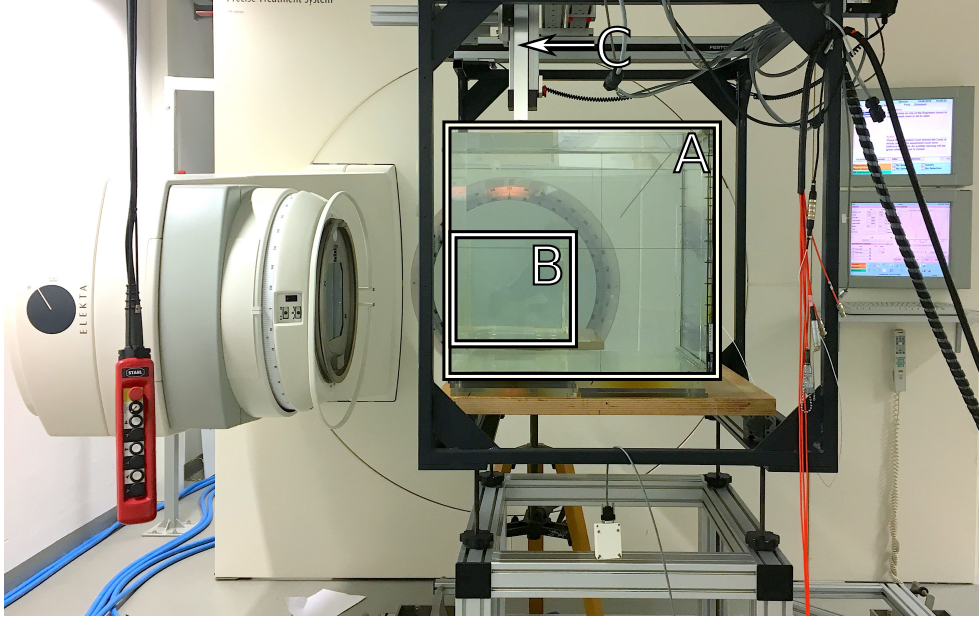


Figure 4.1. Photograph of measurement setup. The gantry is rotated to 270° with the upstream face of the phantom walls located at 90 cm SSD. The large phantom (A) is positioned in front of the linac aperture. The small phantom (B) is behind the large phantom in this photo. The arm used to scan the detectors is also visible (C).

Table 4.1. Measurement conditions for all absorbed dose profiles scanned in of this work.

Phantom	Field Size (cm^2)	Source-to-Measurement-Plane Distance (cm)	Scan Direction	Off-Axis Distance (cm)
In-Air	2×2	100	x	0, 10, 20, 30, 40
	10×10	"	"	"
Phantom	Field Size (cm^2)	Depth (cm)	Scan Direction	Off-Axis Distance (cm)
In-Water	2×2	3.5, 10, 20, 40	x, y	0, 10, 20, 30, 40
	4×4	"	"	"
	5×5	"	"	"
	10×10	"	"	"
	14×14	"	"	"
	20×20	"	"	"

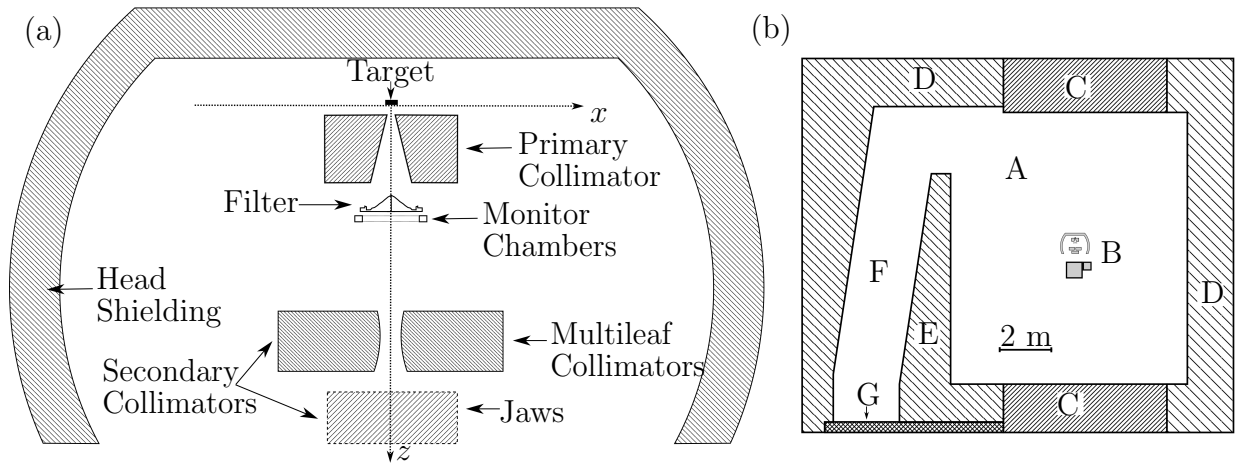


Figure 4.2. (a) Cross-sectional schematic view of linac head illustrating the relative locations of the beam-modifying and beam-limiting devices including the X-ray target, the cylindrical primary collimator, the flattening filter, the monitor chamber, the multi-leaf collimators (MLCs), and the jaws (not to scale). The location of the MLCs is rendered with a dotted line since the MLC leaves may not extend into the xz -plane for a given field. (b) Plan view of the vault geometry of the PTB metrology facility including A, the vault; B, linac head and phantoms; C, primary barriers; D, secondary barriers; E, inner-maze wall; F, maze; and G, door.

devices including the high-Z x-ray target, flattening filter, and monitor ionization chambers. The beam limiting devices modeled include the conical primary collimator, the multileaf collimator with backup diaphragm, and the jaws. Figure 4.2a illustrates the components of the linac treatment head. The gantry angle of the simulation matched the 270° angle employed for the physical measurements. The simulated field sizes included 2×2 , 5×5 , 10×10 , 14×14 , and 20×20 cm^2 .

The geometry, density, and material composition of the treatment vault were taken from as-built drawings and other design documents. The main area of the treatment vault is approximately 10×9 m^2 with a ceiling height of 5 m. The floor, ceiling, and all secondary barriers, including the maze walls, are shielded with standard concrete of density 2.38 g/cm^3 . The sections of the walls designated as primary barriers were shielded with heavy concrete of density 3.28 g/cm^3 . A plot of the treatment vault geometry is shown in Figure 4.2b. The $60 \times 60 \times 60$ - cm^3 and $30 \times 30 \times 30$ - cm^3 phantoms were positioned in the simulation exactly as they were for the measurements. Each phantom had 1-cm thick PMMA walls on the sides

and bottom. The water inside the large phantom was broken into 1-cm³ cubic voxels. The water-box phantoms in use at PTB were also modeled. Both photons and electrons were transported, and the total absorbed dose to each voxel was found by taking the sum of F6-type energy deposition lattice tallies for both particle types.

We used an F4-type lattice tally to determine the photon fluence in each voxel. In order to obtain the photon spectral fluence, we binned the fluence tally logarithmically between 1 eV and the maximum energy of electrons impinging on the target. To separate the total photon spectral fluence into the spectral fluence from uncollided, head-scattered, and patient-scattered photons, we used the TAG card to bin the F4 tally by the cell in which the photons were created. Photons created in the target or backing plate were summed to yield the uncollided photon spectral fluence. Photons created in the phantoms, including the water and the plastic walls, were summed to yield the patient-scattered spectral fluence. Photons created in other cells were binned and summed to yield the head-scattered spectral fluence. For each of these components, we found the photon energy fluence by multiplying each bin by its corresponding midpoint energy and summing over all energy bins. We found the mean photon energy of each component by dividing the photon energy fluence by the photon fluence.

Since the analytical absorbed-dose model described in Section 4.2.4 requires the mean photon energy at the point of calculation, we developed simple parameterizations of mean energy with location in the phantom for each of the three components described above, or

$$\bar{E}_n(x, y, z) = \bar{E}_{n,\text{cax}}(z) \times (1 - A_n(z) \times \text{CDF}_n(x, y, z)) \quad , \quad (4.1)$$

where $n = 1$ for uncollided photons, $n = 2$ for head-scattered photons, and $n = 3$ for patient-scattered photons. The mean energy along the beam's central axis is modeled as

$$\bar{E}_{n,\text{cax}}(z) = a_{\bar{E},n} \times z + b_{\bar{E},n} \quad , \quad (4.2)$$

where $a_{\bar{E},n}$ and $b_{\bar{E},n}$ are empirical fitting parameters. The cumulative normal function $\text{CDF}_n(x, y, z)$ governs the shape of the mean energy curve off-axis and is defined as

$$\text{CDF}_n(x, y, z) = \frac{1}{2} \left[1 + \text{erf} \left(\frac{\sqrt{x^2 + y^2} - f_n \times \frac{\text{FS} \times z}{2 \times z_{\text{iso}}}}{\sqrt{2} \times \sigma_{0,n} \times \frac{\text{FS} \times z}{2 \times z_{\text{iso}}}} \right) \right] , \quad (4.3)$$

where erf is the error function, FS is the side-length of the equivalent square of the field, and f_n and $\sigma_{0,n}$ are empirical fitting parameters. Finally, $A_n(z)$ governs the magnitude of the change in mean energy from central-axis to points far off-axis and is given by

$$A_n(z) = c_{\bar{E},n} \times z^2 + d_{\bar{E},n} \times z + e_{\bar{E},n} , \quad (4.4)$$

where $c_{\bar{E},n}$, $d_{\bar{E},n}$ and $e_{\bar{E},n}$ are empirical fitting parameters.

4.2.4. Analytical Model

4.2.4.1. Model Components

The model of absorbed dose comprises the sum of three terms, or

$$D_T(x, y, z) = D_P(x, y, z) + D_L(x, y, z) + D_{\text{HS}}(x, y, z) + D_{\text{PS}}(x, y, z) , \quad (4.5)$$

where $D_P(x, y, z)$ is the dose from primary photons, $D_L(x, y, z)$ is the dose from leakage photons, and $D_{\text{HS}}(x, y, z)$ and $D_{\text{PS}}(x, y, z)$ are the doses from head- and patient-scattered photons, respectively. The axes of the coordinates x and z are shown in Figure 4.2a with the y -axis extending out of the page and the origin located at the target. The four terms of the absorbed dose model are, in turn, based on models of photon energy fluence, Ψ . The total photon energy fluence is modeled as

$$\Psi(x, y, z) = \Psi_P(x, y, z) + \Psi_L(x, y, z) + \Psi_{\text{HS}}(x, y, z) + \Psi_{\text{PS}}(x, y, z) , \quad (4.6)$$

where $\Psi_P(x, y, z) + \Psi_L(x, y, z)$ represents the energy fluence from primary and leakage photons, $\Psi_{HS}(x, y, z)$ from head-scattered photons, and $\Psi_{PS}(x, y, z)$ from patient-scattered photons. These terms will be described in Section 4.2.4.4 and Sections 4.2.5 and 4.2.6.

4.2.4.2. Photon Source Model

Before describing the terms in Equation 4.6, we must describe the model of the photon source. The approach follows that of Jagetic and Newhauser [17], but with several important changes. While previous models have been based on modeling photon fluence and converting this to absorbed dose by assuming an average energy value, our model directly and explicitly models photon energy fluence, $\Psi(x, y, z)$.

In a medical linac, the primary photon fluence is produced by impinging a narrow beam of megavoltage electrons onto a tungsten target, thus generating bremsstrahlung photons. This bremsstrahlung radiation is sharply forward peaked. Often, a laterally-flat absorbed dose distribution is desired at the depth of the tumor, and so the flattening filter is designed to preferentially attenuate photons on and near the beam's central-axis. This results in a distribution that is flat at a depth of 10 cm in water, but which exhibits off-axis peaks, referred to as horns, at shallower depths. For this reason, the uncollimated photon energy fluence is modeled as the sum of three terms, or

$$\Psi_{UC}(x, y, z) = \sum_{i=1}^3 \Psi_i(x, y, z) \quad . \quad (4.7)$$

The first term, $\Psi_1(x, y, z)$, models the bulk of the flattened beam and is centered on the beam's central axis. The energy-weighted sum of the number of photons in each peak is calculated as

$$S_i = Y(T_0) \times T_0 \times \frac{Q_i}{e} \quad , \quad (4.8)$$

where Q_i is the total charge of electrons contributing to the i^{th} source term, e is the elementary charge, T_0 is the nominal energy of the electron beam (*i.e.*, 6 MeV), and $Y(T_0)$ is the thick target photon radiation yield for electrons of energy T_0 . This is a unitless quantity with value 0.2157 [41].

The first source term, denoted by $G_1(x, y, z)$, corresponds to the flat central region with Gaussian-like lateral fall-off and is modeled through the use of a cumulative normal function, or

$$\begin{aligned} G_1(x, y, z) &= \frac{S_1}{\sigma_{1,z}(z) \sqrt{2\pi}} \times \left\{ 1 - \alpha_{G_1} \times \int_{-\infty}^{\rho(x,y)} \exp\left(\frac{-\rho^2(x,y)}{2\sigma_{1,z}^2(z)}\right) d\rho(x,y) \right\} \\ &= \frac{S_1}{\sigma_{1,z}(z) \sqrt{2\pi}} \times \left\{ 1 - \alpha_{G_1} \times \left[\frac{1}{2} + \frac{1}{2} \operatorname{erf}\left(\frac{\rho^2(x,y)}{\sigma_{1,z}(z) \sqrt{2}}\right) \right] \right\} \end{aligned} \quad (4.9)$$

where S_1 is as defined in Equation 4.8, α_{G_1} is an empirical fitting parameter, $\rho(x, y)$ is the distance from the beam's central axis to the point of interest at (x, y) in the calculation plane, and $\sigma_{1,z}(z)$ is the width parameter projected to the calculation plane at distance z .

The second and third source terms are

$$G_i(x, y, z) = \frac{S_i}{\sigma_{i,z}(z) \sqrt{2\pi}} \exp\left[\frac{-(\rho^2(x, y) - \bar{\rho}_{i,z}(z))^2}{2\sigma_{i,z}^2(z)}\right], \text{ for } i = 2, 3 \quad (4.10)$$

where S_i is as defined in Equation 4.8, $\sigma_{i,z}(z)$ is the width parameter of the i^{th} Gaussian, $\rho(x, y)$ is the lateral distance of the calculation point from the central axis, and $\bar{\rho}_{i,z}(x, y, z)$ is the centroid of the i^{th} Gaussian projected to the plane of the point of calculation at distance z . The Gaussian width parameters and centroid positions scale with depth according to geometric magnification, or

$$\sigma_{i,z}(x, y, z) = \sigma_{i,0} \times \frac{z + d_0}{z} \quad (4.11)$$

$$\bar{\rho}_{i,z}(x, y, z) = \bar{\rho}_{i,0} \times \frac{z + d_0}{z} \quad (4.12)$$

where $\sigma_{i,0}$, $\bar{\rho}_{i,0}$, and d_0 are empirically determined fitting parameters of the model with d_0 representing the location of the photon virtual source (see Figure 4.3).

Using the terms described in Equations 4.9 and 4.10, the uncollimated photon energy fluence from the i^{th} Gaussian source, $\Psi_i(x, y, z)$, is defined as

$$\Psi_i(x, y, z) = \frac{G_i(x, y, z)}{4\pi [r_i(x, y, z)]^p}, \text{ for } i = 1, 2, 3 \quad , \quad (4.13)$$

where p is an exponent that governs the divergence and $r_i(x, y, z)$ represents the distance from the centroid of the i^{th} Gaussian in the source plane to the point of interest calculated according to

$$r_i(x, y, z) = \sqrt{\rho_i(x, y)^2 + z^2} \quad , \quad (4.14)$$

where $\rho_i(x, y)$ is defined as

$$\rho_i(x, y) = \sqrt{x^2 + y^2} - \bar{\rho}_{i,0} \quad . \quad (4.15)$$

4.2.4.3. Model of Primary Collimator Attenuation

Section 4.2.4.2 described the model of the photon source energy fluence in-air. To determine the photon energy fluence incident on the patient, we must to model photon attenuation through the various beam limiting devices (BLDs) to obtain the collimated photon energy fluence. As shown in Figure 4.2, the BLD nearest to the target is the primary collimator, which has the form of a cylinder made of tungsten alloy with an aperture in the center in the shape of a conical frustum. Figure 4.3 shows a cutaway drawing of the primary collimator including the dimensions used by the model.

In order to model the collimation of the photon energy fluence at a given point of calculation, (x, y, z) , we must find the thickness of the primary collimator as seen by a ray from each of the three source locations to the calculation point. We define the ray angle, θ ,

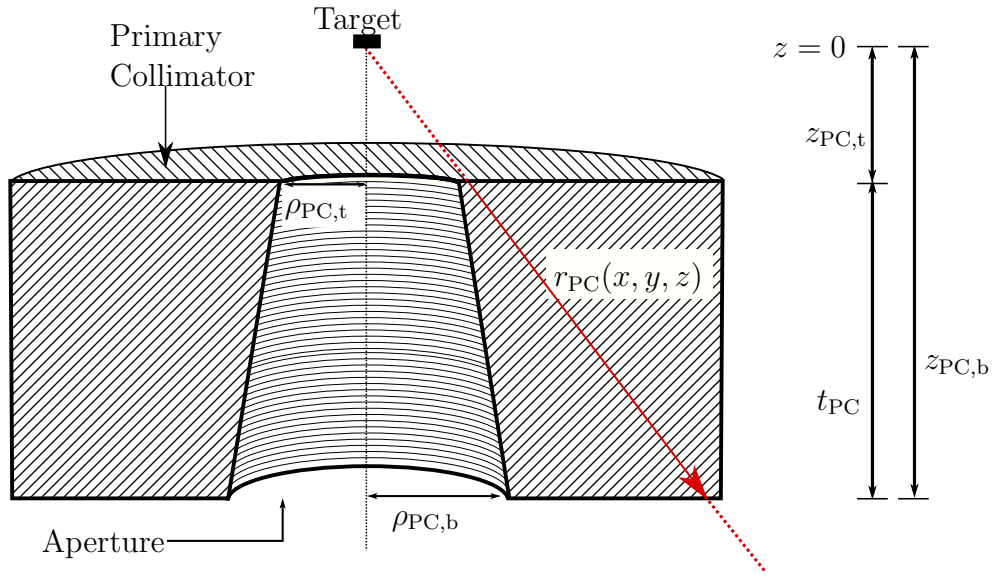


Figure 4.3. Cutaway illustration showing a 3D drawing of half of the primary collimator. $\rho_{PC,0}$ is the radius of the aperture at the bottom face of the primary collimator. t_{pc} is the vertical thickness of the primary collimator. $r_{PC}(x, y, z)$ is the length of a ray passing through the primary collimator used in determining the attenuation.

from the i^{th} source to the calculation point as

$$\theta_i(x, y, z) = \tan^{-1}\left(\frac{\rho_i(x, y)}{z}\right) \quad , \quad (4.16)$$

where $\rho_i(x, y)$ is as defined in Equation 4.15. As illustrated in Figure 4.3, the distance that a ray emanating from the i^{th} source travels through the primary collimator is

$$r_{i,PC}(x, y, z) = \frac{z_{i,PC}(x, y, z)}{\cos[\theta(x, y, z)]} \quad , \quad (4.17)$$

where $z_{i,PC}(x, y, z)$ is the projection of $r_{i,PC}(x, y, z)$ onto the z-axis and is calculated as

$$z_{i,PC}(x, y, z) = \begin{cases} 0, & \text{for } \frac{\rho_i(x, y)}{z} < \frac{\rho_{i,PC}(x, y)}{z_{PC,b}} \\ z_{PC,b} - \frac{b_{i,PC}(x, y)}{\frac{\rho_i(x, y)}{z} - m_{i,PC}}, & \text{for } \frac{\rho_{i,PC}(x, y)}{z_{PC,b}} \leq \frac{\rho_i(x, y)}{z} < \frac{\rho_{i,PC}(x, y)}{z_{PC,t}} \\ z_{PC,b} - z_{PC,t} & \text{for } \frac{\rho_i(x, y)}{z} \geq \frac{\rho_{i,PC}(x, y)}{z_{PC,t}} \end{cases} \quad . \quad (4.18)$$

The transmission factor of the primary-collimator is calculated from $r_{i,\text{PC}}(x, y, z)$ as

$$\text{TF}_{i,\text{PC}}(x, y, z) = \exp\left[-\alpha_{\mu,\text{PC},i} \times \mu_{\text{C}}(\bar{E}_1(x, y, z)) \times r_{i,\text{PC}}(x, y, z)\right] \quad , \quad (4.19)$$

where $\mu_{\text{C}}(\bar{E}_1(x, y, z))$ is the linear attenuation coefficient of the collimator material found using the methods of Sutcliffe [42] for photons of energy $\bar{E}_1(x, y, z)$, and $\alpha_{\mu,\text{PC},i}$ is an empirical adjustment factor to the primary collimator attenuation for the i^{th} source.

4.2.4.4. Model of Secondary Collimator Attenuation

After the primary collimator, the field passes through two sets of secondary collimators. The jaws and MLC leaves are flat on all sides except for the inward faces of the MLC leaves that define the edge of the field, which are circular arcs. Boyer and Li [43] previously reported an analytical formula for determining the special case of the distance a ray from the photon source to the isocentric plane must travel through a rounded collimator edge. Here, we present a general solution for rays extending to any z . Figure 4.4 shows a cross-section of the shape used to model the secondary collimators with the relevant dimensions labeled.

For a ray tangent to the circular face of the collimator emanating from i^{th} Gaussian source, x_{tan} and z_{tan} are the distances to the tangent point from the x - and z -axes as shown in Figure 4.4. Since these distances are not known *a priori*, we calculate their ratio according to

$$\frac{x_{\text{tan}}}{z_{\text{tan}}} = \frac{z_j \times (-x_{j,k} - R_j) + R_j \sqrt{z_j^2 + (x_{j,k} + R_j)^2 - R_j^2}}{R_j^2 - z_j^2} \quad . \quad (4.20)$$

Rays with $\theta_x < \tan^{-1}(x_{\text{tan}}/z_{\text{tan}})$ do not intersect the collimator. For those rays that do intersect the collimator, the distance traveled through the collimator depends upon the surfaces through which the ray enters and exits, as illustrated in two dimensions in Figure 4.5. For simplicity, let us first consider the case of rays limited to the in- and cross-planes. In order to determine the path length a given ray takes through the collimator,

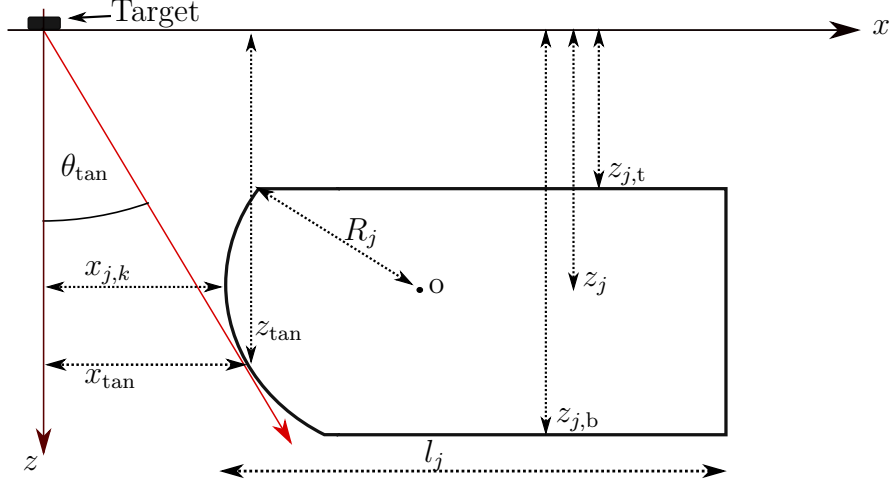


Figure 4.4. Schematic cross-sectional view of an MLC leaf. The index j is 2 if the collimator is an an MLC. The length of the collimator is denoted l_j . The point o marks the origin of the circular arc that defines the collimator edge, and R_j is the arc's radius. z_j is the z -distance from the photon source to the point, o , with $z_{j,t}$ and $z_{j,b}$ labeling the upstream and downstream faces of the collimator, respectively. θ_{tan} is the angle that a tangent ray from the source to the circular collimator face makes with the z -axis, with x_{tan} and z_{tan} being the coordinates of the tangent point. The distance from the photon-beam central-axis to the tip of the collimator is $x_{j,k}$ where k denotes whether this is a positive or negative side collimator. Note: Drawing not to scale.

we must determine the z -values at which it enters and exits the collimator. The z -values of the top and bottom of the collimators are known. For rays that pass through the circular face of the collimator (surface F in Figure 4.5), the z -values at which the ray intersects the imaginary circle that defines the curvature can be calculated as the solutions to a quadratic equation, or

$$z_{j,k,t,F}(x, z) = \frac{z \left(R_j x + x x_{j,k} + z z_j - \sqrt{R_j^2 x^2 - (x_{j,k} z - x z_j)^2 + 2 R_j z (x z_j - x_{j,k} z)} \right)}{x^2 + y^2} \quad (4.21)$$

and

$$z_{j,k,b,F}(x, z) = \frac{z \left(R_j x + x x_{j,k} + z z_j + \sqrt{R_j^2 x^2 - (x_{j,k} z - x z_j)^2 + 2 R_j z (x z_j - x_{j,k} z)} \right)}{x^2 + y^2}, \quad (4.22)$$

where $z_{j,k,t,F}$ and $z_{j,k,b,F}$ are the z -locations at which the ray enters and exits the rounded collimator face, respectively.

Next, we determine the two z -values of interest for any ray traveling in in-plane or cross-plane (*i.e.*, in the $x - z$ - or $y - z$ -planes). The z -value at which the ray enters the collimator is

$$z_{j,k,t,c}(x, z) = \begin{cases} \text{N/A} & \text{for } \frac{x}{z} \leq \frac{x_{\text{tan}}}{z_{\text{tan}}} \\ & \text{or } \frac{x}{z} > \frac{x_{j,k} + l_j}{z_{jt}} \\ z_{j,k,t,F}(x, z), & \text{for } \frac{x}{z} > \frac{x_{\text{tan}}}{z_{\text{tan}}} \\ & \text{and } z_{j,k,t,F}(x, z) \geq z_{jt} \\ z_{jt}, & \text{for } z_{j,k,t,F}(x, z) < z_{jt} \\ & \text{and } \frac{x}{z} \leq \frac{x_{j,k} + l_j}{z_{jt}} \end{cases}, \quad (4.23)$$

where $z_{j,k,t,F}(x, z)$ is as defined in Equation 4.21 and the z -value at which the ray exits the collimator is

$$z_{j,k,b,c}(x, z) = \begin{cases} \text{N/A} & \text{for } \frac{x}{z} \leq \frac{x_{\text{tan}}}{z_{\text{tan}}} \\ & \text{or } \frac{x}{z} > \frac{x_{j,k}+l_j}{z_{jt}} \\ z_{j,k,b,F}(x, z), & \text{for } \frac{x}{z} > \frac{x_{\text{tan}}}{z_{\text{tan}}} \\ & \text{and } z_{j,k,b,F}(x, z) \leq z_{jb} \\ z_{jb}, & \text{for } z_{j,k,b,F}(x, z) > z_{jt} \\ & \text{and } \frac{x}{z} \leq \frac{x_{j,k}+l_j}{z_{jb}} \\ \frac{y z_{jr} z}{y}, & \text{for } \frac{x}{z} > \frac{x_{j,k}+l_j}{z_{jb}} \\ & \text{and } \frac{x}{z} \leq \frac{x_{j,k}+l_j}{z_{jt}} \end{cases}, \quad (4.24)$$

where $z_{j,k,b,F}(x, z)$ is as defined in Equation 4.22. In Equations 4.23 and 4.24, N/A indicates that a ray does not intersect the collimator.

The preceding formulas are sufficient for rays limited to in- and cross-planes, but in order to describe other rays we must consider the 3-dimensional case. Figure 4.6 illustrates the additional types of rays to consider when modeling the horizontal extent, including front-side (FS), top-side (TS), front-rear (FR), side-bottom (SB), side-rear (SR), and side-side (SS).

Once the z -values of entry and exit have been determined (Equations 4.23 and 4.24), the total distance traveled through the collimator is subsequently calculated as

$$r_{j,k}(x, y, z) = \frac{z_{j,k,b}(x, y, z) - z_{j,k,t}(x, y, z)}{\cos[\theta(x, y, z)]}. \quad (4.25)$$

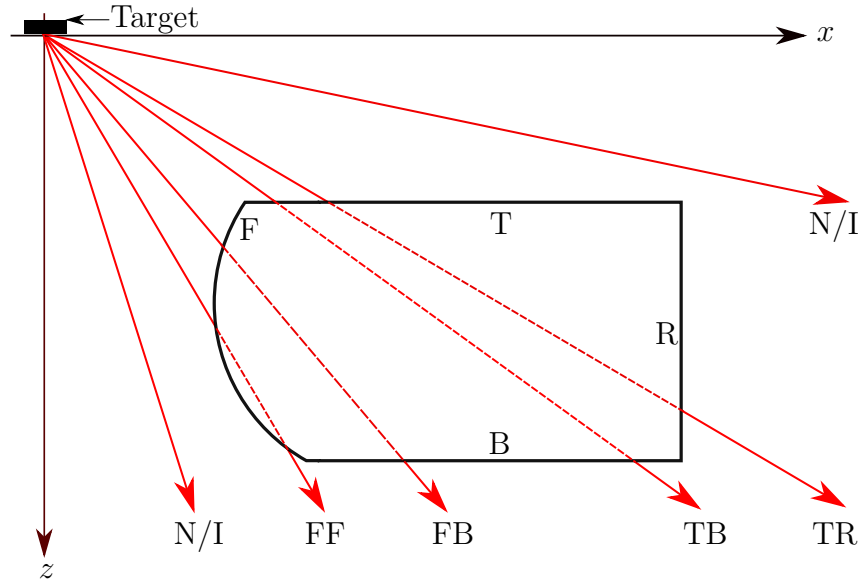


Figure 4.5. 2-dimensional drawing of an MLC leaf illustrating the types of rays that must be considered. Surfaces are labeled F (front), T (top), B (bottom), and R (rear). Rays marked N/I (non-intersecting) are those rays that do not pass through the collimator material. The other rays are labeled according to the surfaces through which they enter and exit the collimator: FF (front-front), FB (front-bottom), TB (top-bottom), and TR (top-rear).

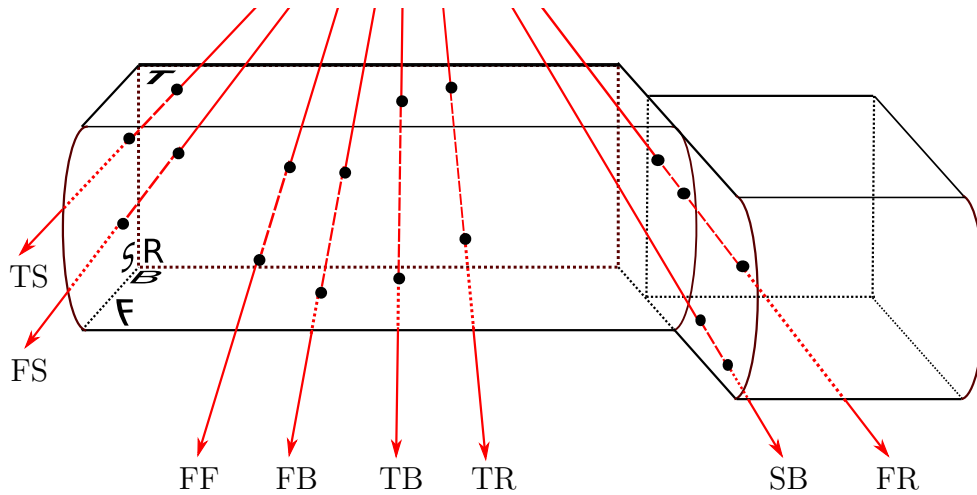


Figure 4.6. 3-dimensional schematic drawing of secondary collimator leaves, illustrating the effect of considering the horizontal extent. The labels F, B, T, and R correspond to those in Figure 4.5 with the addition of S (side). The four central rays, FF through TR, are similar to the four intersecting rays illustrated in Figure 4.5. However, the two leftmost rays illustrate that it is also possible for a ray to enter through either the front or the top of the collimator and leave through surface S (side). The offset section of collimator on the right demonstrates the additional types of rays to consider for offset MLC leaves where rays may enter through the side and exit through the bottom (B), rear (R), or the other side (S).

The transmission factor of the ray through the collimator is

$$\text{TF}_{j,k}(x, y, z) = \exp[-\alpha_{\mu,j,k} \times \mu_C(\bar{E}_1(x, y, z)) \times r_{j,k}(x, y, z)] \quad , \quad (4.26)$$

where $\alpha_{\mu,j,k}$ is an empirical adjustment factor to the attenuation coefficient of the collimator.

The final step before converting photon energy fluence to dose was to calculate the attenuation due to the phantom. The phantom was modeled as a box of water of unit density. The distance through water along a ray from the i^{th} source to the point of calculation is given by

$$r_{i,w}(x, y, z) = r_i(x, y, z) \frac{z}{\text{SSD}} \quad . \quad (4.27)$$

From this, the transmission factor is calculated as

$$\text{TF}_{i,w}(x, y, z) = \exp[-\alpha_{\mu,i} \mu_w(\bar{E}_1(x, y, z)) \times r_{i,w}(x, y, z)] \quad , \quad (4.28)$$

where $\mu_w(\bar{E}_1(x, y, z))$ is the linear attenuation coefficient for photons of energy $\bar{E}_1(x, y, z)$ in water as calculated via the methods of Sutcliffe [42]. Then, the energy fluence of primary and leakage photons, $\Psi_P(x, y, z) + \Psi_L(x, y, z)$, can be found by applying the transmission factors (Equations 4.19, 4.26 and 4.28) to the uncollimated energy fluence from Equation 4.13, or

$$\Psi_P(x, y, z) + \Psi_L(x, y, z) = \Psi_{\text{UC}}(x, y, z) \times \text{TF}_{\text{PC}}(x, y, z) \times \prod_{j=1}^2 \prod_{k=1}^2 [\text{TF}_{j,k}(x, y, z)] \times \text{TF}_w(x, y, z) \quad . \quad (4.29)$$

We then convert photon energy fluence to absorbed dose according to

$$D_P(x, y, z) + D_L(x, y, z) = (\Psi_P(x, y, z) + \Psi_L(x, y, z)) \times \left(\frac{\mu_{\text{en}}}{\rho} \right)_{\bar{E}_1(x,y,z)} \quad , \quad (4.30)$$

where $(\mu_{\text{en}}/\rho)_{\bar{E}_1(x,y,z)}$ is the photon mass-energy-absorption coefficient in water for photons of energy equal to the average energy of primary and leakage photons passing through (x, y, z) . As for the linear attenuation coefficients, the mass-energy-absorption coefficient values for all energies were calculated from a parameterization reported by Sutcliffe [42]. In the interest of space, the models of head- and patient-scattered dose can be found in ???. Plugging Equations 4.30, 4.42 and 4.55 into Equation 4.5 yields the total absorbed dose at the point of calculation, (x, y, z) .

4.2.5. Model of Head-Scattered Radiation

The model of head-scattered photon energy fluence comprises two terms, or

$$\Psi_{\text{HS}}(x, y, z) = \Psi_{\text{HS},1}(x, y, z) + \Psi_{\text{HS},2}(x, y, z) \quad . \quad (4.31)$$

The first head-scatter term is narrower than the second and primarily accounts for the head-scattered radiation present in and very near to the treatment field. It is defined by

$$\Psi_{\text{HS},1}(x, y, z) = A_{\text{HS},1} \times C_{\text{HS}}(x, y, z) \times \text{TF}_{\text{HS},w}(x, y, z) \quad , \quad (4.32)$$

where $A_{\text{HS},1}$ is a field-size dependent scaling factor, $C_{\text{HS}}(x, y, z)$ models the lateral extent of the head-scattered energy fluence, and $\text{TF}_{\text{HS},w}(x, y, z)$ models the attenuation of head-scattered energy fluence through water.

The amount of head-scattered photon energy fluence reaching the phantom increases with increasing field area [17, 44]. Thus, the amplitude of the photon energy fluence reaching the plane of calculation depends on the field-size of interest and was estimated empirically according to

$$A_{\text{HS},1} = \kappa_{\text{HS},1} \times (x_s \times y_s)^{p_{\text{HS},1}} \quad , \quad (4.33)$$

where $\kappa_{\text{HS},1}$ is a constant of proportionality; x_s and y_s are the x - and y -direction field side lengths, respectively; and the exponent, $p_{\text{HS},1}$, governs the dependence of the amplitude on field size.

The lateral extent of $\Psi_{\text{HS},1}(x, y, z)$ is modeled with cumulative normal functions, or

$$\begin{aligned}
C_{\text{HS}}(x, y, z) = & \\
& 1 - \{ [1 - \text{cnorm}(x, y, z, x_{1,s}(z), \sigma_{x,\text{HS},1}(z)) + \text{cnorm}(x, y, z, x_{2,s}(z), \sigma_{x,\text{HS},1}(z))] \\
& + [1 - \text{cnorm}(x, y, z, x_{1,s}(z), \sigma_{x,\text{HS},1}(z)) + \text{cnorm}(x, y, z, x_{2,s}(z), \sigma_{x,\text{HS},1}(z))] \} \quad (4.34) \\
& \times [1 - \text{cnorm}(x, y, z, y_{1,s}(z), \sigma_{y,\text{HS},1}(z)) + \text{cnorm}(x, y, z, y_{2,s}(z), \sigma_{y,\text{HS},1}(z))] \}
\end{aligned}$$

where $x_{1,s}$ is the distance from the central axis to the field edge in the $-x$ -direction, $x_{2,s}$ is the distance from the central axis to the field edge in the $+x$ -direction, and $y_{1,s}$ and $y_{2,s}$ are the same for the y -direction, all projected to the plane of calculation. The penumbral width is controlled by the width parameters defined as

$$\sigma_{x,\text{HS},i}(z) = m_{x,i} \times (z - z_{\text{iso}}) + \sigma_{\text{HS}_{x,i}}^{\text{iso}} \quad , \quad (4.35)$$

$$\sigma_{y,\text{HS},i}(z) = m_{y,i} \times (z - z_{\text{iso}}) + \sigma_{\text{HS}_{y,i}}^{\text{iso}} \quad , \quad (4.36)$$

where $\sigma_{\text{HS}_{x,i}}^{\text{iso}}$ and $\sigma_{\text{HS}_{y,i}}^{\text{iso}}$ are the penumbral widths at the depth of isocenter, $m_{x,i}$ and $m_{y,i}$ are empirical adjustments to the geometric magnification, and $i = 1$ for the first head-scattered term. The cumulative normal function is defined in the usual way as

$$\text{cnorm}(x, y, z, x_{i,s}(z), \sigma(z)) = \frac{1}{\sigma(z)\sqrt{2\pi}} \times \left[\frac{1}{2} + \frac{1}{2} \text{erf} \left(\frac{\rho^2(x, y)}{\sigma(z)\sqrt{2}} \right) \right] \quad , \quad (4.37)$$

where erf denotes the error function.

The second head-scatter term is broader than the first and accounts for the majority of head-scattered energy fluence outside of the treatment field. It is defined as

$$\Psi_{\text{HS},2}(x, y, z) = A_{\text{HS},2} \times G_{\text{HS}}(x, y, z) \times \text{TF}_{\text{HS,w},}(x, y, z) \times \text{GF}_{\text{HS}}(x, y, z) \quad , \quad (4.38)$$

where $A_{\text{HS},2}$ is a field size dependent scaling factor, $G_{\text{HS}}(x, y, z)$ models the lateral extent, $\text{TF}_{\text{HS,w},}(x, y, z)$ models attenuation in water, and $\text{GF}_{\text{HS}}(x, y, z)$ models the increase in head-scattered fluence out-of-field in regions not covered by the secondary collimators.

As with the first term, the magnitude of $\Psi_{\text{HS},2}(x, y, z)$ varies with field size and is modeled similarly to Equation 4.33, or

$$A_{\text{HS},2} = \kappa_{\text{HS},2} \times (x_s \times y_s)^{p_{\text{HS},2}} \quad . \quad (4.39)$$

The second head-scatter term is modeled as a Gaussian in the x - and y -directions according to

$$G_{\text{HS}}(x, y, z) = \frac{1}{\sigma_{x,\text{HS},2}(z) \times \sigma_{y,\text{HS},2}(z) \times 2\pi} \exp\left(\frac{-x^2}{2\sigma_{x,\text{HS},2}^2(z)}\right) \times \exp\left(\frac{-y^2}{2\sigma_{y,\text{HS},2}^2(z)}\right) \quad , \quad (4.40)$$

where $\sigma_{x,\text{HS},2}(z)$ and $\sigma_{y,\text{HS},2}(z)$ are as defined in Equations 4.35 and 4.36 for the case $i = 2$.

In out-of-field regions that are not covered by the secondary collimators (gap regions), head-scattered radiation must pass through the primary collimator and head-shielding, but avoids the jaws and multileaf collimator. One might suspect that this reduction in mass thickness as seen by a ray emanating from the source would result in decreased energy fluence head-scatter, but the photon energy fluence actually increases in these regions due to the reduction in self-attenuation of head-scatter in the collimator material. We modeled this increase in photon energy fluence in the gap regions simply as the ratio of the secondary collimator transmission factor at the calculation point to the product of the transmission

factor at the point of calculation. This gap factor is defined as

$$\text{GF}_{\text{HS}}(x, y, z) = q_{\text{HS}} \left(\frac{\text{TF}_{\text{Jaw}}(x, y, z) \times \text{TF}_{\text{MLC}}(x, y, z)}{\text{TF}_{\text{Jaw}}(x, 0, z) \times \text{TF}_{\text{MLC}}(0, y, z)} \right) , \quad (4.41)$$

where TF_{Jaw} and TF_{MLC} are as defined in Equation 4.26, and q_{HS} is a empirical constant of proportionality that determines how this ratio translates into increased head-scattered energy fluence.

Finally, we convert the head-scattered energy fluence as calculated in Equation 4.31 into absorbed dose similarly to Equation 4.30, or

$$D_{\text{HS}}(x, y, z) = \Psi_{\text{HS}}(x, y, z) \times \left(\frac{\mu_{\text{en}}}{\rho} \right)_{\bar{E}_2(x, y, z)} , \quad (4.42)$$

where $\bar{E}_2(x, y, z)$ is the average energy of head-scattered photons at point (x, y, z) from Equation 4.1, and $(\mu_{\text{en}}/\rho)_{\bar{E}_2(x, y, z)}$ is the mass energy absorption coefficient in water for photons of energy $\bar{E}_2(x, y, z)$ calculated using the methods of Sutcliffe [42].

4.2.6. Model of Patient-Scattered Radiation

Similarly to the head-scattered radiation model, the model of patient-scattered radiation comprises two terms, or

$$\Psi_{\text{PS}}(x, y, z) = \Psi_{\text{PS},1}(x, y, z) + \Psi_{\text{PS},2}(x, y, z) , \quad (4.43)$$

Also, similarly to the head-scattered radiation, the amplitude of the patient-scattered radiation function depends on the field-area. This was modeled empirically as

$$A_{\text{PS}} = \kappa_{\text{PS}} \times (x_s \times y_s)^{p_{\text{PS}}} , \quad (4.44)$$

where κ_{PS} is a constant of proportionality and the exponent, p_{PS} , governs the dependence on field-size.

Unlike the other components of fluence, patient-scattered radiation is generated inside the phantom. The build-up of patient scattered energy fluence was modeled according to

$$B_{PS}(z) = 1 - \exp[-\alpha_B \times (z - SSD + z_B)] \quad (4.45)$$

where α_B controls the rate at which the patient-scattered energy fluence builds up with depth in water along the z -axis, and z_B is a backscatter factor that prevents the patient-scatter from falling to zero at the surface. With Equations 4.44 and 4.45 we define the model of patient-scattered photon energy fluence along the central axis as

$$\Psi_{PS,cax}(z) = A_{PS} \times B_{PS}(z) \times TF_{PS}(0, 0, z) \quad (4.46)$$

where $TF_{PS}(z)$ is the transmission factor for patient scattered energy fluence.

Both patient-scatter terms are modeled as Gaussian sources, or

$$G_{PS,i}(x, y, z) = \frac{1}{\sigma_{PS,i}(z)\sqrt{2\pi}} \times \exp\left[\frac{-\rho^2(x, y)}{2\sigma_{PS,i}^2}(z)\right] \quad , \quad (4.47)$$

where $\sigma_{PS,i}(z)$ is the Gaussian width parameter which is parameterized with depth according to

$$\sigma_{PS,i}(z) = k_{PS,i} \times (z - SSD) + \sigma_{PS,i}^{surf} \quad , \quad (4.48)$$

where $\sigma_{PS,i}^{surf}$ is the width parameter of the i^{th} patient-scatter source at the surface of the phantom and $k_{PS,i}$ is an empirical adjustment factor to the geometric magnification.

Again, the first of the two patient-scatter terms is narrower than the second, accounting for the majority of patient-scattered radiation in and near the treatment field. It is modeled as originating on the central axis at the depth of calculation such that attenuation is modeled as traveling along a horizontal ray from the central axis to the point of calculation as in

$$TF_{PS,w,1}(x, y) = \exp(-\alpha_{\mu_{PS}} \times \mu_{PS} \times \rho(x, y)) \quad (4.49)$$

where μ_{PS} is the linear attenuation coefficient for patient-scattered photons and $\alpha_{\mu_{\text{PS}}}$ is an empirical adjustment factor. The complete first term of patient-scattered energy fluence is then

$$\Psi_{\text{PS},1}(x, y, z) = c_{\text{PS}} \times \Psi_{\text{PS,cax}}(z) \times G_{\text{PS},1}(x, y, z) \times \text{TF}_{\text{PSw},1}(x, y) \times \left(\frac{r(z)}{r(x, y, z)} \right)^p \quad (4.50)$$

where c_{PS} is an empirically determined number between 0 and 1 that apportions the central axis dose between the first and second patient-scatter terms.

The second patient-scatter term is modeled as originating above the plane of calculation. Though all patient-scattered fluence is generated within the phantom, the amount of patient-scattered present at a location in the phantom depends on the amount of primary, leakage, and head-scattered radiation traveling from the treatment head toward the point of calculation. This in turn depends on the thickness of collimation present along a ray from the primary photon source to the point of calculation. The influence of collimation on the patient-scattered energy fluence modeled with cumulative normal functions as in

$$\begin{aligned} C_{\text{PS}}(x, y, z) = & [1 - \text{cnorm}(x, y, z, x_{1,s}(z), \sigma_{\text{PS},2}(z)) + \text{cnorm}(x, y, z, x_{2,s}(z), \sigma_{\text{PS},2}(z))] \\ & + [\text{cnorm}(x, y, z, x_{1,s}(z), \sigma_{\text{PS},2}(z)) - \text{cnorm}(x, y, z, x_{2,s}(z), \sigma_{\text{PS},2}(z))] \quad (4.51) \\ & \times [1 - \text{cnorm}(x, y, z, y_{1,s}(z), \sigma_{\text{PS},2}(z)) + \text{cnorm}(x, y, z, y_{2,s}(z), \sigma_{\text{PS},2}(z))] . \end{aligned}$$

The transmission factor is then given by

$$\begin{aligned} \text{TF}_{\text{PS,col}}(x, y, z) = & C_{\text{PS}}(x, y, z) \\ & \times \left\{ -1 + \exp \left[-\alpha_{\mu_{\text{col}}} \times \mu_{\text{C}}(\bar{E}_1(x, y, z)) \times \frac{t_{\text{col}}}{\cos(\theta(x, y, z))} \right] \right\} \quad (4.52) \end{aligned}$$

where t_{col} is the averaged thickness of the jaw and multileaf collimator and $\alpha_{\mu_{\text{col}}}$ is an empirical correction factor to the mean linear attenuation coefficient of the collimator material.

Similarly to the head-scatter model, there is additional fluence present along the diagonals in regions outside the shadow of the secondary collimators. To model this increase in fluence, we define a gap factor similar to Equation 4.41 for head-scatter, or

$$\begin{aligned} \text{GF}_{\text{PS}}(x, y, z) = & 1 + (\alpha_{q,\text{PS}} \times \text{FA} + \beta_{q,\text{PS}}) \\ & \times \left[\left(\frac{\text{TF}_{\text{Jaw}}(x, y, z) \times \text{TF}_{\text{MLC}}(x, y, z)}{\text{TF}_{\text{Jaw}}(x, 0, z) \times \text{TF}_{\text{MLC}}(0, y, z)} \right) - 1 \right] \quad , \end{aligned} \quad (4.53)$$

where the coefficient q_{PS} is a constant of proportionality that determines the magnitude of increase in patient-scattered energy fluence. The complete second term for patient-scattered energy fluence is then given by

$$\begin{aligned} \Psi_{\text{PS},2}(x, y, z) = & \Psi_{\text{PS,cax}}(z) \times (1 - c_{\text{ps}}) \times G_{\text{PS},2}(x, y, z) \times \left(\frac{r(z)}{r(x, y, z)} \right)^p \\ & \times \text{GF}_{\text{PS}}(x, y, z) \times \text{TF}_{\text{PS,col}}(x, y, z) \times \text{TF}_{\text{PS}}(x, y, z) \quad . \end{aligned} \quad (4.54)$$

Again following the method of Equation 4.30, absorbed dose due to patient-scattered radiation was calculated as

$$D_{\text{PS}}(x, y, z) = \Psi_{\text{PS}}(x, y, z) \times \left(\frac{\mu_{\text{en}}}{\rho} \right)_{\bar{E}_3(x,y,z)} \quad (4.55)$$

where $\Psi_{\text{PS}}(x, y, z)$ is as defined in Equation 4.43. Plugging Equations 4.30, 4.42 and 4.55 into Equation 4.5 yields the total absorbed dose at the point of calculation, (x, y, z) .

4.3. Results

4.3.1. Monte Carlo Simulations

The suite of irradiation conditions of the Monte Carlo simulations is detailed in Table 4.2. Figure 4.7 plots the source energy fluence for the “open field” simulation condition with all collimators, head-shielding, water, and plastic phantom walls replaced by air. The tallies of photon energy fluence in the water phantom with all collimators present were binned by the cell in which the photons were created. Figure 4.8 shows the simulated

Table 4.2. Conditions for all Monte Carlo simulations performed as part of this work. Open-field refers to simulations in which all beam-limiting devices have been replaced by air for the purpose of investigating the uncollimated source fluence.

Phantom	Field Size (cm ²)	Voxel Size (cm ³)	x range (cm)	y range (cm)	z range (cm)
	Open	0.125	-50 → 50	-50 → 50	50
In-Air	”	1	0 → 40	0 → 40	91.5 → 130.5
	10 × 10	”	”	”	”
In-Water	2 × 2	1	0 → 40	0 → 40	91.5 → 130.5
	5 × 5	”	”	”	”
	10 × 10	”	”	”	”
	14 × 14	”	”	”	”
	20 × 20	”	”	”	”
	5 × 20	”	”	”	”
	20 × 5	”	”	”	”

Table 4.3. Empirical parameter values for parameterizations average photon energy.

Parameter	Uncollided	Head-Scattered	Patient-Scattered
n (N/A)	1	2	3
$a_{\bar{E},n}$ (MeV cm ⁻¹)	2.58×10^{-2}	1.44×10^{-2}	9.70×10^{-3}
$b_{\bar{E},n}$ (MeV)	-3.98×10^{-1}	2.46×10^{-2}	-4.25×10^{-1}
$c_{\bar{E},n}$ (cm ⁻²)	2.19×10^{-4}	-4.23×10^{-4}	-1.27×10^{-4}
$d_{\bar{E},n}$ (cm ⁻¹)	-5.83×10^{-2}	7.75×10^{-2}	3.04×10^{-2}
$e_{\bar{E},n}$ (N/A)	4.06×10^0	-2.90×10^0	-1.05×10^0
f_n ”	1.00×10^0	1.74×10^0	6.82×10^{-1}
$\sigma_{0,n}$ ”	2.00×10^{-1}	2.00×10^{-1}	2.00×10^{-1}

total and component fluences at z_{iso} (depth of 10 cm in the water phantom) for a 6-MV, 10×10-cm² field. Finally, Figure 4.9 plots the mean photon energy from all components of photon energy fluence for the 6-MV, 10×10-cm² field. Values of the empirical fitting parameters from 4.2–4.4 are listed in Table 4.3.

4.3.2. Analytical Model

4.3.2.1. Photon Source Model

The photon source in-air model parameters are listed in Table 4.6. The model achieved good agreement with the Monte Carlo simulation of uncollimated source energy fluence. Quantitatively comparing the uncollimated source model to the simulations, the

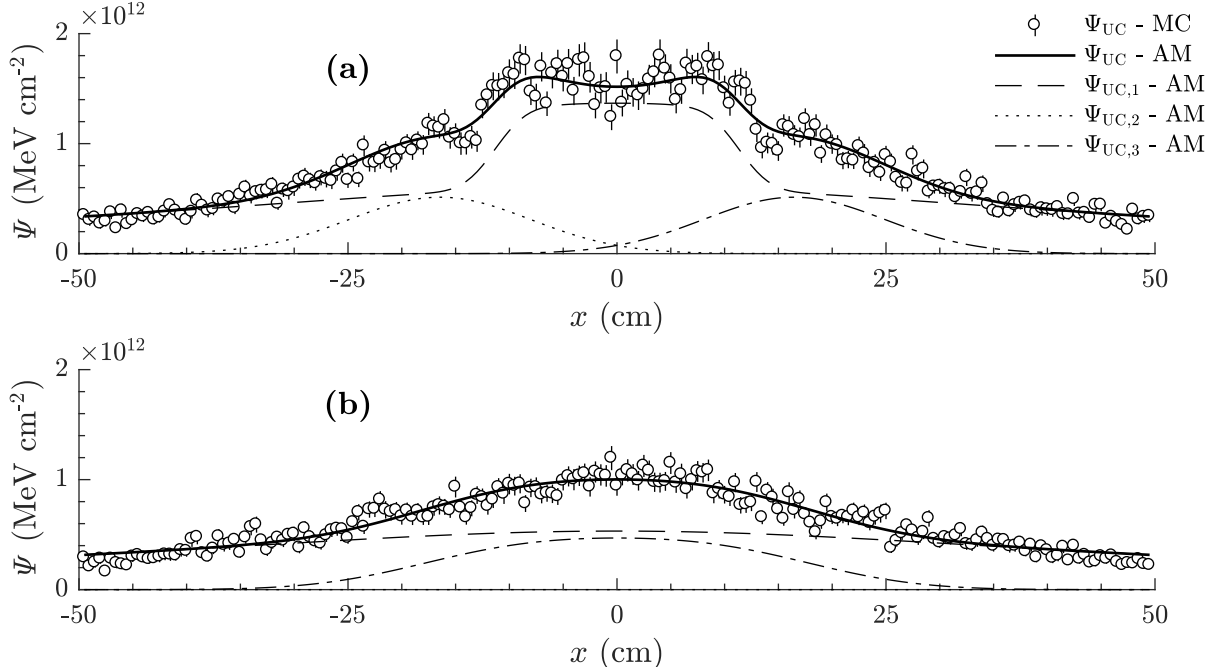


Figure 4.7. Circles represent Monte Carlo simulations of energy fluence from the uncollimated photon source. The values are normalized to the number of electrons-on-target necessary to deliver a dose of 1 Gy at d_{\max} . Lines represent the total analytical model of uncollimated energy fluence and the individual components from the central and lateral source terms.

mean unsigned local relative error, $_{\text{US}}\overline{\Delta\Psi}_{\text{rel}}$, is 9.9%. The mean signed local relative error, $_{\text{S}}\overline{\Delta\Psi}_{\text{rel}}$, is -0.4%, indicating vanishingly small systematic error. Plots of the uncollimated source energy fluence, including both the Monte Carlo simulations and analytical model calculations, are shown in Figure 4.7. Excellent agreement can be seen along the cardinal x - and y -axes and in profiles parallel to the axes shifted 20 cm from isocenter.

4.3.2.2. Model of Energy Fluence in a Water-Box

The model of head-scattered radiation in a water-box phantom achieved similarly good agreement. Figure 4.10 plots head-scattered energy fluence for a $10\times 10\text{-cm}^2$ field from Monte Carlo simulations and from the analytical model, revealing excellent agreement in the x - and y -directions and along the diagonal.

Figure 4.11 shows the Monte Carlo simulated and analytical model calculated patient-scattered energy fluence for the $10\times 10\text{-cm}^2$ field-size at a depth of 5 cm in water. The dashed and dotted lines represent components of the patient-scattered energy fluence model

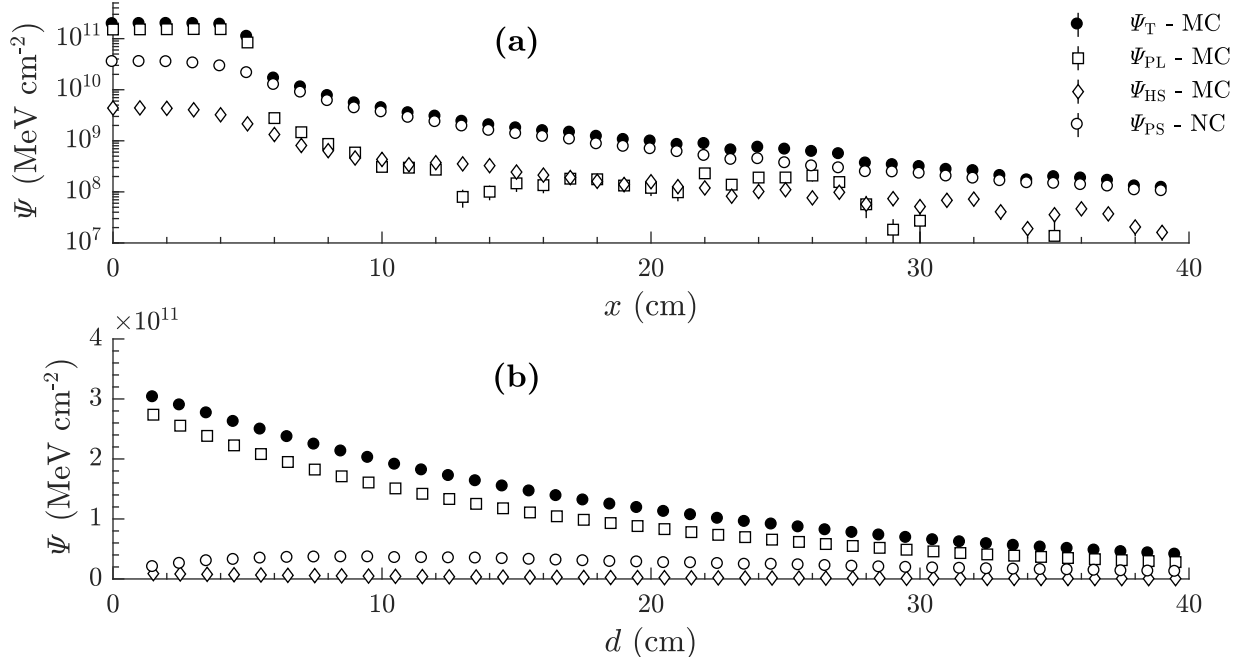


Figure 4.8. Results of Monte Carlo simulation of a $10 \times 10\text{-cm}^2$ collimated photon beam incident on large water-box phantom, including all components of photon energy fluence. The values are normalized to the number of electrons-on-target necessary to deliver a dose of 1 Gy at d_{\max} . Profiles (a) and (b) are at 10 cm depth in water along the x - and y -axes, respectively. Profile (c) is also at a depth of 10 cm and plots along the line $x = y$. Plot (d) shows energy fluence *versus* depth along the beam's central-axis.

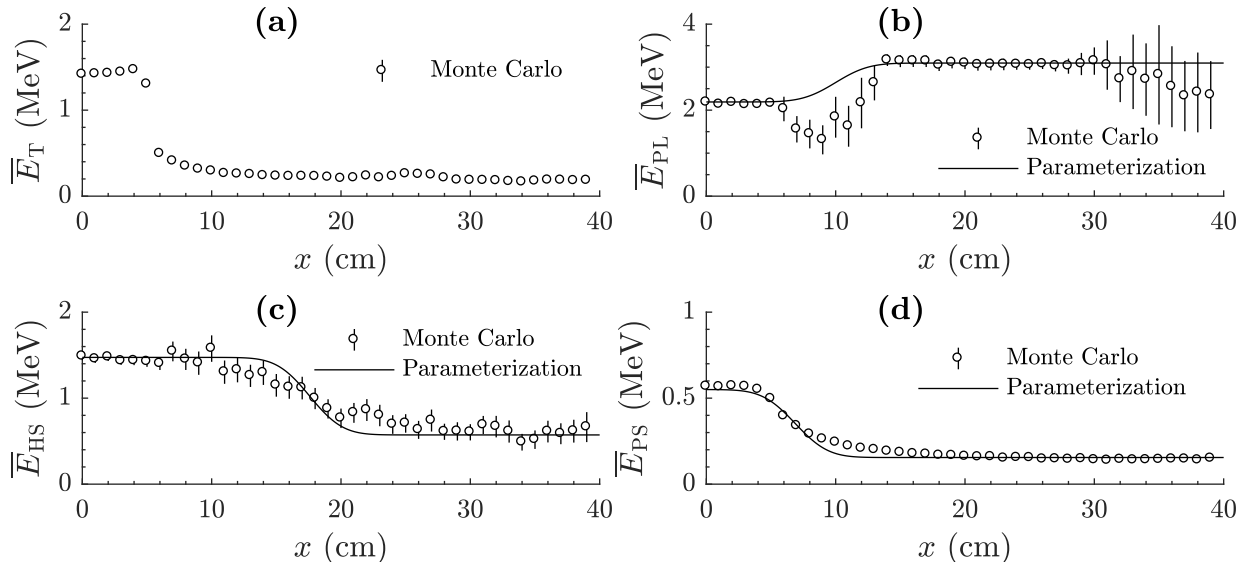


Figure 4.9. Mean photon energy *versus* distance from photon-beam central axis at 10-cm depth in water from a 6-MV, $10 \times 10\text{-cm}^2$ field. Plots include the mean energy of (a) all photons, (b) primary and leakage photons, (c) head-scattered photons, and (d) patient-scattered photons. The solid curves in plots (b)–(d) represent the parameterizations of mean photon energy defined in 4.1–4.4.

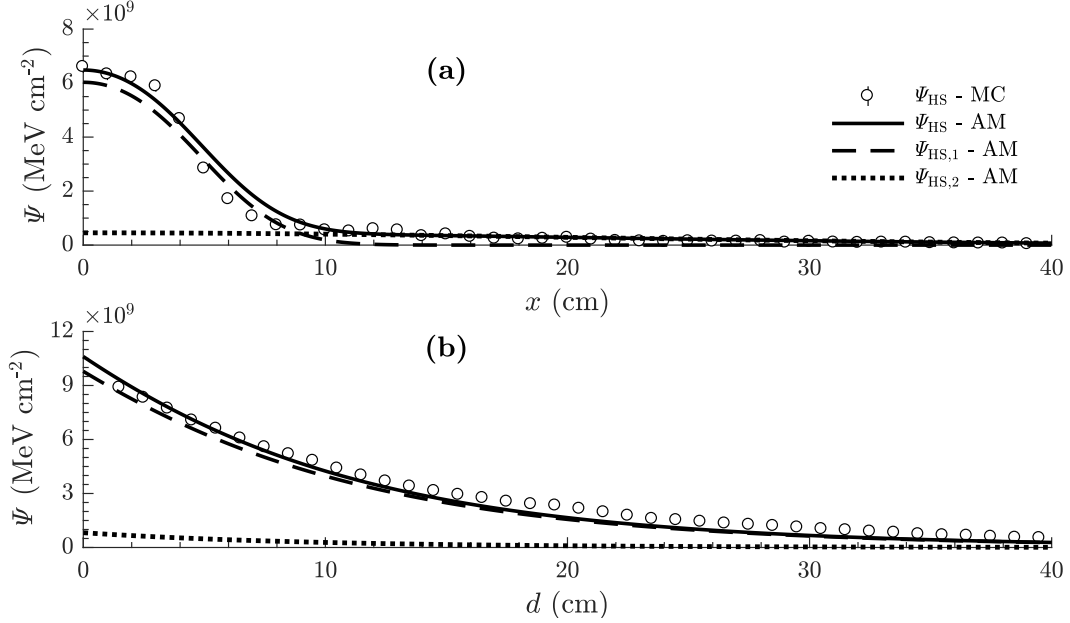


Figure 4.10. Monte Carlo simulated and analytical model calculated head-scattered energy fluence for the 10×10 -cm² field-size at a depth of 5 cm in water. The values are normalized to the number of electrons-on-target necessary to deliver a dose of 1 Gy at d_{max} .

as given in Equations 4.50 and 4.54, respectively. As in the case of head-scattered radiation, the top plots in the figure demonstrate agreement in the x - and y -directions. The bottom right plot reveals good agreement with depth in water including in the build-up region where Equation 4.45 models the increase of patient-scattered energy fluence with depth.

The model of total energy fluence in water agreed well with the Monte Carlo simulations. The mean of the unsigned local percent error for all field-sizes and locations was 10.3%. Figure 4.12 shows a diagonal profile including the Monte Carlo simulated and analytical model calculated values of energy fluence for all components.

4.3.2.3. Model of Absorbed Dose

All model fitting parameters are listed in Table 4.6. The model of absorbed dose agreed well with the Monte Carlo simulations. The signed and unsigned average percent differences were -3.0% and 15.9%, respectively, for all points and field-sizes considered. The extended gamma index analysis with criteria of 3-mm distance-to-agreement, 3% relative dose difference in-field, and 3-mGy/Gy absolute dose difference out-of-field resulted in 92.1%

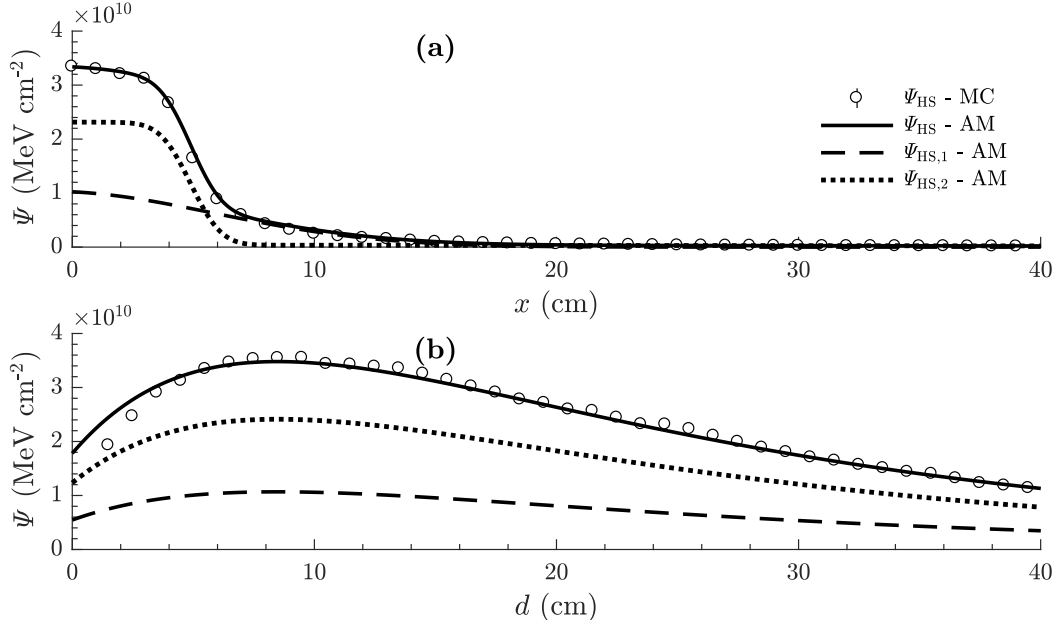


Figure 4.11. Monte Carlo simulated and analytical model calculated patient-scattered energy fluence for the 10×10 -cm² field-size at a depth of 5 cm in water. The values are normalized to the number of electrons-on-target necessary to deliver a dose of 1 Gy at d_{\max} .

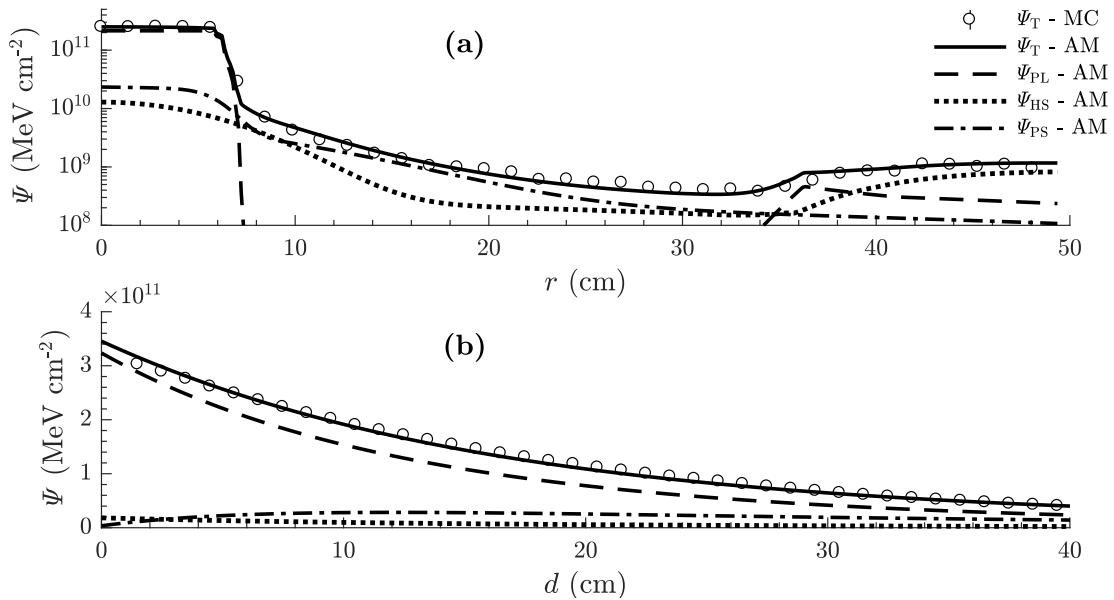


Figure 4.12. Monte Carlo simulation (points) and analytical model calculated (lines) photon energy fluence, including all components, for the case of a 6-MV, 10×10 -cm² field at a depth of 5 cm in water. The values are normalized to the number of electrons-on-target necessary to deliver a dose of 1 Gy at d_{\max} .

Table 4.4. Gamma index passing rates of the analytical model compared with the training data-set (Monte Carlo). The distance-to-agreement criterion is 3 mm.

ΔD_A (mGy)	ΔD_R (%)				
	1.0%	3.0%	5.0%	7.5%	10.0%
0.5	60.6%	71.2%	74.1%	75.1%	75.4%
1.0	73.5%	84.1%	87.1%	88.0%	88.4%
3.0	81.5%	92.1%	95.1%	96.0%	96.4%
5.0	83.0%	93.6%	96.5%	97.5%	97.8%
10.0	83.8%	94.4%	97.4%	98.3%	98.6%

Table 4.5. Gamma index passing rates of the analytical model compared with the validation data-set (measurements). The distance-to-agreement criterion is 3 mm.

ΔD_A (mGy)	ΔD_R (%)				
	1.0%	3.0%	5.0%	7.5%	10.0%
0.5	51.3%	53.6%	55.1%	55.4%	55.5%
1.0	68.5%	70.6%	72.1%	72.4%	72.5%
3.0	85.6%	87.8%	89.3%	89.6%	89.7%
5.0	90.7%	92.9%	94.4%	94.7%	94.8%
10.0	92.1%	94.3%	95.7%	96.0%	96.1%

of points passing. The gamma-index passing rates for various criteria are shown in Table 4.4 for all field-sizes and locations. The average wall clock time necessary for the model to calculate dose to 1 million points was 3 minutes and 19 seconds.

The model also achieved good agreement with measurements (*i.e.*, the validation data-set). The extended gamma-index analysis of Wilson et al. [45] with criteria of 3-mm distance-to-agreement, 3% relative dose difference in-field, and 3-mGy/Gy absolute dose difference out-of-field resulted in 89.3% of points passing. The gamma-index passing rates of the model compared with the validation data-set for various criteria are shown in Table 4.5.

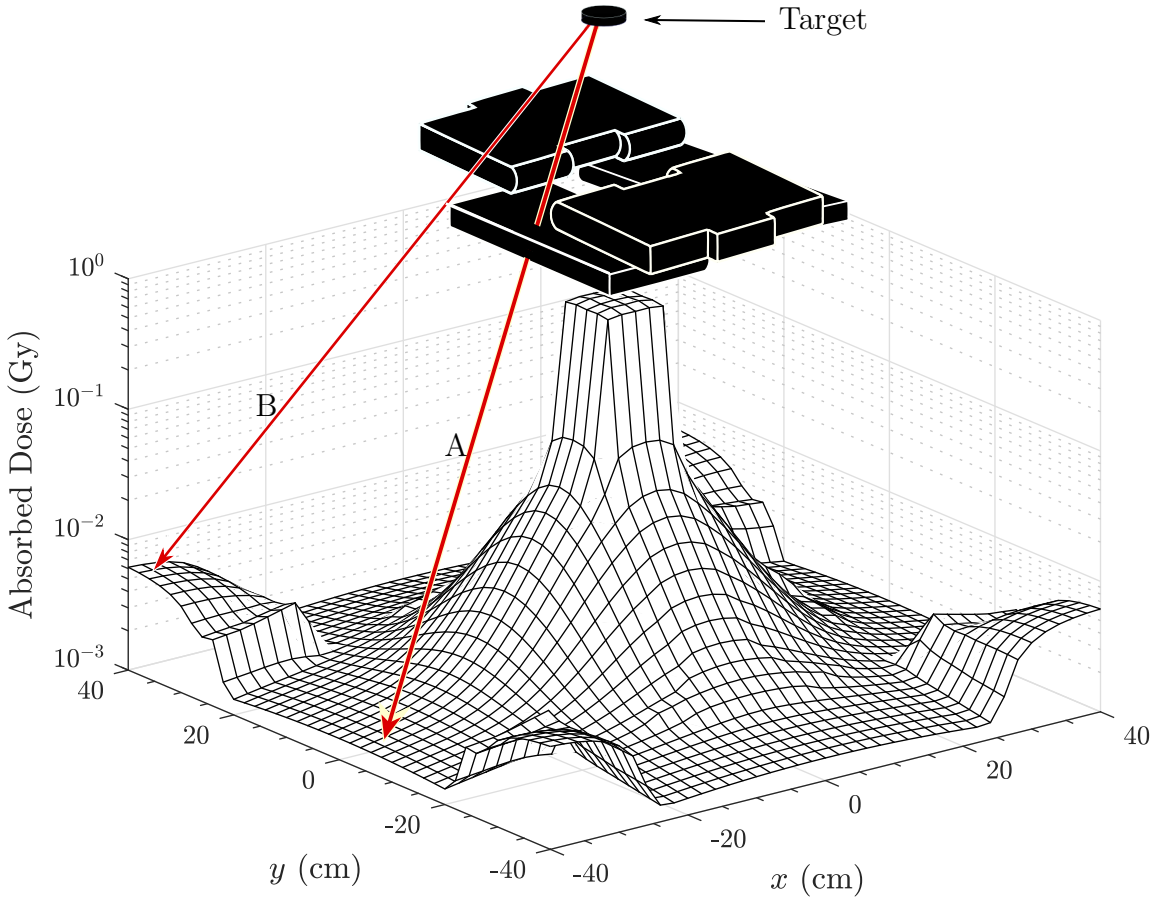


Figure 4.13. 2-dimensional plot of the absorbed dose for a 6-MV $10 \times 10 \text{ cm}^2$ field at a depth of 10 cm in water as calculated by the analytical model. An illustration of the secondary collimator positioning for a square field has been superimposed above the plot. Ray A illustrates an example path of a leakage photon that passes through the jaws. Ray B illustrates an example path of a leakage photon that does not intersect the secondary collimators.

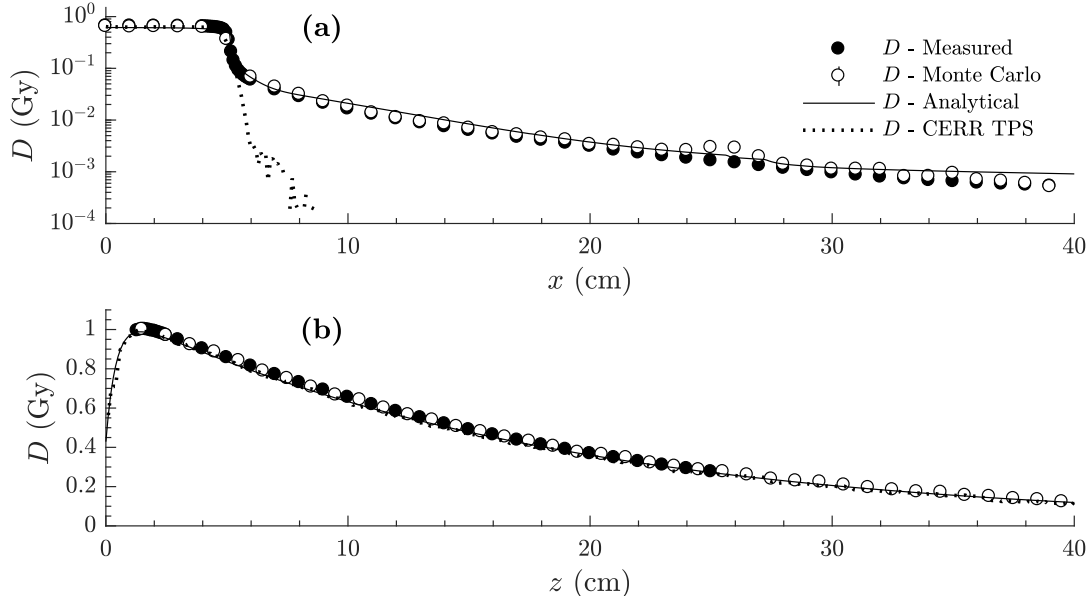


Figure 4.14. Absorbed dose to the water-box phantom for case of a 10×10 -cm² field. Closed circles represent measurements, open circles represent Monte Carlo simulated values, the solid line represents the analytical model, and the dotted line represents the dose as calculated by the Computational Environment for Radiotherapy Research (CERR) TPS [46]. Subplot (a) is a profile at 10-cm depth along the x -axis. Subplot (b) shows dose *versus* depth along the photon-beam's central axis. The dose values are normalized to 1 Gy at d_{\max} .

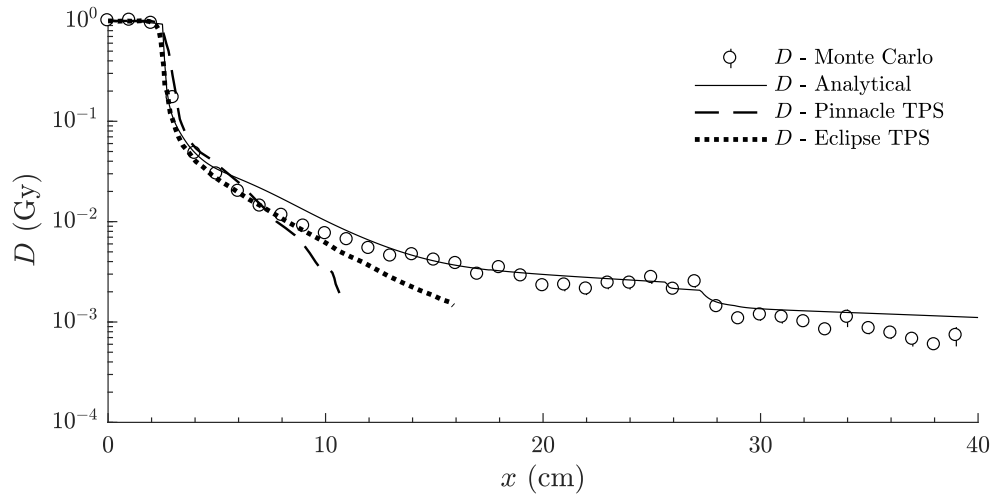


Figure 4.15. Absorbed dose to the water-box phantom for case of a 5×5 -cm² field at a depth of 10 cm. Circles represent Monte Carlo simulated values, the solid line represents the analytical model calculations, and the dashed and dotted lines represent the Pinnacle (Philips Healthcare, Andover, MA) and Eclipse (Varian Medical Systems, Inc., Palo Alto, CA) TPS calculated doses, respectively.

Table 4.6. Parameter values for analytical model of absorbed dose.

Symbol	Description	Value	Units
Uncollimated Photon Source In-Air Model Parameters			
Q_1	Electron charge in central source term	2.25×10^{-2}	C
Q_2	Electron charge in each lateral source term	1.93×10^{-2}	"
$\sigma_{1,0}$	Central source term width parameter	4.37×10^{-2}	cm
$\sigma_{2,0}$	Lateral source terms width parameter	1.88×10^{-1}	"
$\bar{\rho}_{2,0}$	Lateral source Gaussian centroid displacement	2.05×10^{-1}	"
α_{G_1}	Flattening filter build-up parameter	5.58×10^{-1}	N/A
p	Falloff parameter	1.88×10^0	"
Primary and Leakage Dose Model Parameters			
$a_{\mu,PC,1}$	Empirical adjustment to PC attenuation for central source term	5.56×10^{-1}	N/A
$a_{\mu,PC,2}$	Empirical adjustment to PC attenuation for lateral source term	1.13×10^0	"
$a_{\mu,Jaw,1}$	Empirical adjustment to jaw attenuation for central source term	6.48×10^0	"
$a_{\mu,Jaw,2}$	Empirical adjustment to jaw attenuation for lateral source term	8.35×10^0	"
$a_{\mu,MLC,1}$	Empirical adjustment to MLC attenuation for central source term	1.11×10^0	"
$a_{\mu,MLC,2}$	Empirical adjustment to MLC attenuation for lateral source term	1.40×10^0	"
$a_{\mu,1}$	Empirical adjustment to water attenuation for central source term	8.36×10^{-1}	"
$a_{\mu,2}$	Empirical adjustment to water attenuation for lateral source term	8.98×10^{-1}	"
Head-Scatter Dose Model Parameters			
$\kappa_{HS,1}$	First head-scatter term constant of proportionality	1.93×10^{10}	N/A
$p_{HS,1}$	First head-scatter term field-size exponent	3.94×10^{-2}	"
$\sigma_{HS,x,1}^{iso}$	First head-scatter term width parameter at isocenter	8.82×10^{-1}	cm
$m_{x,1}$	First head-scatter term width parameter correction to geometric magnification	4.50×10^{-1}	N/A

(table cont'd.)

Symbol	Description	Value	Units
Head-Scatter Dose Model Parameters (Continued)			
$\kappa_{\text{HS},2}$	Second head-scatter term constant of proportionality	3.27×10^8	"
$p_{\text{HS},2}$	Second head-scatter term field-size exponent	7.77×10^{-2}	"
$\sigma_{\text{HS},x,2}^{\text{iso}}$	Second head-scatter term x -width parameter at isocenter	4.24×10^0	cm
$m_{x,2}$	Second head-scatter term x -width parameter correction to geometric magnification	6.43×10^0	N/A
$\sigma_{\text{HS},y,2}^{\text{iso}}$	Second head-scatter term y -width parameter at isocenter	2.48×10^0	cm
$m_{y,2}$	Second head-scatter term y -width parameter correction to geometric magnification	9.92×10^0	N/A
$\alpha_{\mu,\text{HS}}$	Empirical adjustment factor for head-scatter attenuation in water	1.19×10^{-1}	"
$\beta_{\mu,\text{HS}}$	Empirical adjustment factor for head-scatter attenuation in water	3.15×10^0	"
q_{HS}	Head-scatter gap factor coefficient	3.02×10^{-2}	"
Patient-Scatter Dose Model Parameters			
κ_{PS}	Patient-scatter constant of proportionality	6.30×10^{10}	N/A
p_{PS}	Patient-scatter field-size exponent	4.25×10^{-1}	"
α_{B}	Patient-scatter buildup factor coefficient	2.21×10^{-2}	"
z_{B}	Patient-scatter buildup factor shift	2.90×10^0	cm
$\alpha_{\sigma,\text{PS},1}$	1 st order coefficient for first patient scatter term width parameter	9.50×10^{-1}	
$\beta_{\sigma,\text{PS},1}$	0 th order coefficient for first patient scatter term width parameter	4.10×10^{-8}	
$k_{\text{PS},1}$	First patient-scatter term width parameter correction to geometric magnification	6.19×10^{-2}	N/A
c_{PS}	Patient-scatter central-axis apportionment constant	2.19×10^{-1}	N/A
$\alpha_{\sigma,\text{PS},2}$	1 st order coefficient for second patient scatter term width parameter	1.63×10^3	
$\beta_{\sigma,\text{PS},2}$	0 th order coefficient for second patient scatter term width parameter	6.18×10^{-2}	
$k_{\text{PS}2}$	Second patient-scatter term width parameter correction to geometric magnification	4.36×10^1	N/A
$\alpha_{q,\text{PS}}$	1 st order coefficient for patient-scatter gap factor constant of proportionality	6.79×10^{-1}	"
$\beta_{q,\text{PS}}$	0 th order coefficient for patient-scatter gap factor constant of proportionality	1.78×10^1	"
$\alpha_{\mu,\text{PS}}$	1 st order empirical adjustment factor for patient-scatter attenuation in water	1.06×10^0	"
$\beta_{\mu,\text{PS}}$	0 th order empirical adjustment factor for patient-scatter attenuation in water	8.60×10^{-4}	"
$\alpha_{\text{PC,PS}}$	Empirical adjustment factor to primary collimator impact on patient-scatter.	1.25×10^0	
$\alpha_{\text{col,PS}}$	Empirical adjustment factor to secondary collimator impact on patient-scatter.	7.40×10^{-1}	

4.4. Discussion

In this work, we developed an analytical model of absorbed dose and photon energy fluence from primary, leakage, head-scattered, and patient-scattered radiation for 6-MV X-ray beams. The model realistically calculates transmission through circular MLC leaf tips and through regions where secondary collimators may overlap or be absent. The major finding of this work is that it is possible to quickly and accurately calculate the absorbed dose to arbitrary points in a 3-dimensional phantom from 6-MV photon fields using a physics based analytical model.

Unlike previous models of this type, this work explicitly models the variation in absorbed dose both on and off the cardinal axes. Many previous models neglected locations falling outside of the in- or cross-planes or modeled collimators as semi-infinite planes. By realistically modeling the 3-dimensional extent of all beam-limiting devices, this work accounts for the variations in fluence that occur due to the overlapping and absence of secondary collimators. This increases the domain of applicability of the model and is necessary if one wishes to accurately calculate out-of-field exposures.

One major strength of this work is the inclusion of a large amount of high-quality measured data. The measurements were conducted at, and the equipment calibrated by, a renowned German national standards laboratory. This lends significant confidence to their accuracy. Another strength is the inclusion of tagged Monte Carlo tallies of each component of energy fluence and dose (*i.e.*, primary, leakage, head-scattered and patient-scattered radiation). Jagetic and Newhauser [17] listed uncertainty in the accuracy of the leakage, head-scatter, and patient-scatter models as a weakness of that work. By verifying the accuracy of each model component by comparison with Monte Carlo simulations, this work overcomes that obstacle.

Limitations of this work include the focus on a single model of linear accelerator. However, this is not a serious limitation because the physics-based nature of the model should allow users to simply modify the model's configuration to reflect the dimensions of

the collimators to match those used in their clinic and train the model on a limited set of measurements. Access to proprietary information is not required. Another limitation of this work is the focus on a single photon beam energy. Since 6-MV beams are used in the majority of treatments, this is not a serious limitation.

Future work related to this project should include expanding the model to the full suite of clinical beam energies. A detailed, component based model of stray absorbed-dose necessitates the inclusion of a model of photoneutron absorbed dose. Such work is currently ongoing in our laboratory. Additionally, the integration of the model into a commercial or research treatment planning system to test the feasibility of including whole body absorbed dose calculations into the clinical workflow would be useful to demonstrate feasibility and utility in a clinical setting

4.5. References

- ¹G. T. Armstrong, M. Stovall, and L. L. Robison, “Long-term effects of radiation exposure among adult survivors of childhood cancer: results from the childhood cancer survivor study”, *Radiat Res* **174**, 840–50 (2010).
- ²W. D. Newhauser and M. Durante, “Assessing the risk of second malignancies after modern radiotherapy”, *Nat Rev Cancer* **11**, 438–48 (2011).
- ³T. M. Okwuosa, S. Anzevino, and R. Rao, “Cardiovascular disease in cancer survivors.”, *Postgrad Med J* **93**, 82–90 (2017).
- ⁴J. P. Williams and W. Newhauser, “Normal tissue damage: its importance, history and challenges for the future.”, *Br J Radiol*, 20180048 (2018).
- ⁵NCRP, *NCRP Report No. 170 - Primary cancers and cardiovascular disease after radiation therapy* (National Council on Radiation Protection and Measurements, Bethesda, MD, 2011).
- ⁶I. Diallo, N. Haddy, E. Adjadj, A. Samand, E. Quiniou, J. Chavaudra, I. Alziar, N. Perret, S. Guerin, D. Lefkopoulos, and F. de Vathaire, “Frequency distribution of second solid cancer locations in relation to the irradiated volume among 115 patients treated for childhood cancer”, *Int J Radiat Oncol Biol Phys* **74**, 876–83 (2009).
- ⁷D. Smart, *Physician characteristics and distribution in the U.S.* (American Medical Association, Chicago, IL, 2009).

- ⁸K. E. Henson, P. McGale, C. Taylor, and S. C. Darby, “Radiation-related mortality from heart disease and lung cancer more than 20 years after radiotherapy for breast cancer”, *Br J Cancer* **108**, 179–82 (2013).
- ⁹K. D. Miller, R. L. Siegel, C. C. Lin, A. B. Mariotto, J. L. Kramer, J. H. Rowland, K. D. Stein, R. Alteri, and A. Jemal, “Cancer treatment and survivorship statistics, 2016”, *CA Cancer J Clin* **66**, 271–89 (2016).
- ¹⁰ACS, *Cancer treatment & survivorship facts & figures 2016-2017* (American Cancer Society, Atlanta, 2016).
- ¹¹NCRP, *Ncrp report no. 181 - evaluation of the relative effectiveness of low-energy photons and electrons in inducing cancer in humans* (National Council on Radiation Protection and Measurements, Bethesda, MD, 2018).
- ¹²W. D. Newhauser, C. Schneider, L. Wilson, S. Shrestha, and W. Donahue, “A review of analytical models of stray radiation exposures from photon- and proton-beam radiotherapies”, *Radiat Prot Dosimetry* **180**, 245–251 (2018).
- ¹³R. M. Howell, S. B. Scarborough, S. F. Kry, and D. Z. Yaldo, “Accuracy of out-of-field dose calculations by a commercial treatment planning system”, *Phys Med Biol* **55**, 6999–7008 (2010).
- ¹⁴M. L. Taylor and T. Kron, “Consideration of the radiation dose delivered away from the treatment field to patients in radiotherapy”, *J Med Phys* **36**, 59–71 (2011).
- ¹⁵A. Joosten, O. Matzinger, W. Jeanneret-Sozzi, F. Bochud, and R. Moeckli, “Evaluation of organ-specific peripheral doses after 2-dimensional, 3-dimensional and hybrid intensity modulated radiation therapy for breast cancer based on monte carlo and convolution/superposition algorithms: implications for secondary cancer risk assessment”, *Radiother Oncol* **106**, 33–41 (2013).
- ¹⁶U. Schneider, R. A. Halg, M. Hartmann, A. Mack, F. Storelli, A. Joosten, R. Mockli, and J. Besserer, “Accuracy of out-of-field dose calculation of tomotherapy and cyberknife treatment planning systems: a dosimetric study”, *Z Med Phys* **24**, 211–5 (2014).
- ¹⁷L. J. Jagetic and W. D. Newhauser, “A simple and fast physics-based analytical method to calculate therapeutic and stray doses from external beam, megavoltage x-ray therapy”, *Phys Med Biol* **60**, 4753–75 (2015).
- ¹⁸M. T. Bahreyni Toossi, B. Farhood, and S. Soleymanifard, “Evaluation of dose calculations accuracy of a commercial treatment planning system for the head and neck region in radiotherapy”, *Rep Pract Oncol Radiother* **22**, 420–427 (2017).
- ¹⁹R. Harrison, “Introduction to dosimetry and risk estimation of second cancer following radiotherapy”, *Radiat Meas* **57**, 1–8 (2013).

- ²⁰K. R. Kase, G. K. Svensson, A. B. Wolbarst, and M. A. Marks, “Measurements of dose from secondary radiation outside a treatment field”, *Int J Radiat Oncol Biol Phys* **9**, 1177–83 (1983).
- ²¹M. Stovall, C. R. Blackwell, J. Cundiff, D. H. Novack, J. R. Palta, L. K. Wagner, E. W. Webster, and R. J. Shalek, “Fetal dose from radiotherapy with photon beams: report of AAPM radiation therapy committee Task Group No. 36”, *Med Phys* **22**, 63–82 (1995).
- ²²R. Kaderka, D. Schardt, M. Durante, T. Berger, U. Ramm, J. Licher, and C. La Tessa, “Out-of-field dose measurements in a water phantom using different radiotherapy modalities”, *Phys Med Biol* **57**, 5059–74 (2012).
- ²³S. F. Kry, U. Titt, F. Ponisch, D. Followill, O. N. Vassiliev, R. A. White, R. Mohan, and M. Salehpour, “A Monte Carlo model for calculating out-of-field dose from a Varian 6 MV beam”, *Med Phys* **33**, 4405–13 (2006).
- ²⁴B. S. Athar and H. Paganetti, “Comparison of second cancer risk due to out-of-field doses from 6-MV IMRT and proton therapy based on 6 pediatric patient treatment plans”, *Radiother Oncol* **98**, 87–92 (2011).
- ²⁵S. S. Almberg, J. Frengen, and T. Lindmo, “Monte Carlo study of in-field and out-of-field dose distributions from a linear accelerator operating with and without a flattening-filter”, *Med Phys* **39**, 5194–203 (2012).
- ²⁶N. Chofor, D. Harder, K. C. Willborn, and B. Poppe, “Internal scatter, the unavoidable major component of the peripheral dose in photon-beam radiotherapy”, *Phys Med Biol* **57**, 1733–43 (2012).
- ²⁷J. A. Kalapurakal, M. Gopalakrishnan, M. Mille, I. Helenowski, S. Peterson, C. K. Rigsby, F. Laurie, J. W. Jung, T. J. Fitzgerald, and C. Lee, “Feasibility and accuracy of UF/NCI phantoms and Monte Carlo retrospective dosimetry in children treated on National Wilms Tumor Study protocols”, *Pediatr Blood Cancer* **65** (2018) 10.1002/pbc.27395.
- ²⁸P. H. van der Giessen, “Peridose, a software program to calculate the dose outside the primary beam in radiation therapy”, *Radiother Oncol* **58**, 209–13 (2001).
- ²⁹M. Stovall, R. Weathers, C. Kasper, S. A. Smith, L. Travis, E. Ron, and R. Kleinerman, “Dose reconstruction for therapeutic and diagnostic radiation exposures: use in epidemiological studies”, *Radiat Res* **166**, 141–57 (2006).
- ³⁰P. J. Taddei, W. Jalbout, R. M. Howell, N. Khater, F. Geara, K. Homann, and W. D. Newhauser, “Analytical model for out-of-field dose in photon craniospinal irradiation”, *Phys Med Biol* **58**, 7463–79 (2013).

- ³¹B. Sánchez-Nieto, R. El-far, L. Irazola, M. Romero-Expósito, J. I. Lagares, J. C. Mateo, J. A. Terrón, and F. Sánchez Doblado, “Analytical model for photon peripheral dose estimation in radiotherapy treatments”, *Biomed Phys Eng Express* **1**, 045205 (2015).
- ³²P. Hauri, R. A. Halg, J. Besserer, and U. Schneider, “A general model for stray dose calculation of static and intensity-modulated photon radiation”, *Med Phys* **43**, 1955 (2016).
- ³³C. W. Schneider, W. D. Newhauser, L. J. Wilson, U. Schneider, R. Kaderka, S. Miljanic, Z. Knezevic, L. Stolarczyk, M. Durante, and R. M. Harrison, “A descriptive and broadly applicable model of therapeutic and stray absorbed dose from 6 to 25 MV photon beams”, *Med Phys* **44**, 3805–3814 (2017).
- ³⁴PTW, *Detectors including codes of practice*, http://www.ptw.de/fileadmin/data/download/catalogviewer/DETECTORS_Cat_en_16522900_11/blaetterkatalog/index.html, 2018.
- ³⁵N. Chofor, D. Harder, and B. Poppe, “Non-reference condition correction factor k_{NR} of typical radiation detectors applied for the dosimetry of high-energy photon fields in radiotherapy”, *Z Med Phys* **22**, 181–96 (2012).
- ³⁶N. Chofor, D. Harder, and B. Poppe, “Supplementary values of the dosimetric parameters k_{NR} and E_m for various types of detectors in 6 and 15 MV photon fields”, *Z Med Phys* **24**, 27–37 (2014).
- ³⁷A. Schüller, S. Pajtinger, M. Meier, C. Makowski, and R. P. Kapsch, “The metrological electron accelerator facility (MELAF) for research in dosimetry for radiotherapy”, in *World congress on medical physics and biomedical engineering 2018*, Vol. 68/3, edited by L. Lhotska, L. Sukupova, I. Lacković, and G. Ibbott, IFMBE Proceedings (2019), pp. 589–593.
- ³⁸R. P. Kapsch and A. Krauss, “On the performance of monitor chambers to measure the output of medical linear accelerators for high-precision dosimetric investigations”, in *World congress on medical physics and biomedical engineering, september 7 - 12, 2009, Munich, Germany*, edited by O. Dössel and W. C. Schlegel (2009), pp. 85–88.
- ³⁹D. B. Pelowitz, *MCNPX user’s manual version 2.7.0* (Los Alamos, NM, 2011).
- ⁴⁰Elekta, *Information for Monte Carlo modeling of the Elekta linear accelerator, Personal communication*, Nov. 2018.
- ⁴¹F. H. Attix, *Introduction to radiological physics and radiation dosimetry* (Wiley-VCH, Weinheim, Germany, 1986).
- ⁴²J. F. Sutcliffe, “A simplified model of radiation attenuation and energy absorption coefficients of the elements”, *Appl Radiat Isot* **105**, 188–197 (2015).

- ⁴³A. L. Boyer and S. Li, “Geometric analysis of light-field position of a multileaf collimator with curved ends”, *Med Phys* **24**, 757–62 (1997).
- ⁴⁴F. M. Khan, *The physics of radiation therapy*, Fourth (Lippincott Williams and Williams, 2009).
- ⁴⁵L. J. Wilson, W. D. Newhauser, and C. W. Schneider, “An objective method to evaluate radiation dose distributions varying by three orders of magnitude”, *Med Phys* **46**, 1888–1895 (2019).
- ⁴⁶J. O. Deasy, A. I. Blanco, and V. H. Clark, “CERR: A computational environment for radiotherapy research”, *Med Phys* **30**, 979–85 (2003).

Chapter 5.

Photoneutron Fluence and Absorbed Dose from 25-MV External Beam X-Ray Radiotherapy

5.1. Introduction

Neutron contamination is an important component of stray radiation produced by external beam x-ray treatment units [1, 2]. The main source of neutrons is photoneutron production induced by photons impinging on high-atomic-number materials in the treatment unit, such as lead and tungsten. Neutron contamination increases strongly with photon energy, becoming important at photon beam energies greater than 10 MV. The absorbed dose (D_n) to the patient from neutrons is low in comparison with the maximum therapeutic absorbed dose from the primary field, but the radiation weighting factors for neutrons are large and vary strongly with energy ($2 \leq w_R \leq 20$), and so the neutron contribution to equivalent dose (H_n) can be considerable [3, 4]. In spite of this, photoneutron exposures are neglected by clinical treatment planning systems. The use of high energy beams in x-ray radiation therapy has increased in recent years due to advantages, such as greater therapeutic photon dose at depth, reduced photon skin dose, and reduced penumbral dose due to decreased photon scatter [5, 6], and so the characterization of neutron exposures is necessary.

Photoneutrons in x-ray radiotherapy are produced primarily through the giant dipole resonance. Figure 5.1 shows a typical photoneutron spectrum from a 25-MV x-ray beam at isocenter in air. This illustrates the importance of neutrons produced by evaporation processes, with a spectral peak between 0.1 and 1 MeV. If water or tissue is present, this results in a spectrum of neutron energies with three distinct regions, as shown in Figure 5.2. In Chapter 2, we reported a physics-based analytical model of external neutron contamination for passively-scattered proton therapy that was based on four neutron energy regimes, including thermal, $1/E$ (or epithermal), evaporation, and intranuclear cascade neutrons [7, 8].

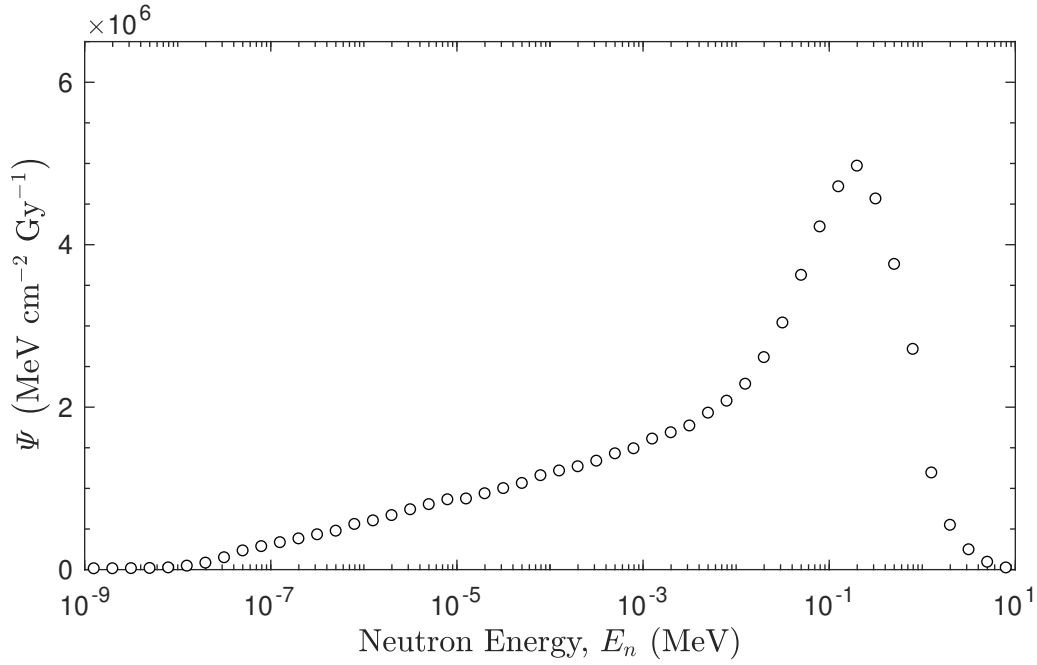


Figure 5.1. Typical photoneutron energy spectrum, Ψ , at isocenter for a 25-MV beam in air.

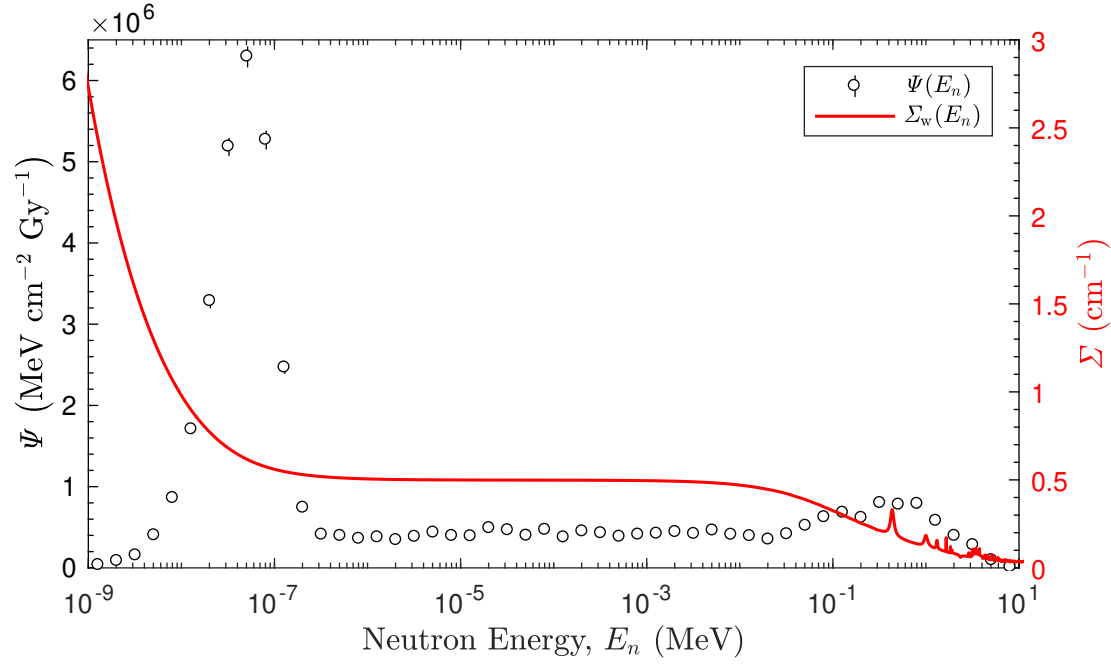


Figure 5.2. Typical photoneutron energy fluence spectrum, Ψ , at $d = 10$ cm in water for a 25-MV beam with a source-to-surface distance (SSD) of 90 cm. The small peak located around 1 MeV is due to evaporation neutrons. The tall peak centered between 10^{-8} and 10^{-7} MeV is due to thermal neutrons. Neutrons in the broad continuum between these peaks are known as $1/E$, or epithermal, neutrons. The axis at right shows the neutron macroscopic cross section in water, Σ_w , over the same energy interval.

Table 5.1. Selected measurement conditions for total absorbed dose profiles presented in this work. The z-direction (depth dose) scans were performed along the central axis of the photon beam.

Photon Beam Energy (MV)	Phantom	Field Size (cm ²)	Depth (cm)	Scan Direction
25	Water	10 × 10	0–40 4, 10	z x,y

The literature contains several studies on measurements and empirical models of neutron exposures [9–13]. Relatively little attention has been paid in the literature to physics-based analytical models of neutron exposures in radiation therapy, and all such published works apply to proton therapy [7, 8, 14–17]. It was not known if a comparable model could be developed for x-ray therapy.

The objective of this work was to develop a new analytical model of absorbed dose from photoneutrons produced by a 25-MV photon beam incident on a water phantom. The model was designed and configured based on Monte Carlo simulations of high-energy x-ray beams delivered by a medical electron linear accelerator. We bench marked the Monte Carlo model with measurements of total absorbed dose.

5.2. Methods

5.2.1. Measurement of Total Absorbed Dose

The measurement equipment and setup was described elsewhere (Section 4.2.2 [18]). We measured depth dose and in-plane and cross-plane half-profiles listed in Table 5.1.

5.2.2. Monte Carlo Simulations

Simulations were performed using the Monte Carlo N-Particle eXtended (MCNPX) transport code (version 2.7) [19]. The dimensions and material definitions of the linac (Precise Treatment SystemTM, SN 151617, Elekta, Stockholm, Sweden) were taken from proprietary information provided by the manufacturer [20]. The geometry of the model is as described in Section 4.2.3 except that the 6-MV flattening filter has been replaced by the two component 25-MV flattening filter system, as illustrated in Figure 5.3. All simulations

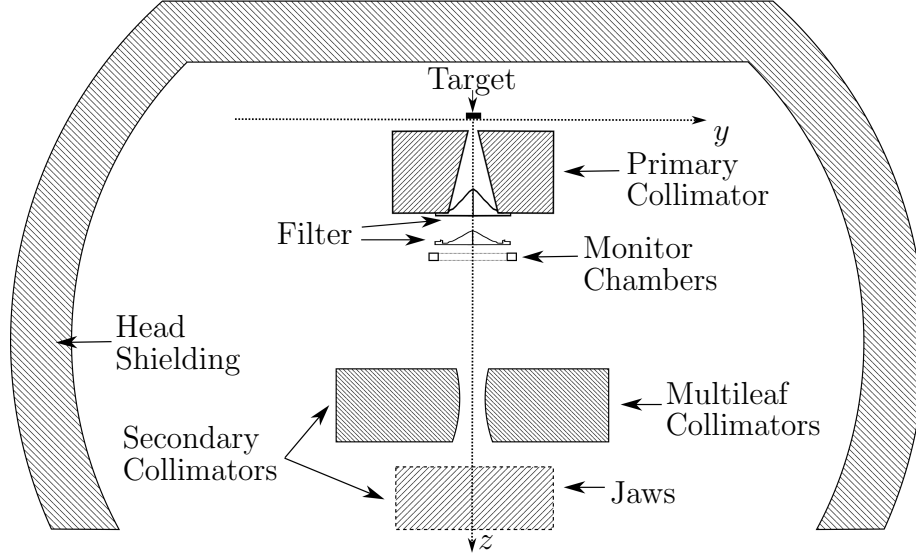


Figure 5.3. Cross-sectional schematic diagram of the linac head illustrating the relative locations of the beam-modifying and beam-limiting devices including the X-ray target, the cylindrical primary collimator, the flattening filter, the monitor chamber, the multi-leaf collimators (MLCs), jaws, and head-shielding. The location of the jaw is rendered with a dotted line since it may not intersect the yz -plane for a given field. Note: Dimensions are not to scale.

Table 5.2. Neutron energy regime definitions and number of energy bins in each regime. E_n refers to neutron energy.

Energy Regime	Definition	# of Bins in Regime
Thermal	$E_n < 3 \times 10^{-7} \text{MeV}$	13
$1/E$ (Epithermal)	$3 \times 10^{-7} \text{MeV} \leq E_n \leq 3 \times 10^{-2} \text{MeV}$	25
Evaporation	$E_n > 3 \times 10^{-2} \text{MeV}$	15

were configured to transport neutrons, photons, and electrons (mode n p e). F6-type energy deposition tallies were performed for neutron, protons, and electrons, and summed to yield the total absorbed dose at each tally location. F4-type tallies of neutron spectral fluence were binned uniformly in $\log(E_n)$ between 10^{-9} and 25 MeV. We divided the fluence into three energy regimes. The energy regime definitions and number of energy bins in each regime are list in Table 5.2.

The dose deposited by neutrons in the i^{th} energy bin was calculated with with kerma factors obtained from Chadwick et al. [21] as

$$D_{n,i} \stackrel{\text{CPE}}{=} K_{n,i} = k_{\phi,i} \times \phi_{n,i} \quad , \quad (5.1)$$

where $K_{n,i}$ is the kerma due to neutrons in the i^{th} energy bin, $k_{\phi,i}$ is the kerma coefficient for neutrons in the i^{th} energy bin, and $\phi_{n,i}$ is the neutron fluence in the i^{th} energy bin. The assumption of charged particle equilibrium is justified as results in the literature have shown $d_{\text{max},n}$ (*i.e.*, the depth of maximum neutron dose), to be at or shallower than 4 cm, the shallowest depth for which we calculated dose [22, 23].

We calculated neutron equivalent dose, (H_n), according to

$$H_{n,i} = w_R(E_i) \times D_{n,i} \quad . \quad (5.2)$$

The radiation weighting factors, $w_R(E_i)$, were calculated according to the formula from ICRP Publication 92 [24], or

$$w_R(E_n) = 2.5 \times \left[2 - \exp(-4E_n) + 6 \times \exp\left(\frac{-\ln(E_n)^2}{4}\right) + \exp\left(\frac{-\ln(E_n/30)^2}{2}\right) \right] \quad . \quad (5.3)$$

We verified the accuracy of the Monte Carlo simulations by benchmarking the simulated total absorbed dose against the corresponding measured values at the same locations. The local relative difference in dose at the q^{th} point is

$$\Delta D_i = \frac{D_{\text{MC},q} - D_{\text{m},q}}{D_{\text{m},q}} \times 100\% \quad , \quad (5.4)$$

where $D_{MC,i}$ is the Monte Carlo simulated dose at the q^{th} location, and $D_{m,q}$ is the corresponding measured value. We then calculated the mean unsigned dose difference according to

$$\overline{\Delta D} = \sum_{q=1}^{N_p} \text{abs} \left(\frac{\Delta D_q}{N_p} \right) \quad , \quad (5.5)$$

where N_p is the number of points.

From the Monte Carlo data, we also determined the fluence weighted average macroscopic neutron interaction cross section, neutron mean free path, and neutron kerma coefficient for the three neutron energy regimes considered. The average macroscopic neutron interaction cross section of the j^{th} neutron energy regime, $\overline{\Sigma}_j$, was calculated according to

$$\overline{\Sigma}_j = \sum_{i=1}^n \frac{\Sigma(E_i) \times \phi(i)}{\Phi_j} \quad , \quad (5.6)$$

where Φ_j is the total fluence of the j^{th} energy regime, $\Sigma(E_i)$ is the ENDF-VII/B macroscopic cross section for neutrons of energy E_i in water, and ϕ_i is the fluence of neutrons in the i^{th} energy bin. The neutron mean free path, also known as the relaxation length, was calculated simply as

$$\overline{\lambda}_j = \frac{1}{\overline{\Sigma}_j} \quad . \quad (5.7)$$

Finally, the fluence weighted average kerma factor of the j^{th} energy regime was calculated by

$$\overline{k_{\phi,j}} = \sum_{i=1}^n \frac{k_{\phi,i} \times \phi_i}{\Phi_j} \quad . \quad (5.8)$$

5.2.3. Analytical Model

The analytical model for neutron fluence in the j^{th} energy regime at a point, p , in the phantom is

$$\Phi_{j,p} = C_j \times \Phi_{\text{iso}} \left(\frac{r}{z_{\text{iso}}} \right)^{-q_j} \exp[-\alpha_j \overline{\Sigma}_j (r' - z'_{\text{iso}})] \exp \left[\frac{-\rho^2 z_{\text{iso}}^2}{2\sigma_j^2 z^2} \right] \times M_{j,p} \quad , \quad (5.9)$$

where Φ_{iso} is the total neutron fluence at isocenter obtained from the Monte Carlo data, $r = x^2 + y^2 + z^2$ is the distance from the neutron source to the point of calculation, z_{iso} is the distance from the neutron source to isocenter, q is an exponent governing geometric divergence of the neutron field, $\overline{\Sigma}_j$ is the mean macroscopic neutron interaction cross section (Equation 5.6), α_j is an empirical adjustment factor to the macroscopic cross section, r' is the distance through water from the source to the point of calculation, z'_{iso} is the depth of isocenter, $\rho^2 = x^2 + y^2$ for the point of calculation, σ_j is the width parameter governing the lateral falloff, the C_j factors apportion the fraction of fluence at isocenter to each of the three energy regimes such that $\sum_{j=1}^3 C_j = 1$, and $M_{j,p}$ is function that corrects for the moderation of j^{th} energy group neutrons out-of-field by the beam-limiting devices in the treatment head. We define $j = 1$ to represent the thermal neutron regime, $j = 2$ for the epithermal neutron regime, and $j = 3$ for the evaporation neutron regime. The relevant distances are labeled in Figure 2.1.

The beam-limiting devices in the treatment head are composed of poor neutron moderators such as tungsten and lead. However, their effect on neutron fluence is not negligible. The attenuation of neutron fluence in the j^{th} energy group is modeled with a cumulative distribution function, or

$$M_{j,p} = b_{M,j} + (1 - b_{M,j}) \times \left[\frac{1 - \text{erf}\left(\frac{\rho - \mu_{M,j}}{\sigma_{M,j}\sqrt{2}}\right)}{2} \right] , \quad (5.10)$$

where $\mu_{M,j}$ is the normal distribution mean, $\sigma_{M,j}$ is the width parameter, $b_{M,j}$ is a constant, and “erf” is the error function.

The absorbed dose at a point, p , is modeled as the sum of the three fluence regimes each multiplied by its corresponding mean kerma coefficient, or

$$D_p = \sum_{j=1}^3 \overline{k_{\phi,j}} \times \Phi_{j,p} \quad , \quad (5.11)$$

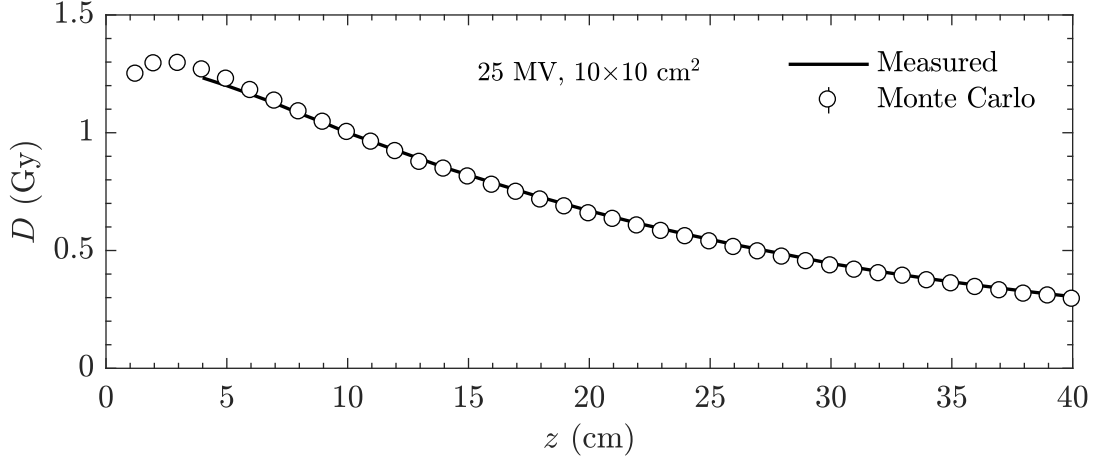


Figure 5.4. Measured and simulated dose (D) versus depth (z) of a 25-MV photon beam with a field size of $10 \times 10 \text{ cm}^2$ along the beam's central axis in water. Note: The measured curve begins at $d = 4 \text{ cm}$. This is because the thickness of the phantom wall and the size of the detector prevented shallow measurements.

where $\overline{k_{\phi,j}}$ is the average kerma factor as defined in Equation 5.8, and $\Phi_{j,p}$ is the total fluence in the j^{th} neutron energy regime at the point of calculation, p .

5.3. Results

The values of total absorbed dose obtained from the Monte Carlo simulations agreed well with the corresponding measured values. The mean local relative dose difference, $\overline{\Delta D}$, was found to be 9.9% for all locations considered. Figure 5.4 shows plots of the depth dose measured and simulated along the beam's central axis. Figures 5.5 and 5.6 show half-profiles of the measured and simulated absorbed doses in the x- and y-directions, respectively, for depths of 4, 10, 20, and 40 cm.

Figure 5.7 shows a half-profile plot of the analytical model of neutron fluence along with the Monte Carlo values. The model parameters from Equation 5.9 are listed in Table 5.3. The average local relative difference between the analytical model and the Monte Carlo data for absorbed dose from neutrons was found to be 6.8%.

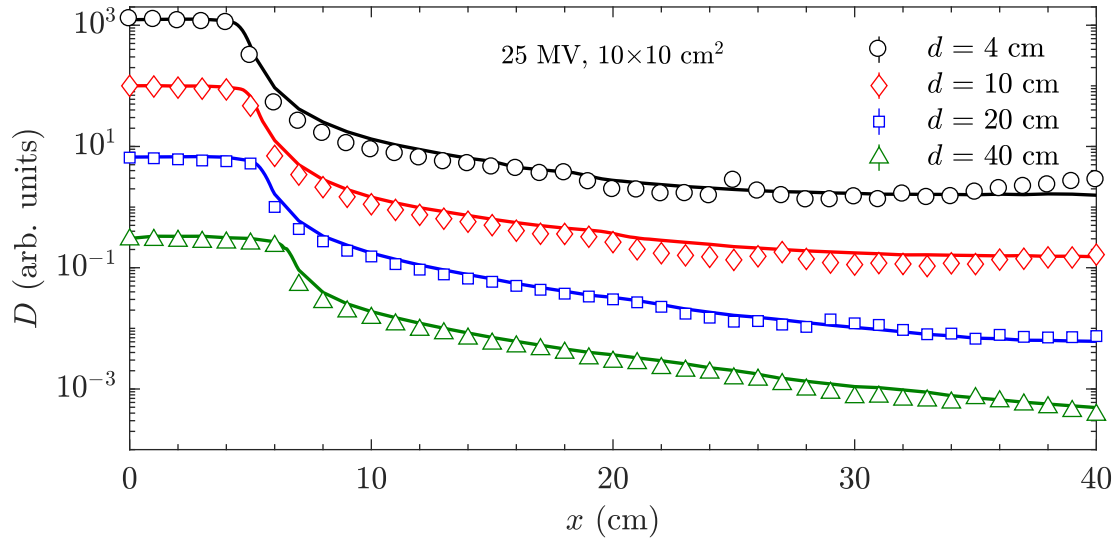


Figure 5.5. Measured and simulated absorbed dose (D) versus lateral position (x) of a 25-MV, $10 \times 10 \text{ cm}^2$ photon beam at four depths in water. The markers indicate the Monte Carlo simulation values, and the lines show the measured doses. Each curve was normalized to the measured dose at isocenter. The upper three curves were offset by an order of magnitude each for visibility.

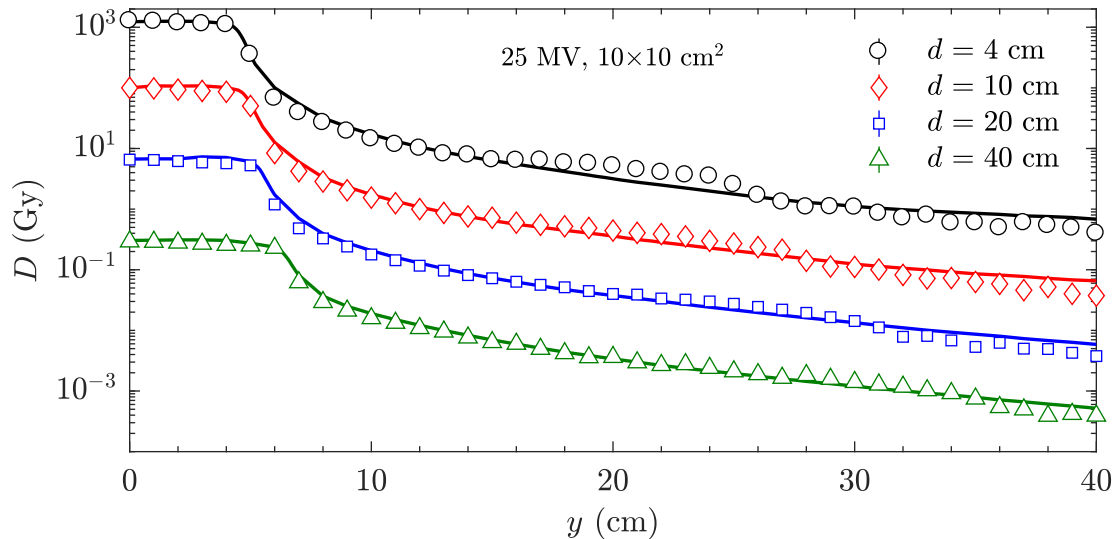


Figure 5.6. Measured and simulated absorbed dose (D) versus lateral position (y) of a 25-MV, $10 \times 10 \text{ cm}^2$ photon beam at four depths in water. The markers indicate the Monte Carlo simulation values, and the lines show the measured doses. Each curve was normalized to the measured dose at isocenter. The upper three curves were offset by an order of magnitude each for visibility.

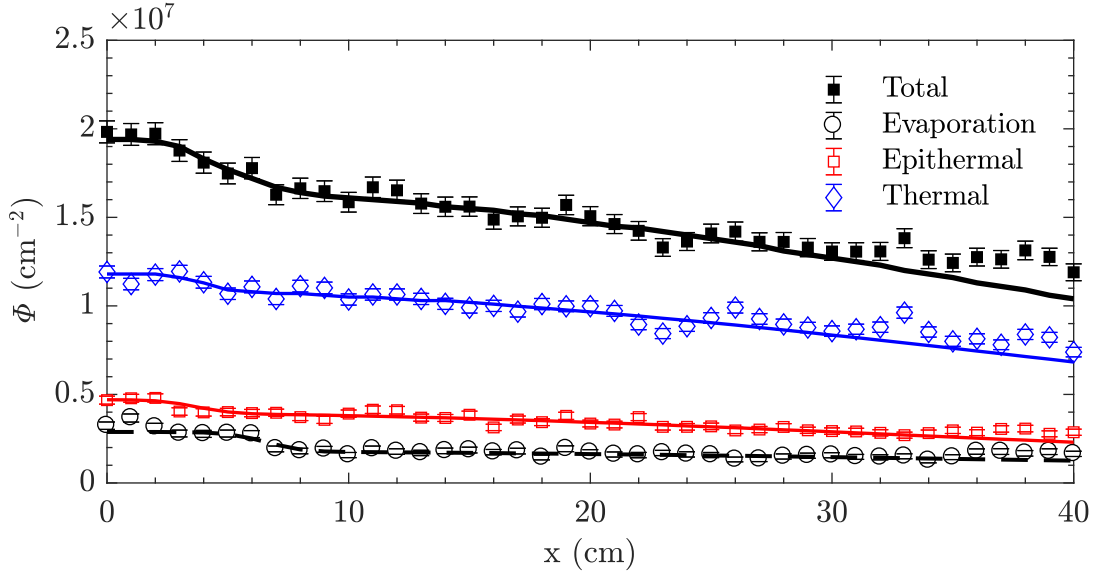


Figure 5.7. Half-profile of neutron fluence, Φ_n , predicted by Monte Carlo and analytical model. Plot is for a 25-MV, $10 \times 10 \text{ cm}^2$ x-ray field at a depth of 4 cm in a water-box phantom. Error bars indicate the standard error of the Monte Carlo tallies.

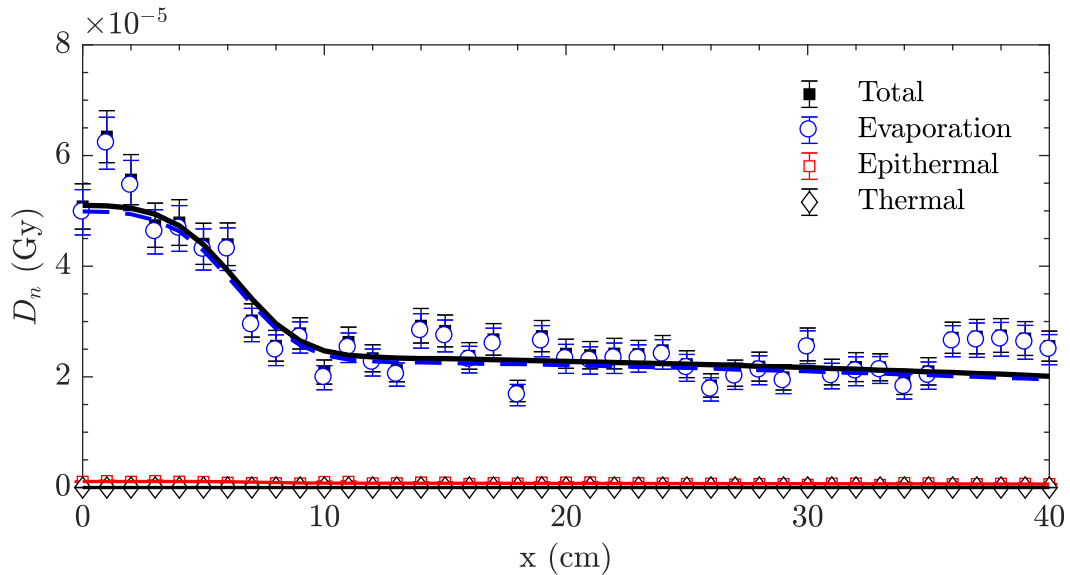


Figure 5.8. Half-profile of neutron absorbed dose, D_n , predicted by Monte Carlo and analytical model, including individual energy groups. Plot is for a 25-MV, $10 \times 10 \text{ cm}^2$ x-ray field at a depth of 4 cm in a water-box phantom. Error bars indicate the standard error of the Monte Carlo tallies.

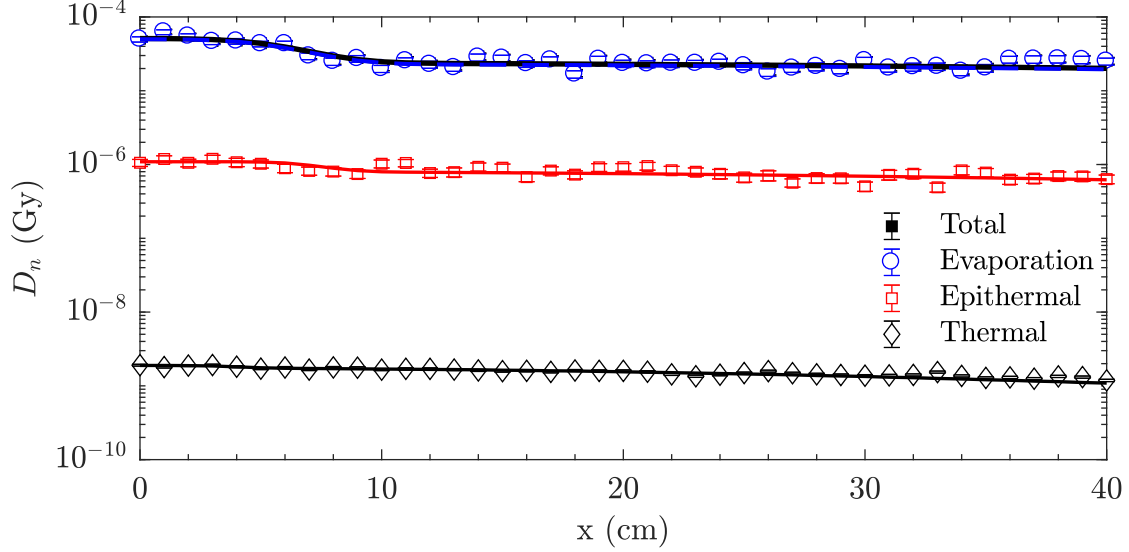


Figure 5.9. Log scale plot showing half-profile of neutron absorbed dose, D_n , predicted by Monte Carlo and analytical model, including individual energy groups. Plot is for a 25-MV, 10×10 cm² x-ray field at a depth of 4 cm in a water-box phantom. Error bars indicate the standard error of the Monte Carlo tallies.

Table 5.3. Model inputs calculated from Monte Carlo data, and model fitting parameters.

Calculated Inputs			Fitting Parameters		
Symbol	Value	Units	Symbol	Value	Units
Φ_{iso}	7.45×10^6	cm ⁻²	z_{iso}	84.6	cm
C_1	0.60	N/A	σ_1	60.6	cm
C_2	0.24	N/A	σ_2	9.78	cm
C_3	0.16	N/A	σ_3	4.65	cm
$\overline{\Sigma}_1$	0.69	cm ⁻¹	α_1	0.29	N/A
$\overline{\Sigma}_2$	0.50	cm ⁻¹	α_2	0.10	N/A
$\overline{\Sigma}_3$	0.20	cm ⁻¹	α_3	0.71	N/A
$\overline{k}_{\phi,1}$	1.6×10^{-16}	Gy cm ²	$q1$	0.10	N/A
$\overline{k}_{\phi,2}$	2.5×10^{-13}	Gy cm ²	$q2$	1.01	N/A
$\overline{k}_{\phi,3}$	2.0×10^{-11}	Gy cm ²	$q3$	0.99	N/A
			$\mu_{M,1}$	3.92	cm
			$\mu_{M,2}$	3.73	cm
			$\mu_{M,3}$	6.57	cm
			$\sigma_{M,1}$	1.04	cm
			$\sigma_{M,2}$	1.15	cm
			$\sigma_{M,3}$	1.20	cm
			$b_{M,1}$	0.92	N/A
			$b_{M,2}$	0.84	N/A
			$b_{M,3}$	0.62	N/A

5.4. Discussion

In this work we developed a new analytical model of absorbed dose from neutron contamination in a 25-MV photon beam. To configure the model, we performed Monte Carlo simulations of neutron fluence and total absorbed dose, and we performed measurements of the total absorbed dose both in- and out-of-field in order to validate the Monte Carlo simulations. The major finding of this work is that it appears to be feasible to calculate the neutron dose, $D_n(x, y, z)$, with a fast and accurate analytical model suitable for use in the clinical workflow, which is not current achievable with measurements or Monte Carlo simulations. This has implications for radiotherapy treatment planning, clinical decision making, and for retrospective studies of the effects of neutron exposures to radiation therapy patients.

Strengths of this study include the novelty of modeling the photoneutron absorbed dose from three neutron energy regimes. This is similar to the approach our laboratory has taken in modeling neutron dose in proton therapy treatments [7, 8]. To our knowledge, no other work has applied this approach to photoneutron modeling in x-ray radiation therapy. We separately modeled neutron absorbed dose and neutron weighting factors to facilitate the use of other energy dependent radiation weight factors and dose-response models that may supersede ICRP Publication 92 in the future.

Limitations of this work include that we only considered 25-MV x-ray beams. This is the highest x-ray beam energy routinely used in clinics and is, thus, the beam energy for which the photoneutron hazard is greatest. Work is on going in our laboratory to extend this model to the full interval of clinically relevant photon beam energies. Another limitation is the lack of measured neutron absorbed doses to validate the model. This is not a serious limitation because we partially validated our Monte Carlo model against measurements of total absorbed dose, and previous studies have shown the Monte Carlo software package we used to be reliable for calculating photoneutron exposures [9, 23].

5.5. References

- ¹P. H. McGinley, M. Wood, M. Mills, and R. Rodriguez, “Dose levels due to neutrons in the vicinity of high-energy medical accelerators”, *Med Phys* **3**, 397–402 (1976).
- ²P. H. McGinley and E. K. Butker, “Evaluation of neutron dose equivalent levels at the maze entrance of medical accelerator treatment rooms”, *Med Phys* **18**, 279–81 (1991).
- ³A. Naseri and A. Mesbahi, “A review on photoneutrons characteristics in radiation therapy with high-energy photon beams”, *Rep Pract Oncol Radiother* **15**, 138–44 (2010).
- ⁴NCRP, *NCRP Report No. 116 - Limitation of exposure to ionizing radiation* (National Council on Radiation Protection and Measurements, Bethesda, MD, 1993).
- ⁵A. H. Karimi, H. Brkic, D. Shahbazi-Gahrouei, S. B. Haghghi, and I. Jabbari, “Essential considerations for accurate evaluation of photoneutron contamination in radiotherapy”, *Appl Radiat Isot* **145**, 24–31 (2019).
- ⁶N. Mohammadi, S. H. Miri-Hakimabad, and L. Rafat-Motavalli, “A Monte Carlo study for photoneutron dose estimations around the high-energy linacs”, *J Biomed Phys Eng* **4**, 127–40 (2014).
- ⁷A. Perez-Andujar, R. Zhang, and W. Newhauser, “Monte Carlo and analytical model predictions of leakage neutron exposures from passively scattered proton therapy”, *Med Phys* **40**, 121714 (2013).
- ⁸C. Schneider, W. Newhauser, and J. Farah, “An analytical model of leakage neutron equivalent dose for passively-scattered proton radiotherapy and validation with measurements”, *Cancers (Basel)* **7**, 795–810 (2015).
- ⁹A. Mesbahi, H. Ghiasi, and S. R. Mahdavi, “Photoneutron and capture gamma dose equivalent for different room and maze layouts in radiation therapy”, *Radiat Prot Dosimetry* **140**, 242–9 (2010).
- ¹⁰A. Hakimi, M. Sohrabi, and S. Rabie Mahdavi, “Effects of field size and depth on photoneutron dose equivalent distributions in an 18 MV x-ray medical accelerator”, *Radiat Prot Dosimetry* **176**, 354–364 (2017).
- ¹¹M. Sohrabi and A. Hakimi, “Novel 6MV x-ray photoneutron detection and dosimetry of medical accelerators”, *Phys Med* **36**, 103–109 (2017).
- ¹²R. Khabaz, R. Boodaghi, M. R. Benam, and V. Zanganeh, “Estimation of photoneutron dosimetric characteristics in tissues/organs using an improved simple model of linac head”, *Appl Radiat Isot* **133**, 88–94 (2018).

- ¹³L. Montgomery, M. Evans, L. Liang, R. Maglieri, and J. Kildea, “The effect of the flattening filter on photoneutron production at 10 MV in the Varian TrueBeam linear accelerator”, *Med Phys* **45**, 4711–4719 (2018).
- ¹⁴Y. Zheng, W. Newhauser, J. Fontenot, P. Taddei, and R. Mohan, “Monte Carlo study of neutron dose equivalent during passive scattering proton therapy”, *Phys Med Biol* **52**, 4481–96 (2007).
- ¹⁵R. Zhang, A. Perez-Andujar, J. D. Fontenot, P. J. Taddei, and W. D. Newhauser, “An analytic model of neutron ambient dose equivalent and equivalent dose for proton radiotherapy”, *Phys Med Biol* **55**, 6975–85 (2010).
- ¹⁶K. J. Gallagher and P. J. Taddei, “Independent application of an analytical model for secondary neutron equivalent dose produced in a passive-scattering proton therapy treatment unit”, *Phys Med Biol* **63**, 15NT04 (2018).
- ¹⁷K. J. Gallagher and P. J. Taddei, “Analytical model to estimate equivalent dose from internal neutrons in proton therapy of children with intracranial tumors”, *Radiat Prot Dosimetry* (2018) 10.1093/rpd/ncy166.
- ¹⁸C. W. Schneider, W. D. Newhauser, L. J. Wilson, and R. Kapsch, “A physics-based analytical model of absorbed dose from primary, leakage, and scattered photons from megavoltage radiotherapy with MLCs”, (In Revision, 2019).
- ¹⁹D. B. Pelowitz, *MCNPX user’s manual version 2.7.0* (Los Alamos, NM, 2011).
- ²⁰Elekta, *Information for Monte Carlo modeling of the Elekta linear accelerator, Personal communication*, Nov. 2018.
- ²¹M. B. Chadwick, H. H. Barschall, R. S. Caswell, P. M. DeLuca, G. M. Hale, D. T. Jones, R. E. MacFarlane, J. P. Meulders, H. Schuhmacher, U. J. Schrewe, A. Wambersie, and P. G. Young, “A consistent set of neutron kerma coefficients from thermal to 150 MeV for biologically important materials”, *Med Phys* **26**, 974–91 (1999).
- ²²H. A. Nedaie, H. Darestani, N. Banaee, N. Shagholi, K. Mohammadi, A. Shahvar, and E. Bayat, “Neutron dose measurements of Varian and Elekta linacs by TLD600 and TLD700 dosimeters and comparison with MCNP calculations”, *J Med Phys* **39**, 10–7 (2014).
- ²³S. F. Kry, R. M. Howell, M. Salehpour, and D. S. Followill, “Neutron spectra and dose equivalents calculated in tissue for high-energy radiation therapy”, *Med Phys* **36**, 1244–50 (2009).
- ²⁴ICRP, *ICRP Publication 92: Relative biological effectiveness (RBE), quality factor (Q), and radiation weighting factor (w_R)* (International Commission on Radiological Protection, B, 2003).

Chapter 6.

External and Internal Neutron Absorbed Dose from Proton Radiotherapy

6.1. Introduction

Proton therapy has been found to achieve desired tumor volume coverage with lower dose to a patient's healthy tissues in many cases compared with other forms of radiation therapy [1–3]. Some stray radiation exposure, however, is unavoidable [4, 5]. In proton therapy, the dominant source of stray radiation is neutron contamination. Stray neutrons are primarily produced by nuclear reactions between primary protons and atomic nuclei in the treatment head as well as in the patient or phantom [6]. Neutrons emanating from the treatment head are referred to as external or leakage neutrons. Neutrons produced in the patient are referred to as internal or patient-scattered neutrons.

Previous works from our laboratory have reported on Monte Carlo and analytical models of external neutron exposures from passively-scattered proton therapy (PSPT) [7–9]. In this work, we report on simulations of external and internal neutron exposures from a compact commercial proton therapy system.

6.2. Methods

The PSPT Monte Carlo simulations were conducted with a model of the proton therapy gantry beamline at the *Centre de Protonthérapie de l'Institut Curie* in Orsay, France. The clinic is a three room proton therapy center that operates two fixed beamlines, in addition to the gantry beamline, based on the Proteus Plus system (IBA, Louvain-La-Neuve, Belgium). Simulations were performed using the Monte Carlo N-Particle eXtended (MCNPX) code version 2.7 [10] for proton beam energies of 162, 192, 207, and 219 MeV. These energies were chosen to coincide with those from a previous work [11]. The field simulated was circular with a diameter of 5.5 cm. We exploited this radial symmetry by simulating a 1-m diameter cylindrical water phantom.

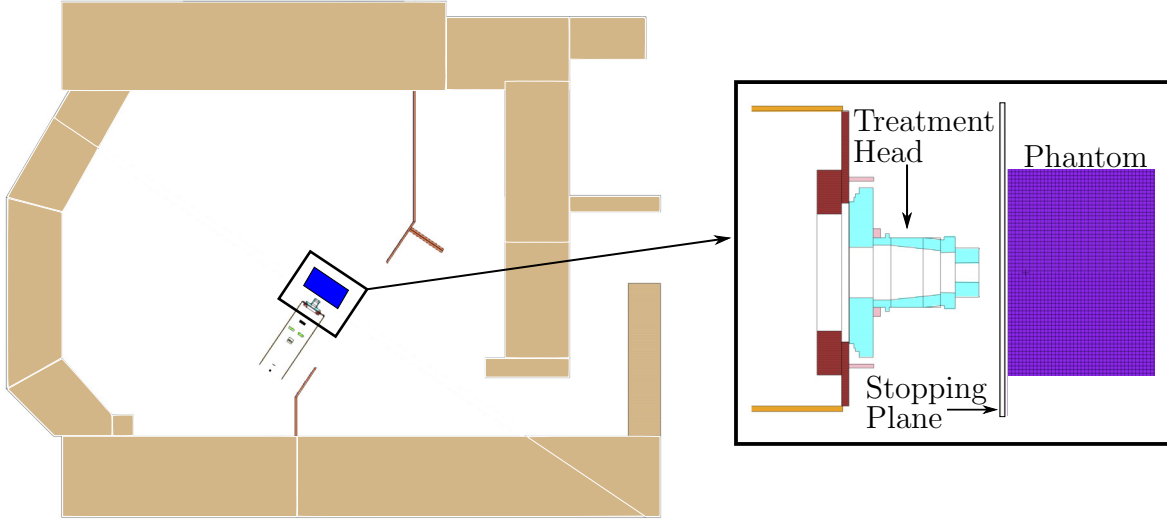


Figure 6.1. Monte Carlo simulation vault geometry. The inset shows a magnified view of the treatment head and phantom.

The Monte Carlo geometry consisted of the treatment vault and proton therapy treatment head setup for the passive-scattering technique. Figure 6.1 shows a plot of the vault geometry and a close up view of the treatment head, voxelized water phantom, and the location of the stopping plane. The stopping plane was used alternatively to stop either external neutrons (`imp:n=0, imp:h=1`) or to stop primary protons (`imp:n=1, imp:h=0`) in order to discriminate between the dose from external and internal neutrons. Simulations were also run with the no particles stopped in the plane (`imp:n=1, imp:h=1`) in order to tally the total dose from protons and neutrons. Tallies of neutron fluence were binned logarithmically in energy with 40 energy bins per decade.

The phantom was voxelized in cylindrical coordinates with the off-axis distance denoted ρ , depth in water denoted d , and azimuthal angle denoted φ . The step sizes for voxelization were $\delta d = 1$ cm, $\delta\varphi = \pi/4$ radians, and $\delta\rho = 1$ cm for $\rho < 28$ cm and $\delta\rho = 2$ cm for $\rho = 28$ cm to 50 cm. This yields a total of 6.4×10^4 voxels. All simulation results were normalized per 10^9 primary protons.

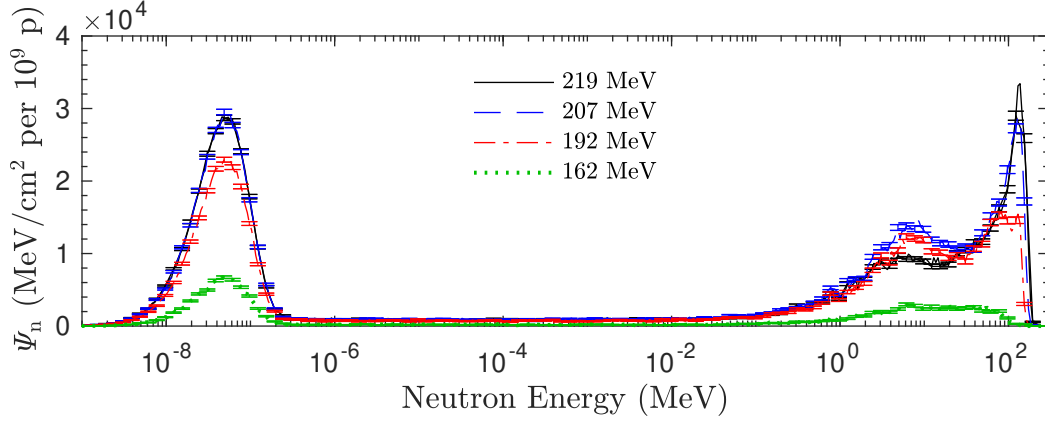


Figure 6.2. Spectral neutron energy fluence, Ψ_n , on central axis at 10-cm depth in water for all proton beam energies considered.

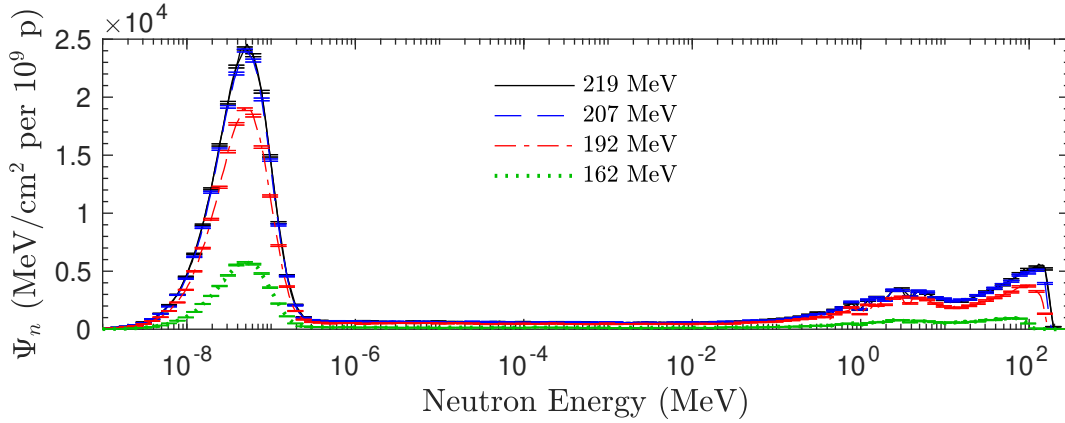


Figure 6.3. Spectral neutron energy fluence, Ψ_n , 10 cm off-axis at 10-cm depth in water for all proton beam energies considered.

6.3. Results

The neutron spectral energy fluence is shown at 10-cm depth in water along the central axis for all proton beam energies considered in Figure 6.2. Figure 6.3 shows the same at an off-axis distance of $\rho = 10$ cm. The spectral energy fluence from all neutrons, only external neutrons, and only internal neutrons are plotted in Figure 6.4 for the 219-MeV beam at $\rho = 0$ cm and $d = 10$ cm. Figure 6.5 shows the corresponding data at 10 cm off-axis.

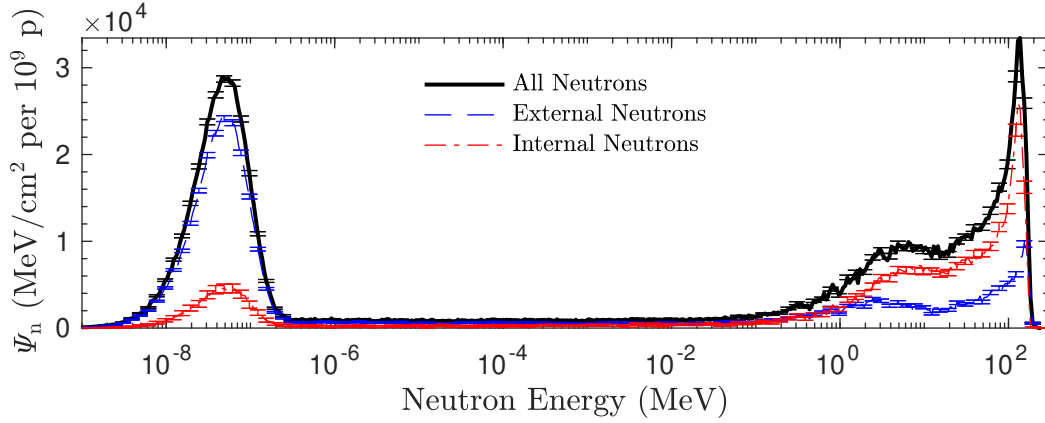


Figure 6.4. Spectral neutron energy fluence, Ψ_n , from all neutrons, external neutrons, and internal neutrons on central axis at 10-cm depth in water for the 219-MeV proton beam.

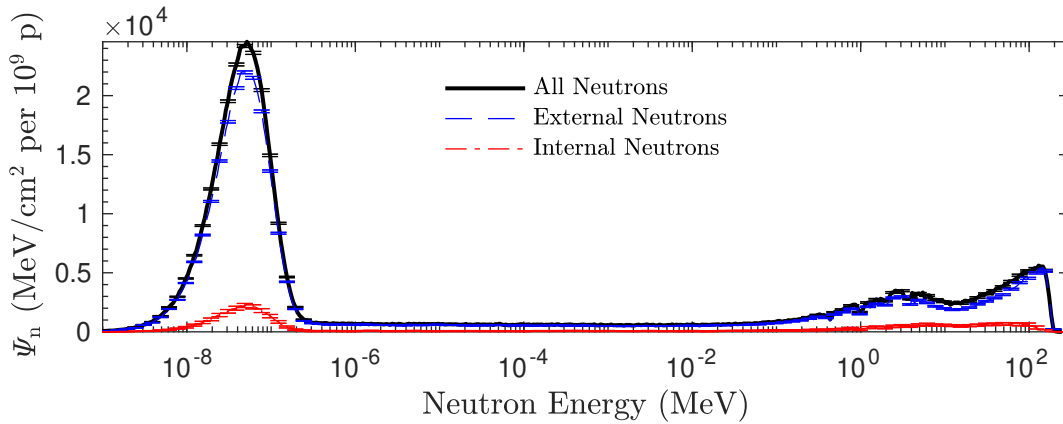


Figure 6.5. Spectral neutron energy fluence, Ψ_n , from all neutrons, external neutrons, and internal neutrons 10-cm off-axis at 10-cm depth in water for the 219-MeV proton beam.

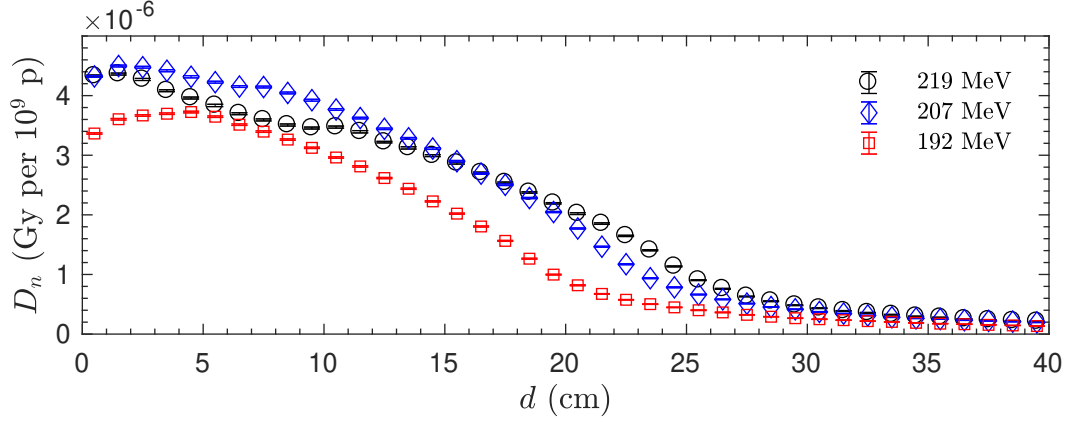


Figure 6.6. Neutron absorbed dose, D_n , along the proton beam's central axis for several proton beam energies.

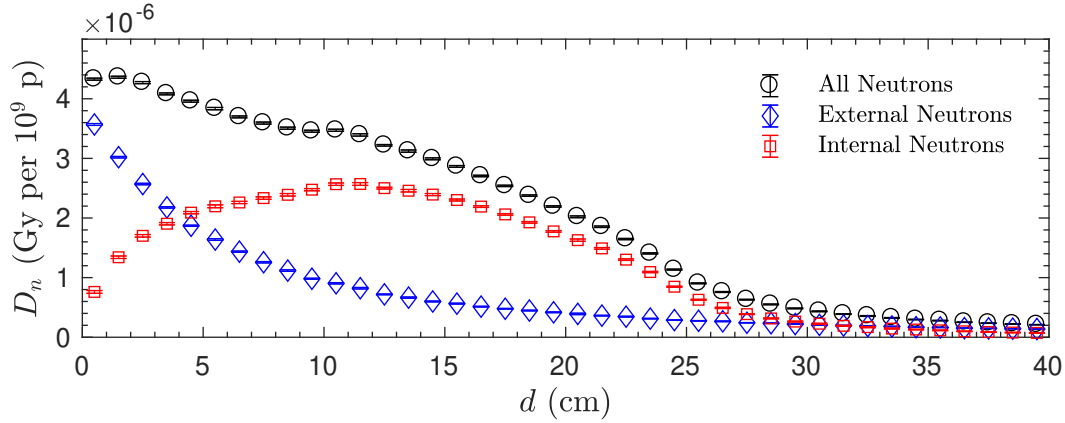


Figure 6.7. Neutron absorbed dose, D_n , from all neutrons, external neutrons, and internal neutrons along the proton beam's central axis for the 219-MeV beam.

Absorbed dose from neutrons along central axis is shown for three beam energies in Figure 6.6. Figure 6.7 shows a breakdown of the total, external, and internal neutron dose along central axis for the 219-MeV beam.

Figure 6.8 shows a half profile of the total absorbed dose, along with the proton and neutron doses, from the 219-MeV beam at a depth of 10 cm in water. In this plot, the dose from internal neutrons is greater than that of external neutrons in the in-field and near-field regions. Linearly interpolated estimations of the off-axis distance at which the dose from external neutrons equals that of internal neutrons are listed in Table 6.1 for different proton beam energies and depths in water.

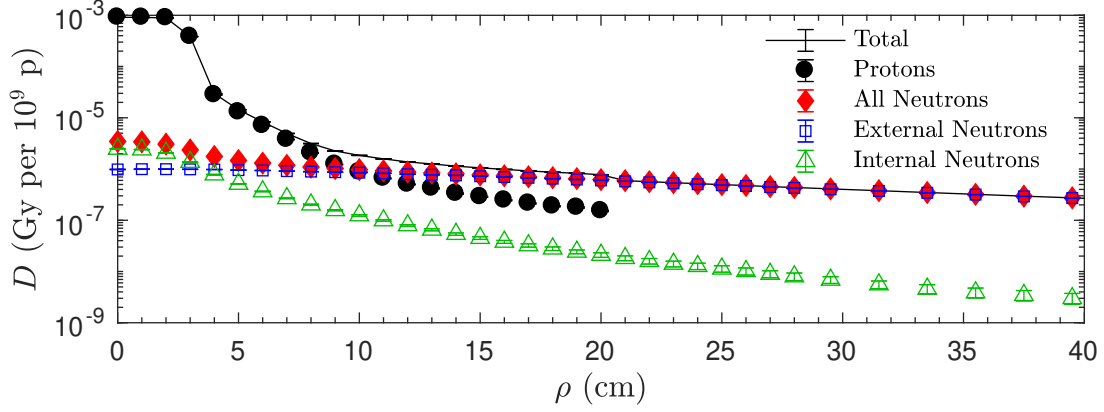


Figure 6.8. Total absorbed dose, D , for the 219-MeV beam versus off-axis distance, ρ , at a depth of 10 cm in water. Also shown are the absorbed doses from protons, the dose from all neutrons, and the dose from external and internal neutrons, respectively.

Table 6.1. Off-axis distances, ρ , at which absorbed dose from external neutrons overtakes that of internal neutrons for three proton beam energies and depths in water. Also listed are the distances, δ , from the field edge at which external neutron dose overtakes that of internal neutrons, with positive values indicating that the transition takes place outside of the primary treatment field.

Depth (cm)	192 MeV		207 MeV		219 MeV	
	ρ (cm)	δ (cm)	ρ (cm)	δ (cm)	ρ (cm)	δ (cm)
5	2.71	0.21	2.29	-0.21	1.44	-1.06
10	4.13	1.63	3.97	1.47	3.59	1.09
20	5.47	2.97	6.20	3.70	5.90	3.40

6.4. Discussion

In this work, we performed Monte Carlo simulations of the neutron fluence and proton and neutron absorbed dose from a modern, compact proton therapy system. We segregated the neutron energy fluence and absorbed dose from external neutrons (produced in the treatment head) and internal neutrons (produced in the phantom). We also estimated the off-axis distance at which the dose from external neutrons becomes greater than that from internal neutrons.

The results of this work show that the absorbed dose from internal neutrons may be greater than that of external neutrons both in and near the primary treatment field. The distance beyond the field-edge at which external neutron dose surpasses the internal neutron dose increases with increasing depth in the phantom and does not appear to depend strongly on the proton beam energy. This is an important finding because the region in the periphery of the primary treatment field exhibits the greatest risk per volume for radiation late effects such as second cancers. Attempts to estimate such risks while considering only external neutron doses may lead to underestimations.

Strengths of this study include the use a Monte Carlo model based on design drawings from a modern proton therapy facility and the inclusion of multiple clinically relevant beam energies. Additionally, the use a radially symmetric computational phantom with voxels based in cylindrical coordinates resulted in excellent simulation statistics even far from the primary field, making this simulated data potentially useful for the design and configuration of analytical models of external and internal neutron dose. Limitations of this study include the use of only a single field size and the lack of simulated irradiations on any heterogeneous phantom. Future work should include the addition of multiple field sizes including irregularly shaped fields.

6.5. References

- ¹R. Miralbell, A. Lomax, L. Cella, and U. Schneider, “Potential reduction of the incidence of radiation-induced second cancers by using proton beams in the treatment of pediatric tumors”, *Int J Radiat Oncol Biol Phys* **54**, 824–9 (2002).
- ²W. D. Newhauser, J. D. Fontenot, A. Mahajan, D. Kornguth, M. Stovall, Y. Zheng, P. J. Taddei, D. Mirkovic, R. Mohan, J. D. Cox, and S. Woo, “The risk of developing a second cancer after receiving craniospinal proton irradiation”, *Phys Med Biol* **54**, 2277–91 (2009).
- ³R. Zhang, R. M. Howell, A. Giebeler, P. J. Taddei, A. Mahajan, and W. D. Newhauser, “Comparison of risk of radiogenic second cancer following photon and proton craniospinal irradiation for a pediatric medulloblastoma patient”, *Phys Med Biol* **58**, 807–23 (2013).
- ⁴S. Agosteo, C. Birattari, M. Caravaggio, M. Silari, and G. Tosi, “Secondary neutron and photon dose in proton therapy”, *Radiother Oncol* **48**, 293–305 (1998).
- ⁵X. Yan, U. Titt, A. M. Koehler, and W. D. Newhauser, “Measurement of neutron dose equivalent to proton therapy patients outside of the proton radiation field”, *Nuclear Instruments and Methods in Physics Research A* **476**, 429–34 (2002).
- ⁶W. D. Newhauser and R. Zhang, “The physics of proton therapy”, *Phys Med Biol* **60**, R155–209 (2015).
- ⁷Y. Zheng, W. Newhauser, J. Fontenot, P. Taddei, and R. Mohan, “Monte Carlo study of neutron dose equivalent during passive scattering proton therapy”, *Phys Med Biol* **52**, 4481–96 (2007).
- ⁸R. Zhang, A. Perez-Andujar, J. D. Fontenot, P. J. Taddei, and W. D. Newhauser, “An analytic model of neutron ambient dose equivalent and equivalent dose for proton radiotherapy”, *Phys Med Biol* **55**, 6975–85 (2010).
- ⁹A. Perez-Andujar, R. Zhang, and W. Newhauser, “Monte Carlo and analytical model predictions of leakage neutron exposures from passively scattered proton therapy”, *Med Phys* **40**, 121714 (2013).
- ¹⁰D. B. Pelowitz, *MCNPX user’s manual version 2.7.0* (Los Alamos, NM, 2011).
- ¹¹A. Bonfrate, J. Farah, L. De Marzi, S. Delacroix, J. Herault, R. Sayah, C. Lee, W. E. Bolch, and I. Clairand, “Influence of beam incidence and irradiation parameters on stray neutron doses to healthy organs of pediatric patients treated for an intracranial tumor with passive scattering proton therapy”, *Phys Med* **32**, 590–9 (2016).

Chapter 7.

Conclusion

This work reports several related advancements in characterizing stray radiation dose from radiotherapy. In Chapter 2, we reported a new analytical model to predict leakage neutron exposures from proton therapy. In Chapters 3 and 4 we presented new analytical models of absorbed dose from primary and stray photons in megavoltage x-ray radiation therapy. To develop, configure, and test the models, we made in-field and out-of-field dose measurements. In order to accurately predict the out-of-field photon exposures, it was necessary to model the geometry of the collimators in greater detail than was previously attempted in the literature. In Chapter 5, we reported a model of photoneutron absorbed dose from 25-MV x-ray radiotherapy. Finally, in Chapter 6, we report a Monte Carlo model of external and internal neutron energy fluence and absorbed dose from a modern, compact proton therapy system.

7.1. Implications

The works presented in this dissertation suggest that it is feasible to calculate the radiation exposure due to primary and stray radiation from megavoltage x-ray radiation therapy and proton therapy. The results revealed strong variation in the absorbed dose out-of-field, suggesting that personalized exposure assessments will be needed.

The results of this work may find applications in clinical tools to prospectively provide such information for radiotherapy patients. This would be useful for enabling the direct optimization of radiotherapy patient health outcomes [1]. Radiation epidemiology studies often must retrospectively reconstruct exposures to large numbers of patients with limited dosimetric data available from the original treatment plan. The reported analytical models could be used to accomplish such a task. Other applications include estimating doses to late-responding tissues in cases of re-irradiation [2, 3], estimating the photon and neutron dose to radiosensitive medical implants such as pacemakers [4], and estimating the dose to the fetus in the case of a pregnant radiotherapy patient [5–7].

7.2. Coherence with the Literature

The models reported in this dissertation exhibit generally good agreement with others found in the literature. However, direct comparisons of our reported models with published literature were not possible for some previous studies. Many works describing analytical models of stray radiation dose are only applicable for specific treatment machines and techniques. Furthermore, most previous reports of analytical models of stray radiation are not reproducible because they neglected to report model parameter values, model equations, and other information necessary to replicate the results. For models of secondary neutron exposures, an additional obstacle is that not all attempts at modeling have focused on the same quantity of radiation exposure, with some researchers choosing to model equivalent dose and others absorbed dose. That said, the equivalent dose predictions of our model of leakage neutron exposure from passively-scattered proton therapy reported in Chapter 2 agree with those predicted by Perez-Andujar et al. [8] within 9%.

The previously published work that is most directly comparable to the photon models reported in this dissertation is that of Jagetic and Newhauser [9], which reported an absorbed dose model for 6-MV photons applicable at depths of 1.5 and 10 cm for off-axis distances of 0–40 cm in the in- and cross-plane directions. The total absorbed doses predicted for these conditions by the simplified photon absorbed dose model from Chapter 3 and the physics-based photon absorbed dose model from Chapter 4 of this work each agree with the doses predicted by Jagetic and Newhauser within 10%. While the total doses do agree well, the proportions of leakage, head-scatter, and patient-scatter dose reported in Chapter 4 differ from those reported by Jagetic and Newhauser. This is not a concern, because the model components reported in this work were developed and configured based on more measured data and on benchmarked Monte Carlo simulations of leakage, head-scatter, and patient-scattered radiation.

Direct comparisons of the measurements performed in this dissertation with those from the literature are difficult because the stray radiation exposures from different models of treatment machines vary by an order of magnitude [10]. However, the models reported in Chapters 2 and 3 were based partially on previously published Monte Carlo data and measurements from Perez-Andujar et al. [8] and Halg et al. [11], and agreed with both previously published and original data. Additionally, the measured out-of-field photon doses produced for this dissertation qualitatively agree with previously reported measurements including Stovall et al. [5], Kase et al. [12], and Kaderka et al. [13]. These works reported that the dose can be roughly described as falling off quasi-exponentially with distance from the field-edge, although this dissertation included more measurement locations than the previous works and is the only such work to consider points lying outside of the in- and cross-planes.

7.3. Future Work

The long-term goal of this work is to improve the health outcomes of radiotherapy patients by providing the clinical and research tools necessary to reduce the risk of radiation late effects. Some additional research will be required before this can be fully realized. Future work should include the independent implementation of the models presented to ensure reproducibility. The technical feasibility of integrating these models in commercial treatment planning systems should also be studied. The model presented in Chapter 2 was implemented into a research treatment planning system by Eley et al. [14]. This model was also independently implemented by Gallagher and Taddei [15].

This dissertation examined externally produced secondary neutron doses from collimated passively-scattered proton beams and the internally (*i.e.*, within the patient) produced secondary neutrons. However, proton therapy treatments delivered via pencil-beam scanning with the addition of collimators to improve penumbral widths are becoming more common, and so it is necessary to investigate the external neutron production from pencil beam treatments delivered with collimators such as proton mini-beam treatments [16–18].

Additionally, the compact, cyclotron based proton therapy units in use at many new proton centers adjust the proton-beam energy via the use of low-Z range-shifter slabs located in the treatment head [19]. The use of energy degraders in close proximity to the patient will also result in increased neutron exposure that should be characterized.

7.4. References

- ¹L. A. Rechner, J. G. Eley, R. M. Howell, R. Zhang, D. Mirkovic, and W. D. Newhauser, “Risk-optimized proton therapy to minimize radiogenic second cancers”, *Phys Med Biol* **60**, 3999–4013 (2015).
- ²A. W. M. Lee, W. Foo, S. C. K. Law, L. J. Peters, Y. F. Poon, R. Chappell, W. M. Sze, S. K. O, S. Y. Tung, W. H. Lau, and J. H. C. Ho, “Total biological effect on late reactive tissues following reirradiation for recurrent nasopharyngeal carcinoma”, *Int J Radiat Oncol Biol Phys* **46**, 865–872 (2000).
- ³M. C. Ward et al., “A competing risk nomogram to predict severe late toxicity after modern re-irradiation for squamous carcinoma of the head and neck”, *Oral Oncol* **90**, 80–86 (2019).
- ⁴C. W. Hurkmans, J. L. Knegjens, B. S. Oei, A. J. Maas, G. J. Uiterwaal, A. J. van der Borden, M. M. Ploegmakers, L. van Erven, R. Dutch Society of, and Oncology, “Management of radiation oncology patients with a pacemaker or icd: a new comprehensive practical guideline in the netherlands. dutch society of radiotherapy and oncology (nvro)”, *Radiat Oncol* **7**, 198 (2012).
- ⁵M. Stovall, C. R. Blackwell, J. Cundiff, D. H. Novack, J. R. Palta, L. K. Wagner, E. W. Webster, and R. J. Shalek, “Fetal dose from radiotherapy with photon beams: report of AAPM radiation therapy committee Task Group No. 36”, *Med Phys* **22**, 63–82 (1995).
- ⁶R. Mazzola, S. Corradini, M. Eidemueller, V. Figlia, A. Fiorentino, N. Giaj-Levra, L. Nicosia, F. Ricchetti, M. Rigo, M. Musola, M. Ceccaroni, S. Gori, S. M. Magrini, and F. Alongi, “Modern radiotherapy in cancer treatment during pregnancy”, *Crit Rev Oncol Hematol* **136**, 13–19 (2019).
- ⁷S. F. Kry, B. Bednarz, R. M. Howell, L. Dauer, D. Followill, E. Klein, H. Paganetti, B. Wang, C. S. Wu, and X. George Xu, “AAPM TG 158: measurement and calculation of doses outside the treated volume from external-beam radiation therapy”, *Med Phys* **44**, e391–e429 (2017).
- ⁸A. Perez-Andujar, R. Zhang, and W. Newhauser, “Monte Carlo and analytical model predictions of leakage neutron exposures from passively scattered proton therapy”, *Med Phys* **40**, 121714 (2013).

- ⁹L. J. Jagetic and W. D. Newhauser, “A simple and fast physics-based analytical method to calculate therapeutic and stray doses from external beam, megavoltage x-ray therapy”, *Phys Med Biol* **60**, 4753–75 (2015).
- ¹⁰C. W. Schneider, W. D. Newhauser, L. J. Wilson, U. Schneider, R. Kaderka, S. Miljanic, Z. Knezevic, L. Stolarczyk, M. Durante, and R. M. Harrison, “A descriptive and broadly applicable model of therapeutic and stray absorbed dose from 6 to 25 MV photon beams”, *Med Phys* **44**, 3805–3814 (2017).
- ¹¹R. A. Halg, J. Besserer, and U. Schneider, “Systematic measurements of whole-body dose distributions for various treatment machines and delivery techniques in radiation therapy”, *Med Phys* **39**, 7662–76 (2012).
- ¹²K. R. Kase, G. K. Svensson, A. B. Wolbarst, and M. A. Marks, “Measurements of dose from secondary radiation outside a treatment field”, *Int J Radiat Oncol Biol Phys* **9**, 1177–83 (1983).
- ¹³R. Kaderka, D. Schardt, M. Durante, T. Berger, U. Ramm, J. Licher, and C. La Tessa, “Out-of-field dose measurements in a water phantom using different radiotherapy modalities”, *Phys Med Biol* **57**, 5059–74 (2012).
- ¹⁴J. Eley, W. Newhauser, K. Homann, R. Howell, C. Schneider, M. Durante, and C. Bert, “Implementation of an analytical model for leakage neutron equivalent dose in a proton radiotherapy planning system”, *Cancers (Basel)* **7**, 427–38 (2015).
- ¹⁵K. J. Gallagher and P. J. Taddei, “Independent application of an analytical model for secondary neutron equivalent dose produced in a passive-scattering proton therapy treatment unit”, *Phys Med Biol* **63**, 15NT04 (2018).
- ¹⁶C. Guardiola, C. Peucelle, and Y. Prezado, “Optimization of the mechanical collimation for minibeam generation in proton minibeam radiation therapy”, *Med Phys* **44**, 1470–1478 (2017).
- ¹⁷Y. Prezado, G. Jouvion, D. Hardy, A. Patriarca, C. Nauraye, J. Bergs, W. Gonzalez, C. Guardiola, M. Juchaux, D. Labiod, R. Dendale, L. Jourdain, C. Sebrie, and F. Pouzoulet, “Proton minibeam radiation therapy spares normal rat brain: long-term clinical, radiological and histopathological analysis”, *Sci Rep* **7**, 14403 (2017).
- ¹⁸L. De Marzi, A. Patriarca, C. Nauraye, E. Hierso, R. Dendale, C. Guardiola, and Y. Prezado, “Implementation of planar proton minibeam radiation therapy using a pencil beam scanning system: a proof of concept study”, *Med Phys* **45**, 5305–5316 (2018).
- ¹⁹R. Pidikiti, B. C. Patel, M. R. Maynard, J. P. Dugas, J. Syh, N. Sahoo, H. T. Wu, and L. R. Rosen, “Commissioning of the world’s first compact pencil-beam scanning proton therapy system”, *J Appl Clin Med Phys* **19**, 94–105 (2018).

Appendix.

Publication Agreements and Permissions

From: Support support@mdpi.com
Subject: Re: Request for permission to reuse article material in disseration
Date: July 3, 2017 at 8:12 PM
To: Christopher W Schneider cschn19@lsu.edu



Dear Mr. Schneider,

Thank you very much for your email. As author of the paper and given that you are the owner of the copyrights, you are entitled to reproduce the material in other publications. Please only remember to refer to the work properly, for example, adding a sentence similar to "reproduced/modified from Haring et al. 2017". Hope it helps.

Kind regards,
Fuli Cao
MDPI Support

--

Ms. Fuli Cao
MDPI Branch Office, Beijing
Tel. + 86 10 8152 1170
E-Mail: fuli.cao@mdpi.com

Disclaimer: The information and files contained in this message are confidential and intended solely for the use of the individual or entity to whom they are addressed. If you have received this message in error, please notify me and delete this message from your system. You may not copy this message in its entirety or in part, or disclose its contents to anyone.

On 2017/7/4 5:35, Christopher W Schneider wrote:

To Whom It May Concern:

I am in the process of preparing my PhD dissertation, and I would greatly appreciate permission to reuse the material from my recent first author publication in the MDPI journal Cancers. The information regarding the article that I am requesting permission to reuse is as follows:

Journal: Cancers
Article Title: "An Analytical Model of Leakage Neutron Equivalent Dose for Passively-Scattered Proton Radiotherapy and Validation with Measurements"
Authors: Christopher Schneider, Wayne Newhauser, and Jad Farah
Volume Number: 7
Page Numbers: 795–810
doi:10.3390/cancers7020795

Information regarding the new document I am preparing is as follows:

Article/Chapter Title: Dissertation Chapter
Author: Christopher William Schneider
Publisher: Louisiana State University and Agricultural and Mechanical College

I will include a citation to the original article on the first page of the chapter. Would it be possible for me to receive a letter or email stating that MDPI grants permission for the use of this material in my dissertation? Thank you, and please let me know if there is anything I can do.

Sincerely

Christopher W Schneider
Ph.D. Candidate, Medical Physics
Newhauser Research Group
Louisiana State University

**JOHN WILEY AND SONS LICENSE
TERMS AND CONDITIONS**

Jan 04, 2019

This Agreement between Mr. Christopher Schneider ("You") and John Wiley and Sons ("John Wiley and Sons") consists of your license details and the terms and conditions provided by John Wiley and Sons and Copyright Clearance Center.

License Number	4501710737502
License date	Jan 04, 2019
Licensed Content Publisher	John Wiley and Sons
Licensed Content Publication	Medical Physics
Licensed Content Title	A descriptive and broadly applicable model of therapeutic and stray absorbed dose from 6 to 25 MV photon beams
Licensed Content Author	Christopher W. Schneider, Wayne D. Newhauser, Lydia J. Wilson, Uwe Schneider, Robert Kaderka, Saveta Miljanić, Željka Knežević, Liliana Stolarczyk, Marco Durante, Roger M. Harrison
Licensed Content Date	Jun 1, 2017
Licensed Content Pages	10
Type of use	Dissertation/Thesis
Requestor type	Author of this Wiley article
Format	Print and electronic
Portion	Full article
Will you be translating?	No
Title of your thesis / dissertation	ANALYTICAL MODELS OF STRAY RADIATION ABSORBED DOSE FROM X-RAY AND PROTON EXTERNAL BEAM RADIATION THERAPIES
Expected completion date	Mar 2019
Expected size (number of pages)	220
Requestor Location	Mr. Christopher Schneider 706 Northbrook Dr BATON ROUGE, LA 70820 United States Attn: Mr. Christopher Schneider

Vita

Christopher William Schneider was born at Lakeside Hospital in Metairie, Louisiana to his loving parents: Michael and Carol Schneider. He met his wife, Caroline Lillian Schneider (*née* Poché), while both were attending Southeastern Louisiana University in Hammond, Louisiana. He majored in physics and she in chemistry. A match made in heaven, they spent their first date watching the transit of Mercury across the Sun through a telescope on the lawn of Pursley Hall, and they married the summer after Christopher's graduation.

Through Christopher's undergraduate research on gravitational waves, he was able to spend a summer working at the National Astronomical Observatory of Japan in Mitaka, Tokyo. This experience convinced him that he wanted to be part of the global community of scientists. As a PhD student at Louisiana State University and Agricultural and Mechanical College, he decided to pursue medical physics, a field that would allow him to be part of an international coalition of scientists while also working directly to help those in the community he calls home. As a Chateaubriand Fellow, he was able to perform a portion of his dissertation research at the *Centre de protonthérapie de l'institut Curie* in Paris and as a visiting scientist at the *Physikalisch-Technische Bundesanstalt* in Braunschweig, Germany. In those moments not spent on research, Christopher enjoyed playing fingerstyle guitar and brewing beer with Caroline in their garage.

After graduate school, Christopher plans to remain in the state and community that have given him so much by accepting a residency position at Mary Bird Perkins Cancer Center in Baton Rouge, Louisiana.